

**Design & Development of Laser Decal Transfer Based μ -
3D Printer for Printing Micro Scale Structures for MEMS
Applications**

Ph.D. THESIS

By

Anshu Sahu



Department of Mechanical Engineering

Indian Institute of Technology Indore

OCTOBER 2023

**Design & Development of Laser Decal
Transfer Based μ -3D Printer for Printing
Micro Scale Structures for MEMS
Applications**

A THESIS

*Submitted in partial fulfilment of the
requirements for the award of the degree
of*

DOCTOR OF PHILOSOPHY

By

Anshu Sahu



**Discipline of Mechanical Engineering
Indian Institute of Technology Indore**

OCTOBER 2023



CANDIDATE'S DECLARATION

I hereby certify that the work being presented in the thesis titled **Design & Development of Laser Decal Transfer Based μ -3D Printer for Printing Micro Scale Structures for MEMS Applications** in the partial fulfilments of the requirements for the award of the degree of **DOCTOR OF PHILOSOPHY** and submitted in the **Department of Mechanical Engineering, Indian Institute of Technology, Indore** is an authentic record of my work performed during the time period of Jan, 2020 to May, 2023 under the supervision of Prof. I. A Palani, Department of Mechanical Engineering, and Prof. Vipul Singh, Department of Electrical engineering, Indian Institute of Technology, Indore.

The matter presented in the thesis has not been submitted by me for the award of any other degree of this or any other institute.

Anshu
09/10/2023
Signature of the student with date
(Anshu Sahu)

This is to certify that the above statement made by the candidate is correct to the best of my/our knowledge.

Signature of Thesis Supervisor #1 with date *[Signature]*
(Prof. I. A. Palani) *09/10/2023*

Signature of Thesis Supervisor #2 with date *[Signature]*
(Prof. Vipul Singh) *09/10/2023*

Anshu Sahu has successfully given his Ph.D. Oral Examination held on **09/10/2023**.

Signature of Thesis Supervisor #1 with date *[Signature]*
Prof. I. A. Palani *09/10/2023*

Signature of Thesis Supervisor #2 with date *[Signature]*
Prof. Vipul Singh *09/10/2023*

*Dedicated to my
Maa
&
Papa*

ABSTRACT

The majority of the microelectromechanical (MEMS) devices are fabricated using either a lithography process or some microfabrication system which goes through the phase change process during the fabrication process. The phase change during processing leads to the change in the chemical as well as the functionality of the fabricated devices hence it is essential to develop a process which retains the chemical and functionality of the structure before and after the fabrication process. The research work focuses on the development of a laser decal transfer-based micro 3D printing process by using a thin film as feed material for the printing of MEMS devices.

In laser decal transfer, the thin film material is deposited on the sacrificial layer coated transparent substrate and the laser beam irradiates from the top of the transparent donor substrate. The laser energy gets absorbed in the sacrificial layer and vaporizes to form high-pressure gas. The high pressure tries to expand and apply a pressure force on the donor thin film that leads to the ejection of the thin film from the donor substrate and collected on another substrate. Since the laser spot size and the donor thin film are in the order of a few microns, the feature size will be the same. To fabricate micro-scale three-dimensional structures, the laser decal transfer process will be continuing to build pixel-by-pixel and layer-by-layer fashion for the fabrication of the microscale MEMS devices.

The process involved a high energy density laser heat source as the driving force for the printing process hence a numerical simulation is performed to investigate the effect of laser interaction with material and estimate the temperature rise during the fabrication process. Moreover, the process involved the absorption of laser energy and leads to the formation of a plume beneath of thin film. The numerical simulation predicts the shape and size of the plume before the material ejection from the donor substrate and the same is monitored using a high-speed camera using time resolve imaging `technique.

At last, Laser micro3D printing is deployed for the fabrication of the different microelectronics devices which can be used for different electronics circuits such as a microheater, antenna, etc. To show the capabilities of micro 3D printing, multiple-layer NiTi-based strain gauges are printed on flexible PET sheets and their performance was investigated at different loading conditions. For three-dimensional strain measurement, a rosette strain gauge is also printed, and its performance is measured at different strain conditions using the universal testing machine.

To check the feasibility of the process towards device fabrication, the ZnO nanostructure was transferred on the PET sheet and its performance was investigated before and after the printing process for optomechanics applications. The process involved micro features printing on a substrate which can induce the roughness of the substrate, hence the micro 3D printing is performed to print the ZnO seed layer in a line pattern followed by the hydrothermal growth for the triboelectric nanogenerator for energy harvesting applications.

ACKNOWLEDGEMENTS

First of all, I would like to express my deepest gratitude and acknowledge to my research guides **Prof. I. A. Palani**, Mechatronics and Instrumentation Lab, & **Prof. Vipul Singh** Molecular and Nano Research Lab, for his continuous guidance, patience, motivation, and enthusiasm. His valuable advice, constructive criticism, extensive discussions, and immense knowledge helped me to build a basic understanding of the subject and accomplish my thesis..

I would like to thank **Prof. Suhas Joshi**, Director, IIT Indore, **Dr. S. Dinakaran**, Head of Department, Mechanical Engineering, for supporting me with the sophisticated facilities to conduct my research. I would also like to thank PSPC members **Dr. Eswara Korimilli** and **Dr. Indrasen Singh** for giving their precious time for my assessment and for their valuable comments and suggestions towards enhancing my research work. My sincere thanks **Dr. Satyanarayana Patel**, DPGC convener for his sincere support.

Also, I want to especially thank, **Dr. Ashish Shukla**, **Dr Nandhini Patra**, **Dr. Jayachandran S**, **Dr. Mani Prabhu**, **Dr. Muralidharan M**, **Dr. Manikandam M**, **Dr. Achyuth Kulkarni**,. and **Dr. T. Geetapriyan** for their moral support, mentorship, constant motivation and assistance during the entire duration of Ph.D.

I would like to thank the **Department of Mechanical Engineering, IIT Indore** as well as **the Department of MEMS, IIT Indore** for allowing access to the facility of various characterization techniques and providing a pleasant atmosphere for research. I would also like to acknowledge **HoD, Department of Mechanical Engineering, IIT Indore** for his constant support throughout the journey. I am deeply indebted to **Department of Science & Technology** and **IIT Indore** for their financial assistance to the research work carried out.

I would also acknowledge my appreciation also extends to **Opto-Mechatronics Group members: Mr. Ashwin Wagh, Mr. Krishnapal Singh Tomar, Mr. Pravin Karna, Mr. Kaushal Gangwar, Mr. Arpit Kumar Singh, Mr. Kaushik Savaniya, Ms. Diksha Jaukar** for their strong support and stimulating discussions. Special thanks to **Mr. Sarathkumar, Dr. S. Jayachandran & Mr. Mayank** for continuous support and endless talk during COVID phases. Also, I would like to admire my colleagues **Mr. Abhishek Ojha, Mr. Dilip Pandey, Mr. Rahul Yadav** for their constant care and endorsement throughout this period. My sincere appreciation extends to my B.Tech inmates Piyush, Vijay, Kailash, and Shibani, Puneet and Srijan for their help and support during my work.

Finally, I would like to express my deepest gratitude and respect to my parents (**Smt. Ramsakhi Devi & Shri. Panna lal Sahu**) and my **entire family** for an ever-supportive rock in my life with their unflinching support.

Completing my thesis would not have been feasible without the collaborative encouragement and assistance of all of the persons named above. Despite the fact that their names are given here, their contribution to this effort extends well beyond words.

Thank you so much for your significant input.

Anshu Sahu

LIST OF PUBLICATION

S.No.	Journal Publication	Status
1.	Anshu Sahu, Ashish Shukla, Daisuke Nakamura, Vipul Singh, I.A. Palani, “Parametric investigation on Laser-Induced Forward Transfer of ZnO nanostructure on flexible PET sheet for optoelectronic application”, <i>Microelectronic Engineering</i> , 244–246, 2021, https://doi.org/10.1016/j.mee.2021.111569 (Impact factor: 2.62)	Published
2.	Anshu Sahu, I.A. Palani, Vipul Singh, “Investigation on Fabrication of Niti based Strain Gauge using Laser Decal Transfer based μ -3D Printing”, <i>Manufacturing Letters</i> , 32, 49-53, 2022, https://doi.org/10.1016/j.mfglet.2022.03.001 (Impact factor: 4.99)	Published
3.	Anshu Sahu, Vipul Singh, I.A. Palani, “Parametric Investigations on Laser-Induced Forward Transfer Based Micro-3D Printing of NiTi Alloy” <i>Materials and Manufacturing Processes</i> , 1-10, 2022, https://doi.org/10.1080/10426914.2022.2072877 (Impact factor: 4.78)	Published
4.	Anshu Sahu, Arpit Singh, Ayush Singh, Vipul Singh, I. A. Palani, “Investigation of Material Ejection in Laser Decal Transfer Based μ -3D Printing of ZnO ceramics with long Pulsed CO ₂ Laser” <i>IJAMT</i> (Impact factor: 3.563)	Under Review

Book Chapter and Conference Proceeding:

1. Sahu, A., Singh, V., Palani, I.A. (2022). Laser-Induced Forward Transfer of NiTi for Functional Application. In: Krishnapillai, S., R., V., Ha, S.K. (eds) *Composite Materials for Extreme Loading . Lecture Notes in Mechanical Engineering*. Springer, Singapore. https://doi.org/10.1007/978-981-16-4138-1_12

2. Sahu, A., Karna, P., Singh, V., Palani, I.A. (2023). Laser Induced Forward Transfer-Based Micro-3D Printing of NiTi Alloy. In: Ramesh Babu, N., Kumar, S., Thyla, P.R., Sripriyan, K. (eds) Advances in Additive Manufacturing and Metal Joining. Lecture Notes in Mechanical Engineering. Springer, Singapore. https://doi.org/10.1007/978-981-19-7612-4_17
3. Anshu Sahu, Ashwin Wagh, Vipul Singh, I A Palani, Suhas S. Joshi, “Laser Induced Forward Transfer Based Micro-3D Printing for Multi-layer Three-Dimensional Structure” in 12 COPEN conference, Dec 2022
4. Anshu Sahu, Vipul Singh, I A Palani, “Micro-3D Printing of NiTi Shape Memory Alloy for Sensor Fabrication” Material Research society of Japan, Dec 2020
5. Anshu Sahu, I. A. Palani, Vipul Singh, “Fabrication of NiTi Rosette Strain Gauge by Laser Decal Transfer based μ -3D Printing for Three-Dimensional Strain Measurement” SMS Conference, Oct 2023 (Accepted for oral Presentation)
6. Anshu Sahu, I. A. Palani, Vipul Singh “Laser Decal Transfer Based Laser μ -3D Printing for Multi-layer Structure” PFAM conference, Sep 2023 (Accepted for oral presentation)

Patent Details:

I. A. Palani, Anshu Sahu, Krishna Pal Singh Tomar, , Vipul Singh, 2022 “Implementation of Laser Decal Transfer Towards μ -3D Printing”, 202221022267 (**filed**)

TABLE OF CONTENTS

List of Figure

List of Table

ABBREVIATIONS

Chapter 1 Introduction	1
<i>1.1 Micro Fabrication-Overview</i>	<i>1</i>
<i>1.2 3D printing/ Additive manufacturing -Overview</i>	<i>4</i>
<i>1.3 Laser-Induced Forward Transfer</i>	<i>9</i>
<i>1.4 Motivation for the thesis:</i>	<i>12</i>
<i>1.5 Objectives of thesis</i>	<i>12</i>
<i>1.6 Significant contribution</i>	<i>13</i>
<i>1.7 Organisation of thesis</i>	<i>13</i>
<i>1.8 Flowchart of Thesis</i>	<i>14</i>
Chapter 2 Literature Survey	15
<i>2.1 Overview of laser Induced Forward Transfer</i>	<i>15</i>
2.1.1 Solid Donor	16
2.1.2 Liquid Donor	19
2.1.3 Dynamic Release Layer (DRL-LIFT)	21
<i>2.2 Time-resolved Shadowgraphy</i>	<i>24</i>
2.2.1 Solid-phase transfer	24
2.2.2 Liquid phase transfer	26
<i>2.3 Applications of Laser-Induced Forward Transfer:</i>	<i>29</i>
<i>2.4 Research Gap</i>	<i>33</i>
<i>2.5 Summary</i>	<i>33</i>
Chapter 3 Theoretical Simulation of laser decal transfer	35
<i>3.1 Temperature estimation through numerical simulation</i>	<i>35</i>

3.1.1	Thermal equation of laser material interaction	35
	Material Properties	37
	Assumptions and Boundary Conditions	38
3.1.2	Influence of laser fluence and PDMS thickness	39
3.2	<i>Summary</i>	43
Chapter 4	Experimental Setup	45
	<i>Experimental Setup Specifications</i>	45
4.1	<i>Donor Preparation</i>	47
4.1.1	Sacrificial Layer coating.....	48
4.1.2	Donor thin film deposition	48
4.2	<i>Imaging Setup</i>	50
4.3	<i>Characterization</i>	50
4.3.1	Printed Morphology and Structure.....	50
4.3.2	The functionality of printed structures.....	51
4.4	<i>Methodology</i>	52
Chapter 5	Parametric investigation of NiTi shape memory alloy through μ-3D printing	53
5.1	<i>Influence of laser fluence and PDMS thickness</i>	53
5.2	<i>Effect of substrate heating</i>	57
5.3	<i>Effect of spot overlap</i>	59
5.4	<i>Effect of focused and defocused condition</i>	60
5.5	<i>Morphology and structural characteristics</i>	61
5.6	<i>Multilayer structure</i>	63
5.7	<i>Metal printed for electronics applications</i>	63
5.8	<i>Summary</i>	65
Chapter 6	Particle dynamics Study using long Pulse in Laser μ-3D printing	69

6.1	<i>Micro 3D printing</i>	71
6.2	<i>Plume formation</i>	73
6.3	<i>Influence of laser fluence on plume</i>	74
6.4	<i>Mode of transfer</i>	76
6.5	<i>Summary</i>	78
Chapter 7 Competences of μ-3D printing μ-scale structures for MEMS		
Applications		
.....		81
7.1	<i>NiTi-based Strain Gauge</i>	81
7.1.1	<i>Morphology</i>	82
7.1.2	<i>Performance analysis</i>	83
7.2	<i>ZnO-based UV-LED for opt mechatronics application</i>	88
7.2.1	<i>Numerical modelling of ITO sacrificial Layer and ZnO donor film</i>	89
	□ <i>Influence of laser wavelength and laser fluence</i>	90
	□ <i>Influence of sacrificial layer thickness</i>	92
7.2.2	<i>ZnO nanostructure printing</i>	93
7.3	<i>Micro-3D printed ZnO based Triboelectric nanogenerator</i> ..	98
7.4	<i>Summary</i>	106
Chapter 8 Conclusion and Scope for Future Work		
.....		109
8.1	<i>Conclusion</i>	109
<i>To retain the functionality and chemical composition, the PDMS sacrificial layer was used to absorb the laser energy and prints the material without phase change. The following conclusions are drawn from the mentioned objectives in chapter 1:</i>		
.....		109
Objective 2: Various prospects towards printed feature size		
.....		110

Objective 3: Process dynamics and mode of particle ejection during printing process	111
Objective 4: Laser μ-3D printing capability towards functionalities and its behaviour.....	112
8.2 <i>Future Scope</i>	115

LIST OF FIGURES

Fig. 1.1 Top-down and Bottom-Up approach in manufacturing	2
Fig. 1.2 Classification of Microfabrication Techniques	3
Fig. 1.3 Number of papers found in the Web of Science till 31/03/2020 (a) MEMS) and 3D printing or additive manufacturing, respectively; (b) the combination of MEMS. [4].....	5
Figure 1.4 Micro-Additive manufacturing Techniques. [4].....	6
Fig. 1.5 (a) Micro-transfer printing mechanism for metal printing and (b) silicon thin film stacked on silicon substrate. [8].....	7
Fig. 1.6 Schematic of micro metal droplet based 3D printing with (a) continuous jet ejection mode and (b) drop on demand mode. [9]	8
Fig. 1.7 Laser Induced Forward transfer mechanism.	10
Fig. 1.8 Laser decal transfer based μ - 3D printing mechanism.	11
Fig. 2.1 Flow chart of literature survey.....	16
Fig. 2.2 Transfer mechanisms of LIFT at different laser fluences. (a) partial vaporization and film fracture at low fluence; (b) thermal radial expansion and film exfoliation at low fluence; (c) melting of donor film and at threshold fluence; (d) partial vapour formation and propelling melted material at high fluence, and (e) complete vaporization at very high fluence	17
Fig. 2.3.Laser Energy profiles of different shaped beams: (a) edges- beam 1, (b) centre-beam 2, and (c) beam 1+beam 2.	19
Fig. 2.4 Principle of operation of liquid transfer a) vapour bubble formation due to laser absorption (b) initial expansion of the vapour bubble (c) jet formation.	20
Fig. 2.5 Schematic of Dynamic Release Layer-LIFT (DRL-LIFT).....	22
Fig. 2.6. Shadography images at different time frames after laser irradiation in the LIFT process at laser fluences: (a) 1.2, (b) 2.4, (c) 5.6, and (d) 10 J /cm ²	28
Fig. 2.7 (a) L μ -3D printed gold track printed on top of a copper support structure, (b) SEM image of the printed gold bar after etching of support, (c) SEM image of printed actuator, and (d) high-aspect-ratio	

multimaterial of gold and platinum structures fabricated by using ns-LIFT.	30
Fig. 2.8 LIFT deposited an Au helix structure (rotating out-of-plane in a clockwise direction) viewed at an angle of 60° (a) after, (b) before etching, (c) shows the helix after etching seen from the top (0°).	31
Fig. 2.9 Seven layered printed grid structure (top view) of fibroblasts (green) and keratinocytes (red) demonstrates micropatterning capabilities of LIFT. Scale bars are 500 μm.	32
Fig. 3.1 (a) Visualization of (a) Geometrical model and (b) Meshing used in the simulation	37
Fig. 3.2 Boundary condition and incident laser energy on modelled geometry	38
Fig. 3.3 Temperature generated with 10 μs pulse width. (a) Gaussian temperature contour at a laser fluence of 1000 mJ/cm ² , (b) temperature at the top surface with 1.5 μm sacrificial layer.....	40
Fig. 3.4 Interface temperature at different laser fluence with a sacrificial layer thickness (a) 1.5 μm sacrificial layer, and (b) 3 μm sacrificial layer.....	41
Fig. 3.5 The velocity of the pixels estimated by numerical simulation.	43
Fig. 4.1 Illustrate the system design component for Laser μ-3D printing.	45
Fig. 4.2 (a) The experimental setup with degree of freedom of donor and acceptor stages and (b) Experimental setup of Laser μ-3D printing and strategy for line printing with pulse overlap.	47
Fig. 4.3 Preparation of donor with sacrificial layer coating and thin film deposition.....	47
Fig. 4.4 (a) Transparent Silicon substrate at laser wavelength 10.6 μm Sacrificial layer coating on a silicon wafer.....	48
Fig. 4.5 Schematic diagram of sputtering and experimental setup with three deposition guns.	49
Fig. 4.6 Schematic diagram of particle dynamics experimental setup	50
Fig. 5.1 Transferred pixel on the receiver substrate at laser fluences (a) 600 mJ/cm ² , (b) 770 mJ/cm ² , (c) 900 mJ/cm ² , and (d) 1030 mJ/cm ² ..	54

Fig. 5.2 Transferred pixel on the receiver substrate at laser fluences (a) 1800 mJ/cm ² , (b) 2300 mJ/cm ² , (c) 2900 mJ/cm ² , and (d) 3600 mJ/cm ²	55
Fig. 5.3. Width of line pattern with laser fluences at sacrificial Layer thickness (a) 1.5 μm and (b) 3 μm.	56
Fig. 5.4. (a) Scotch tape test on the universal testing machine and (b) NiTi deposition at a laser fluence of 2300 mJ/cm ² with 3 μm PDMS at substrate temperature at 25°C, 100 °C, and 200 °C.....	58
Fig. 5.5 Weight of Scotch tape before and after the test.....	58
Fig. 5.6 Transferred pixel with respect to beam overlap at laser fluence 900 mJ/cm ² with 1.5 μm PDMS thickness (a) 30, (b) 60, and (c) 90 %	60
Fig. 5.7 Effect of beam condition on the printed line track at laser fluence 1.03 J/cm ²	61
Fig. 5.8 (a) X-ray diffraction of the deposited pixel, (b) EDS elemental analysis of the deposited pixels, and (c) hexagonal pattern at laser fluence 1000 J/cm ² with 1.5 μm PDMS thickness.....	62
Fig. 5.9 Multilayer three-dimensional structure with top view and cross-sectional view substrate at laser fluence 1030 mJ/cm ²	63
Fig. 5.10 Laser μ-3D metal printed structure for electronics applications.	64
Fig. 6.1 The ablation of a sacrificial layer at laser fluence 1530 mJ/cm ² with time frame after laser irradiation	70
Fig. 6.2 (a) The PDMS sacrificial layer surface temperature at different laser fluences at a pulse duration of 10 μs, and (b) the temperature at the interface of a sacrificial layer at ZnO donor film.	71
Fig. 6.3 (a) RF sputtered ZnO on the donor substrate. Micro 3D printed ZnO line track with 90% pulse overlaps at laser fluence (b) 530 mJ/cm ² , (c) 1030 mJ/cm ² , and (d) 1530 mJ/cm ²	72
Fig. 6.4 The ZnO track printed on a silicon wafer at laser fluences (a) 530 mJ/cm ² , (b) 1030 mJ/cm ² , and (c) 1530 mJ/cm ²	73
Fig. 6.5 The plume formation and expansion in laser decal transfer with time at laser fluence 530 mJ/cm ²	74

Fig. 6.6. The Plume length and width with a different time frame at laser fluence 530 mJ/cm ²	74
Fig. 6.7 The time-resolved image at different laser fluences 530 mJ/cm ² , 1030 mJ/cm ² , and 1530 mJ/cm ² and printed line track on acceptor substrate at respective laser fluences.	75
Fig. 6.8 Maximum plume size before material ejection at different laser	76
Fig. 6.9 Schematic of particle ejection mode in laser decal transfer process with angular deviation (a) cap regime with $\theta < 5^\circ$, (b) debris regime with $5 > \theta > 30^\circ$, (c) Bursting mode with $\theta > 30^\circ$, (d)-(f) shows the three modes of ejection at a laser fluence of 530 mJ/cm ² , 1030 mJ/cm ² , and 1530 mJ/cm ² respectively in time-resolved image just after the material ejection	77
Fig. 7.1 (a) The NiTi printed strain gauge on the flexible PET sheet, (b) The NiTi pixel deposited on the PET substrate, (c) high magnification surface morphology of three-layer NiTi at laser fluence 1.03 J/ cm ² , (d) and (e) thickness of three-layer and five-layer strain gauges respectively.	82
Fig. 7.2 shows (a) The principle of the strain gauge, (b) strain gauge loading condition on the universal testing machine and (c) stress induced on the PET sheet and the performance of strain gauge in terms of resistance.....	83
Fig. 7.3 (a) Resistance and $\Delta R/R$ with different stain % of 5 layered strain gauge	85
Fig. 7.4 (a) CAD model of 7-layer rosette strain gauge, (b) printed Strain gauge, (c) optical image of gauge at higher magnification, (d) EDX analysis, and (e) Loading condition	86
Fig. 7.5 Electromechanical response of the strain gauge at strain speed 1 mm/min.	87
Fig. 7.6 Electromechanical response of the strain gauge at strain speed 0.1 mm/min.	88
Fig. 7.7 The temperature plot with 9 ns pulse duration at the interface of the sacrificial layer and donor materials at different laser fluence and laser wavelength.....	91

Fig. 7.8 The temperature plot with 9 ns pulse duration at the interface of the sacrificial layer and donor materials (a) different wavelength with laser fluence at 550 mJ/cm ²	92
Fig. 7.9 The temperature plot at the interface of the sacrificial layer and donor materials at different sacrificial layer thickness with laser fluence at 550 mJ/cm ²	93
Fig. 7.10 The acceptor substrate and donor substrate before the transfer of ZnO nanostructure	94
Fig. 7.11 (a) and (b) illustrates the FESEM image of acceptor and donor (ZnO Nanostructure) (c) ICCD captured image during the LIFT process of at 550 mJ/cm ² laser fluence (d) donor film after transfer (e) acceptor film after transfer	94
Fig. 7.12 (a) Acceptor substrate after transfer at laser fluence 250 mJ/cm ² and (b) shows the transfer ZnO nanostructure at high magnification.	95
Fig.7.13 (a) Acceptor film after LIFT transfer at 100 mJ/cm ² and (b) High magnification of cluster of nanostructures on acceptor substrate.	96
Fig. 7.14 (a) XRD spectra of ZnO Donor substrate before transfer (b) XRD spectra of ZnO acceptor substrate after transfer at laser fluence 100 mJ/cm ²	97
Fig. 7.15 (a) PL spectra of donor film before LIFT transfer, and (b) PL spectra of acceptor film after LIFT transfer at laser fluence 100 mJ/cm ²	98
Fig. 7.16 The operating principle of the contact mode.	99
Fig. 7.17 (a) Schematic of ZnO base triboelectric nanogenerator and (b) L-μ 3D printed ZnO seed layer printed on ITO coated glass.	101
Fig. 7.18 ZnO nanostructures grown on the Laser μ-3D printed ZnO seed layer, (b) composition of nanostructure by EDS analysis, (c) X-ray diffraction of ZnO shows different phases of ZnO and ITO substrate, (d) final triboelectric nanogenerator.	102
Fig. 7.19 Open circuit voltage and short circuit current at different tapping rate (a &b) 200 rpm, and (c & d) 350 rpm respectively.	104
Fig. 7.20 Total peak Power developed at various tapping rate.	105

Fig. 8.1 Laser μ -3D printed metal microdevices for MEMS application	111
Fig. 8.2 Different mode of ejection with long pulsed laser system ...	112
Fig. 8.3 laser μ -3D printed strain gauge and its performance.....	113
Fig. 8.4 Selective deposition of ZnO nanostructure for UV-LED application.....	114
Fig. 8.5 Laser μ -3D printed ZnO based triboelectric nanogenerator.	115
Fig. 8.6 Multi-material Printing using Laser μ -3D printing, and (b) Overhand curved structure.....	116

LIST OF TABLES

Table 3.1 Material properties used in the simulation.....	36
Table 7.1 Optical properties of ITO sacrificial layer.....	88
Table 7.2 Input Parameter and material properties.....	88

ABBREVIATIONS

Abbreviations	Expansion
L- μ 3D Printing	Laser Micro 3D Printing
LIFT	Laser Induced Forward Transfer
LDT	Laser Decal Transfer
DRL	Dynamic Release Layer
PDMS	Polydimethylsiloxane
ITO	Indium dioxide
MEMS	Microelectromechanical Systems
EDS	Energy Dispersive Spectroscopy
SEM	Scanning Electron Microscope
TENG	Triboelectric nanogenerator
XRD	X-Ray Diffraction
FEM	Finite Element Method
PL	Photoluminescence

Chapter 1

Introduction

1.1 Micro Fabrication-Overview

With advances in the field of the Internet of Things (IoT), today different sensors and actuators are available in most mechanical or electrical systems. These sensors are mostly employed in micro-electro-mechanical systems (MEMS). Hence the MEMS emerges as a vital technology that accelerates the fabrication of micro-scale sensors and actuators for functional devices. Generally, the MEMS structures are in the order of 0.01-500 microns which are fabricated by different conventional microfabrication techniques. In most cases, these structures are thin film multi-material-based structures that show interdisciplinary functionality.

Microfabrication techniques are a group of technologies that are used to create structures and devices on a microscopic scale, often in the micrometre (μm) or sub-micrometre range. These approaches have transformed several industries, including microelectronics, optics, biomedical engineering, and microfluidics, allowing the creation of sophisticated and functioning microscale devices.[1]

The area of microfabrication evolved with the introduction of photolithography in the 1950s, which enabled the patterning of materials at the microscale. Several new approaches have been developed and enhanced, each with its distinct capabilities and uses. For the manufacturing of MEMS devices, bottom-up and Top-down are the two distinct techniques used for the fabrication of micro-scale structures.[2] Both methods have different procedures and modes of operation. Top-down technique: In the top-down approach, a larger-scale material is used as feed material, and the structures are fabricated by smaller systematic removing of material from the initial piece. It is comparable to shaping a massive block of material by cutting out or sculpting it. Lithography and etching are generally deployed for a top-down

approach in the microfabrication process.[3] In contrast, the bottom-up technique involves the addition of individual atoms, molecules, and powders and gradually putting them together to form three-dimensional structures. It is comparable to constructing a structure out of separate construction components. Self-assembly, deposition processes, and 3D printing are common techniques which fall under this approach. Fig. 1.1 shows the Top-down and bottom-Up approach.

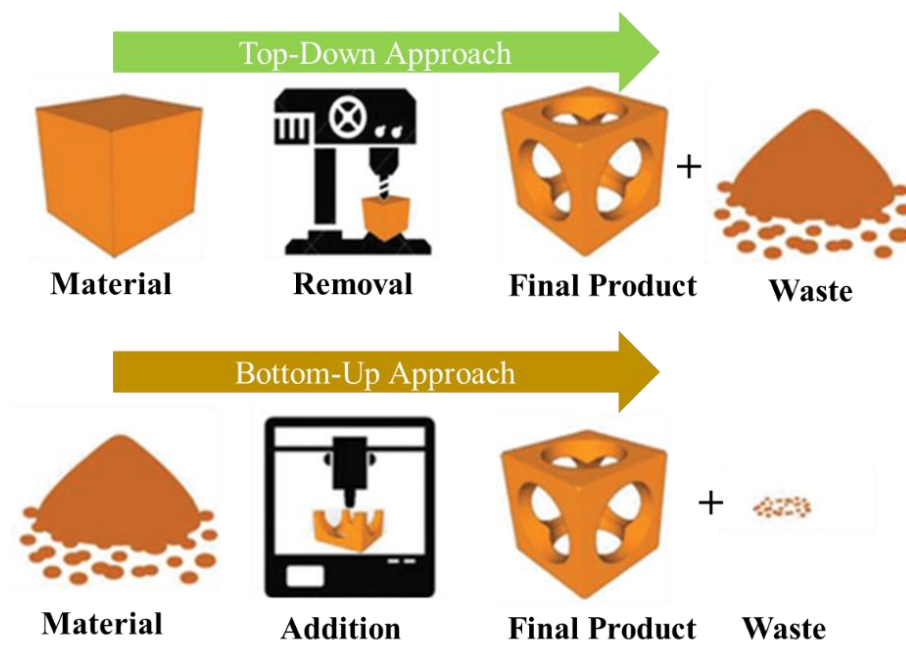


Fig. 1.1 Top-down and Bottom-Up approach in manufacturing

Fig. 1.2 shows the classification of the microfabrication process currently used for MEMS structures and sensors fabrication. To produce the necessary microscale characteristics and capabilities, different methods are often used together or as part of a wider manufacturing process.

Material removal is one of the important aspects of microfabrication for the removal of selective materials from a substrate to generate desired structures and micro features. Various techniques are used depending on material and its application such as Etching, Milling, Laser ablation, electrochemical machining, ion beam machining etc.

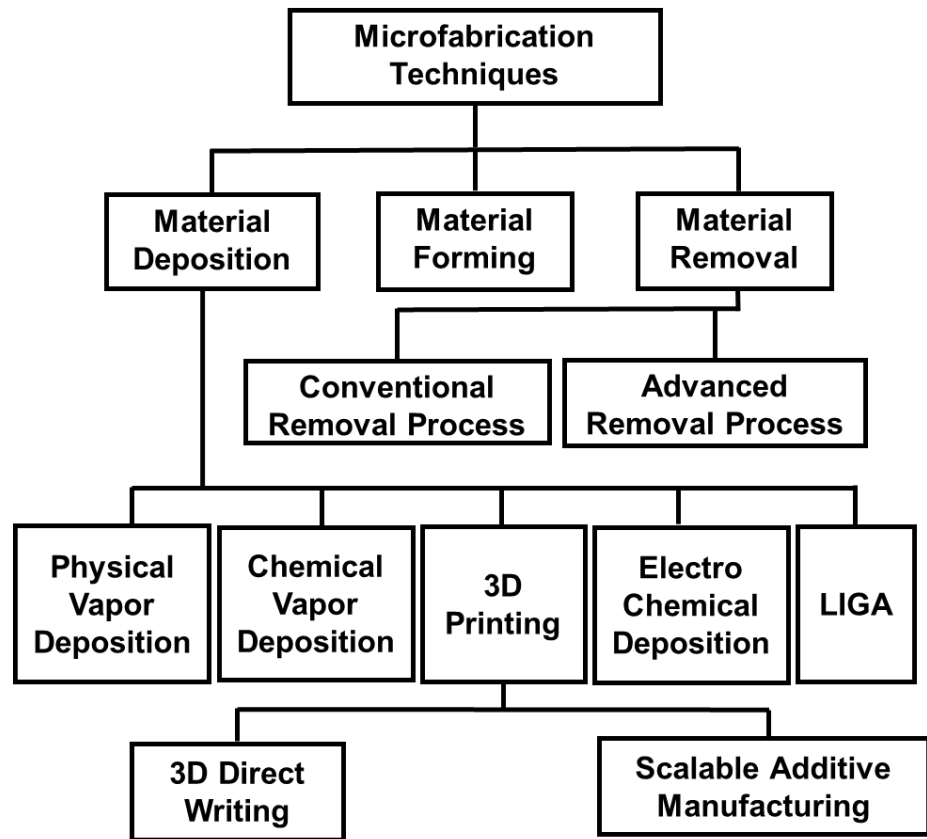


Fig. 1.2 Classification of Microfabrication Techniques

The process of adding or depositing thin layers of materials onto a substrate to build functional structures and components on a microscale is referred to as material deposition in microfabrication. It is the widely used microfabrication technique for device fabrication in electronics for MEMS applications. Lithographic methods are particularly well adapted to minute structures. A mould insert is built up by patterning a resist with an electroplated microstructure. It is distinguished by exceptionally high structural tolerances, tiny lateral dimensions, and sidewall roughness of less than 50 nm. It also provides the multi-material deposition with high resolution for three-dimensional structural micro devices. Photolithography can be employed by making a photomask, a glass plate, or a plastic sheet covered with a non-UV-transparent film. The mask is put on a photoresist on a silicon wafer, and this photoresist is not exposed to UV light via the open sections of the mask. Depending on the photoresist, either the exposed or non-exposed portions create the

pattern, while the remaining photoresist is washed off the wafer, forming a master mould.[4]

3D Direct-write (DW) methods have gained a lot of attention for microfabrication because of pattern design freedom and material patterning simultaneously. Even though the best attainable resolution with DW methods is (100 nm [Haight et al., 2003]) is lower than the lithography process. But the advantages of a wide range of materials, pattern freedom, inherent straightforwardness, and less production time, give more attention towards microfabrication.

1.2 3D printing/ Additive manufacturing -Overview

3D printing/additive manufacturing has shown its potential for fabrication of macro-scale structures for printing engineering components with high degree of complexity, design freedom, material freedom with less material waste and reduces the production time to great extent. Due to its high diversity in material and design, various structures have been demonstrated for MEMS application. Fig. 1.3 shows the trend of research articles related to MEMS application and 3D printing individually till 31 March -2020 in the scientific community.

MEMS have been established in the scientific literature since 1980, but it took another ten years to start 3D printing in scientific research. With the advancement of multiple 3D printing technologies, researchers took another decade for deploying microfabrication for MEMS applications. Despite the increased degrees of freedom provided by 3D printing, less than 1% of 3D printing research focuses on MEMS. This is in contradiction to the potential benefits of 3D printing in MEMS manufacturing, particularly in avoiding challenges of inappropriate under-etching of 3D devices caused by anisotropic.

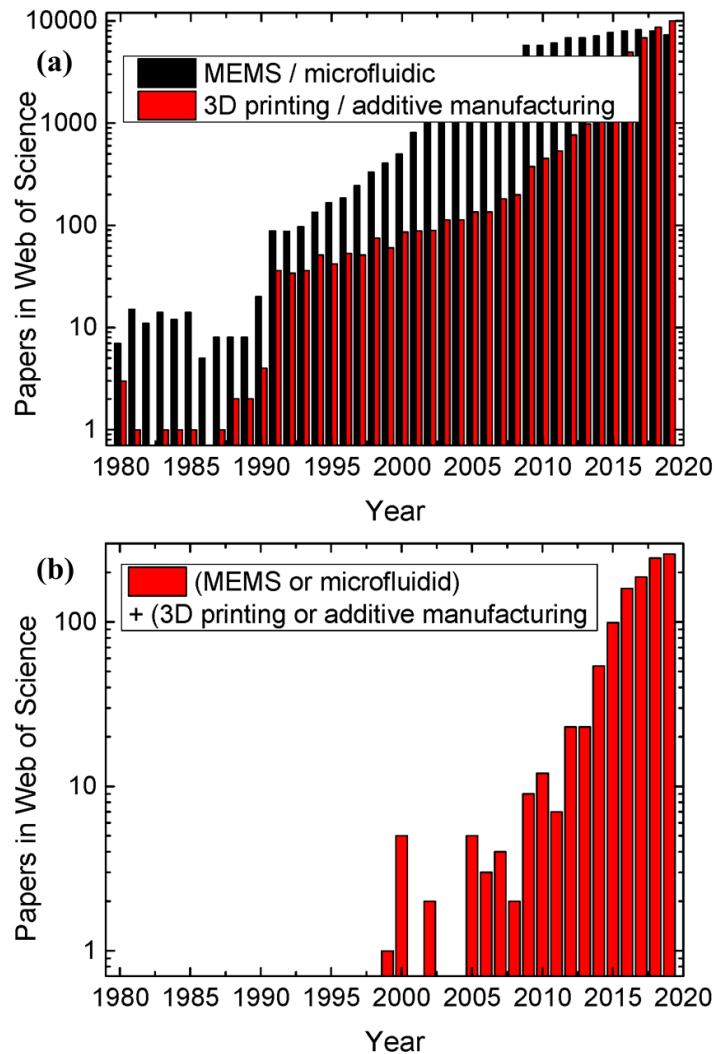


Fig. 1.3 Number of papers found in the Web of Science till 31/03/2020 (a) MEMS) and 3D printing or additive manufacturing, respectively; (b) the combination of MEMS. [4]

The term "3D printing" is most frequently associated with stereolithography to print light-sensitive objects from a polymer solution by utilising a laser for cross-linking the polymer at specified places.[5] Direct laser writing technologies based on two-photon polymerization (2PP) are effective tools for on-demand printing of accurate and sophisticated 3D structures at the micro and nanoscale scale.[6] Despite of significant development, the different strategies and effort has been applied to enhance the resolution and feature size for printing functional features for MEMS applications. The second most widely used technique for microfabrication is inkjet printing due to its wide range of

functional material processing for sensors fabrication. However, there are some challenges which limit its industrial applications such as low viscosity fluid, nanoparticle suspension and nozzle clogging.[7]

With the further invention of new 3D printing technologies, the printing resolution came down up to 1 μm by two photopolymerization techniques. Fig. 1.4 shows the different microfabrication 3D printing process, their resolution, and the material feasibilities. However majority of the micro additive process deals with UV curable polymers, nanoparticle suspension and hydrogels and very few process has capabilities to process the metal for microscale fabrication.



Figure 1.4 Micro-Additive manufacturing Techniques. [4]

For metal printing, micro-transfer printing has shown in potential for the printing of multi layer structures. The process involves stacking tiny layers of prepatterned sheets of a material on top of each other, often using an elastomeric stamp to pick-and-place the prepatterned sheets, resulting in 3D structures as shown in fig. 1.5. The process involved the placing the sonsecutive layer of the thin film hence the adhesion between

the two layers is limited that restrict the usage of this process in the microelectronics devices.

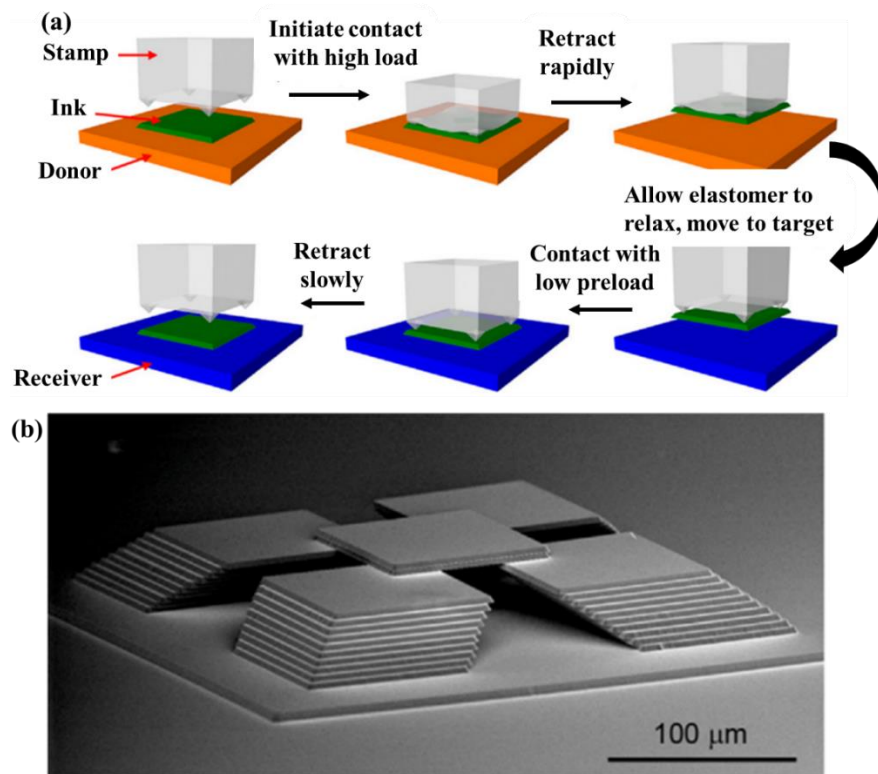


Fig. 1.5 (a) Micro-transfer printing mechanism for metal printing and (b) silicon thin film stacked on silicon substrate. [8]

Similar to Ink-jert printing principle, a micro metal droplet based additive manufacturing is an emerging technique for printing metal droplets for microfabrication. The uniform metal droplets are used as the building block of three dimensional structures. It does not require any specific form of raw material or costly equipment for processing, hence it is most favourable technologies for the microfabrication in industrial scale. The metal droplet ejection is performed by two different methods:

1. Continuous Jet mode
2. Drop on Demand mode

In continuous mode, the molten metal will start ejecting through tiny orifice in laminar flow with constant pressure and the jet will be disturbed by weak perturbation to break the jet into uniform size micro droplets. While in drop of demand mode, the molten metal droplets are

ejected by applying a mechanical vibration or pneumatic pulses. The droplet size will be the function of pulse frequency, amplitude of the vibration source and the orifice size. The DOD provide better controllability for the micro based three dimensional structure by proper integration with motion stages. [9] Fig. 1.6 shows the micro metal droplet-based 3D printing for microfabrication. The process is restricted to low melting point material such as lead, Tin for soldering.

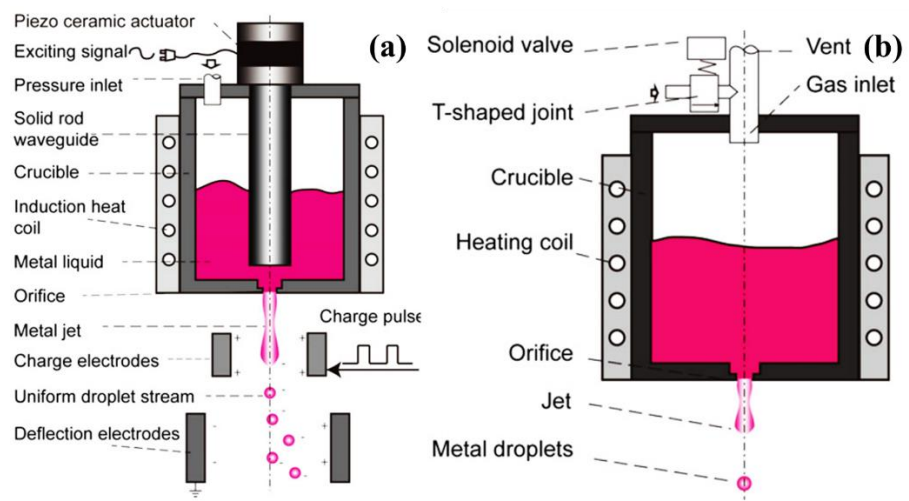


Fig. 1.6 Schematic of micro metal droplet based 3D printing with (a) continuous jet ejection mode and (b) drop on demand mode. [9]

Selective laser sintering is generally deployed for printing the feature size of 25-40 micron which limits the usage in metal processing in microfabrication. It is worth noticing that the resolution of metal-based 3D printing processes was sometimes restricted to the range of 100 μm with waviness or roughness in the order of several 10 μm , necessitating chemical or heat-based post-treatments up to two decades.

Most of the above-mentioned 3D printing/additive manufacturing technologies used photoresist, wire, or powder as feed stock material for microfabrication printing which constraint the deployment of these technologies for MEMS application. In this regard, the laser-induced forward transfer (LIFT) is an alternative technique that can be deployed for three-dimensional printing in a layer-by-layer fashion. In the LIFT

process, a thin film is used as feed stock material for printing high-resolution material selectively for sensor fabrication. Almost most of the material can be deposited in the form of thin film by physical vapour deposition, chemical vapour deposition, spin coating, etc. Hence it is easy to prepare feed stock material for this technique and accelerate the production of sensors for different industries.

1.3 Laser-Induced Forward Transfer

In LIFT, the material to be printed is coated as a thin film on the transparent substrate, and the pulsed laser beam is focused on it, which locally induces high pressure at the interface and ejects the material in the form of droplets or pellets. The ejected material will print on another substrate placed closed to each other as shown in Fig. 1.7. The LIFT is a non-contact technique that allows a wide range of metals, compounds, and biomolecules.[10–17] It does not require the usage of cleanroom equipment or the presence of vacuum making it consider device fabrication with a wide range of substrates and materials for processing. However, the if we compare it with the well -establish ink jet printing, LIFT has design freedom for printing high-resolution 2D printing of various functional high viscous ink that can avoid the nozzle clogging problem.

As the result of direct laser interaction with material, the mechanism involves heating, melting, and vaporization of material in a short period which can change in phase and composition and induces a change in the mechanical and thermal behaviour of printed structures. To be fully compatible with the largest possible spectrum of materials, the transfer phase must occur with minimum or no alteration or modification of the donor material when it releases from the donor substrate. This is crucial because many materials, particularly complex multicomponent and multiphase systems, can experience irreversible changes during melting or vaporisation, degrading the functional properties of printed structures.

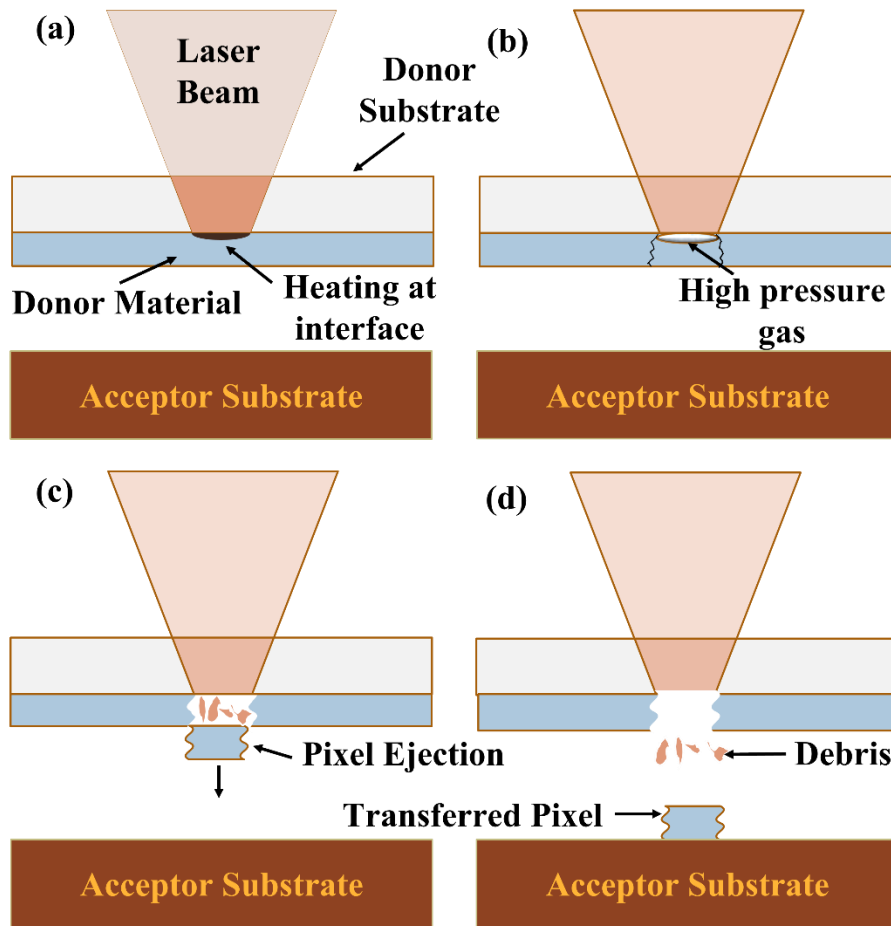


Fig. 1.7 Laser Induced Forward transfer mechanism.

To retain the functionality of the material a sacrificial layer or dynamic release layer can be introduced between the substrate and donor film. The dynamic release layer absorbs the laser energy and forms the high-pressure vapour pocket. These vapours exert pressure force on the donor material to initiate the ejection mechanisms. The process was renamed as DRL-LIFT or Laser decal transfer process for μ -3D printing as shown in Fig. 1.8. The laser energy absorbs the entire energy in the sacrificial layer and induces the necessary thrust force for the transfer mechanism. Since the laser energy is not interacting with donor film and printing is performed by mechanism thrust which helps to retain the functionalities of printed structure similar to donor film.

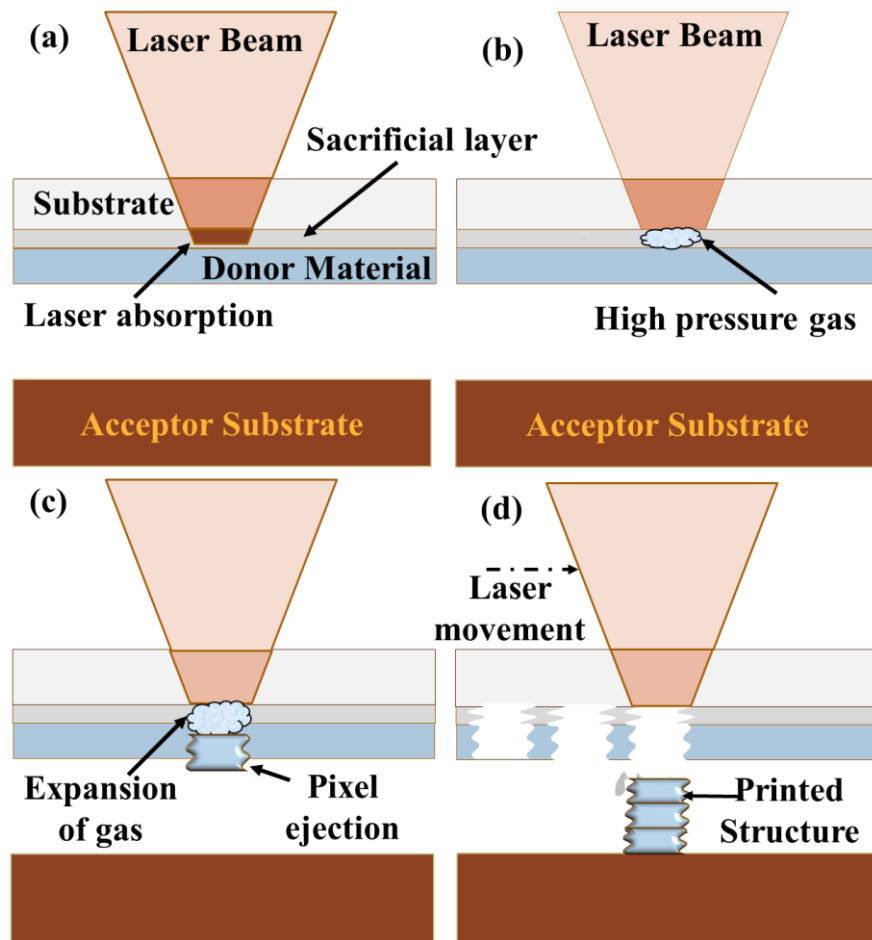


Fig. 1.8 Laser decal transfer based μ - 3D printing mechanism.

Generally, laser decal transfer can be more suitable for different biological molecules and observed the survival and proliferative ability of the deposited proteins, cells and DNAs remain constant after the deposition. A similar phenomenon is observed in the deposition of organic and inorganic polymers where the laser irradiation may damage the structure of the polymers hence the DRL is applied for the deposition of polymers based functional devices for the electronics components.[18–20] Moreover, the LFT can deposit ceramic materials using the DRL-LIFT phenomenon, but the resolution of ceramics is not as good as in the case of metals and polymers.[21]

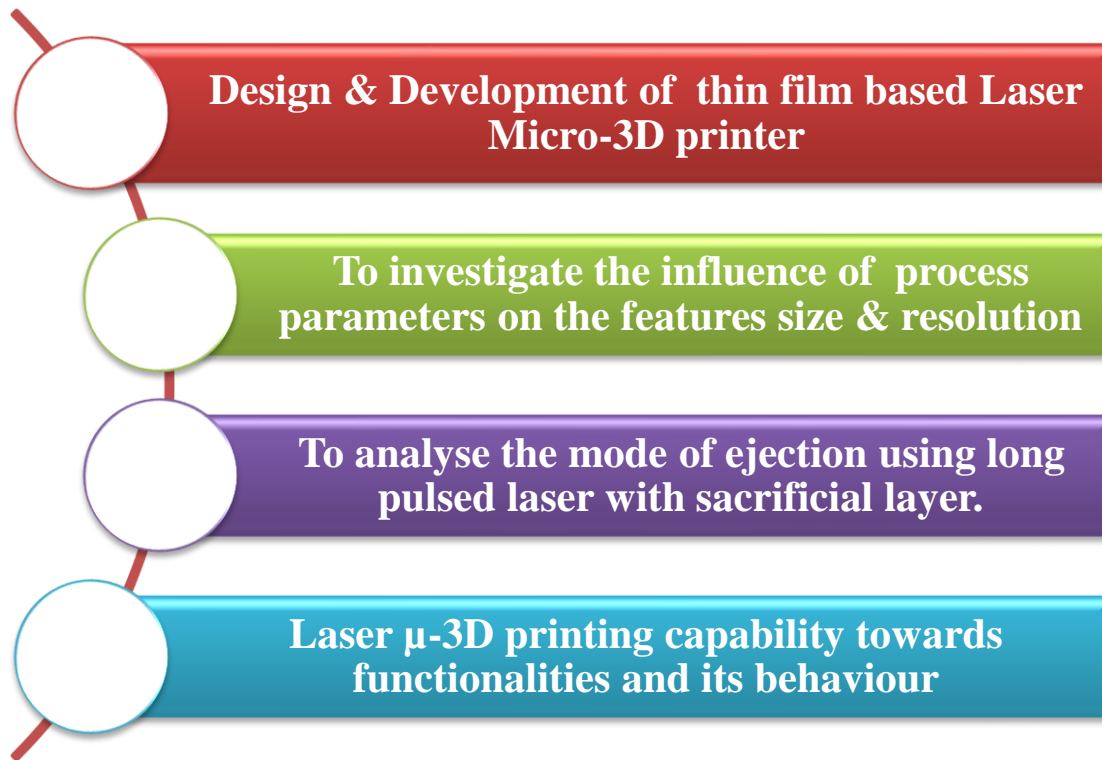
For the microfabrication of sensors and devices, laser μ -3D printing is performed by pixel-by-pixel transfer in a layer-by-layer fashion for a three-dimension microscale structure.

1.4 Motivation for the thesis:

The constraints with conventional microfabrication systems limit the usage of MEMS devices. Hence it is important to explore new innovative approaches to overcome the limitation of current microfabrication systems. In this regard, additive manufacturing has shown its potential for printing high-resolution, more intricate, and more efficient systems for macro-scale MEMS applications. Most of the metal additive manufacturing process use powder or wire form as feed stock material which limits the usage of innovative techniques for various applications due to the unavailability of material in the market. Also, despite novel developments in additive manufacturing, the printing of nano and micro-scale metal-based manufacturing is still a challenging task. The current 3D metal printer faces limitations in low layer thickness printing, inability to print wide varieties of material and low printing speed. In this regards, laser μ -3D printing provides freedom towards low layer thickness (0.5 μm to 1 μm) and high production rate for metal printing in microelectromechanical systems. The laser μ -3D printing provides thin film-based printing process without changing its phase. It has multimaterial and multilayer printing capabilities for printing three-dimensional structure.

1.5 Objectives of thesis

The main aim of the thesis is to develop a thin film-based laser μ -3D printer for printing micro-scale complex structures for MEMS applications. For achieving this, the following main objective will be addressed in this thesis work.



1.6 Significant contribution

The proposed μ -3D printer overcomes the limitation of current microfabrication techniques and additive manufacturing for the fabrication of sensors and actuators in MEMS devices. The developed printer will open a new way for industries to explore new device fabrication in microfluidic systems, microelectronics, biomedical and sensing applications.

1.7 Organisation of thesis

The thesis is divided into eight chapters as mentioned below:

Chapter 1: Introduction

Provides the general introduction, and background of the topic, motivation, objectives, signification contribution and outline of the thesis.

Chapter 2: Overview of Microfabrication Techniques.

Consist of a comprehensive literature survey of microfabrication techniques, laser-induced/decal transfer, and micro-scale 3D printing with its limitations.

Chapter 3: Theoretical Simulation of laser decal transfer in COMSOL Multiphysics

Details description of finite element modelling in COMSOL Multiphysics Software and estimate the temperature produced at the interface.

Chapter 4 Experimental Setup Specification

Description of developed experimental setup, equipment, and materials, with different characterization techniques.

Chapter 5: Process optimization of NiTi using Laser μ -3D printing.

Parametric investigation of process parameter of laser μ -3D printer of NiTi metal.

Chapter 6: Particle dynamics Study using long Pulse in μ -3D printing.

Describes the mode of ejection of donor material and correlates the resolution of printing.

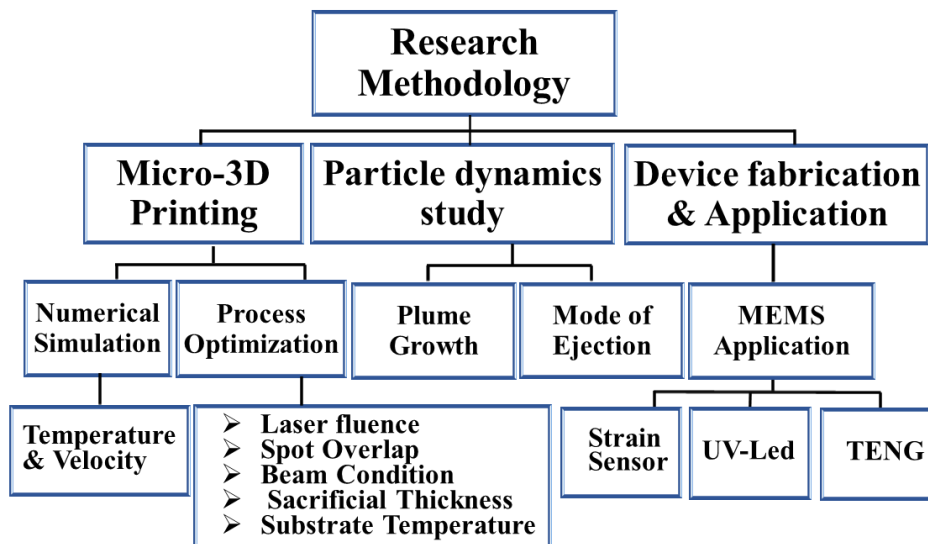
Chapter 7: Competences of μ -3D printing μ -scale structures for MEMS Applications.

Shows the process capabilities of μ 3D printer for device fabrication in different applications.

Chapter 8: Conclusion and Scope for Future Work.

The outcome of the work and possible future scope

1.8 Flowchart of Thesis



Chapter 2

Literature Survey

2.1 Overview of laser Induced Forward Transfer

The laser-induced forward transfer is the most versatile fabrication process to deposit a micron-size structure with relatively lower resolution and wide varieties of materials compare to other direct writes techniques. The straightforwardness of this method and its high compatibility led to applying this method to the diverse field of materials such as metals, oxides, semiconductors, polymers and biomaterials. It does not require any post-processing after the fabrication of functional devices for further operation.[21–23] It can print the function devices with high resolution ($<1\ \mu\text{m}$) and the capacity to fabricate high aspect ratio micropillars which can be used for the photonics, biomedical and electronics industries.^[13,14,15]

In 1970, Levene et al. reported the transfer of black ink from a polyethene-backed typewriter ribbon and coloured dyes in an open environment at a 100-200 μm donor-receiver spacing gap with Nd:YAG laser[26]. It shows the high-speed and straightforward transfer capability of the process based on the melting and vaporization of donor material. Unfortunately, it was unnoticed by the researchers for two decades. For the first time, Laser-induced forward transfer term was introduced by Bohandy et al. for the Cu metal transfer on the fused silica substrate using the excimer laser (wavelength 193 nm pulse width 15ns) in a vacuum.[27] The laser pulse is focused on the cylindrical lens to deposit the continuous line of 50 μm width. The resistivity measurement shows that LIFT-printed copper have 3 to 15 times more than the bulk values of copper. After the successful deposition of Cu lines, the same group tried to deposit the Cu and Ag with 532 nm laser wavelength using a frequency-doubled ND: YAG laser.[28].The proposed model for the solid metal donor is based on heating, melting, and vaporization. When the comparable threshold laser fluence (J/cm^2) irradiates on the donor substrate, it melting and partial vaporization takes place. As the laser

pulse interacts with donor material four different process takes place before transfer: (a) The front surface of the film is heated by the laser pulse until it melts; (b) the melt front travels across the film as long as it touches the rear surface; (c) at this point, or just prior to the melt across, the front side is superheated or very close to the vaporization temperature; and (d) at this point, or just before the melt through occurs, the metal vapour pressure at the back surface push the molten liquid to the acceptor substrate where it becomes solid as a metal feature.[28][29].

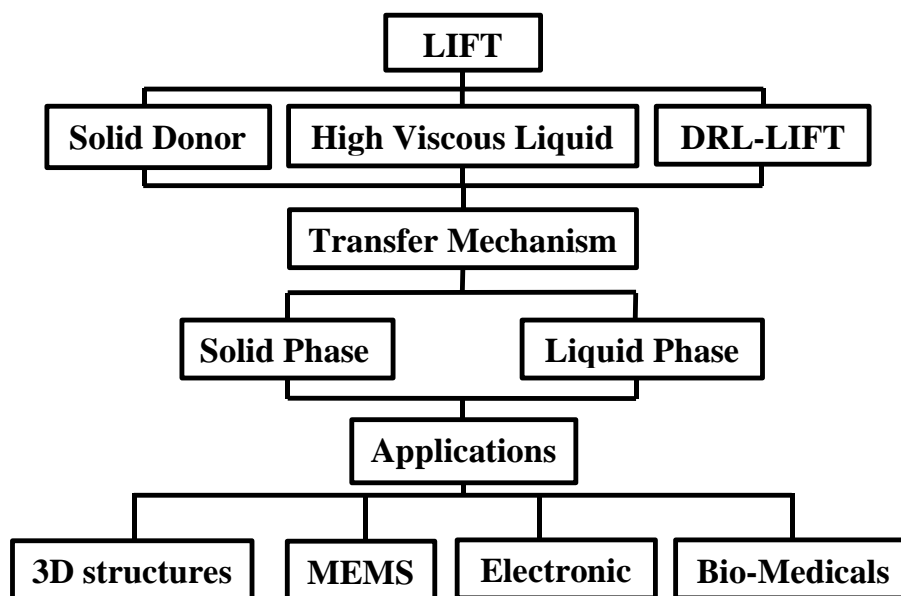


Fig. 2.1 Flow chart of literature survey

2.1.1 Solid Donor

When the temperature at the interface is not sufficient to melt the solid donor, the transfer happens in the solid phase. The size of the transferred pellets is close to the laser beam diameter. **In solid donor two material transfer takes place with two different mechanism** (a) Blasting mechanism and (b) Thermomechanical film tearing-off [11]. In the blasting mechanism, the heating of the interface results from desorption by donor substrate surface defect that creates vapour pockets which exert high pressure on the solid film. When t is the most common used his pressure exceeds the fracture limit of the donor thin film,

pellets will release from the donor substrate and propelled to the receiver substrate.

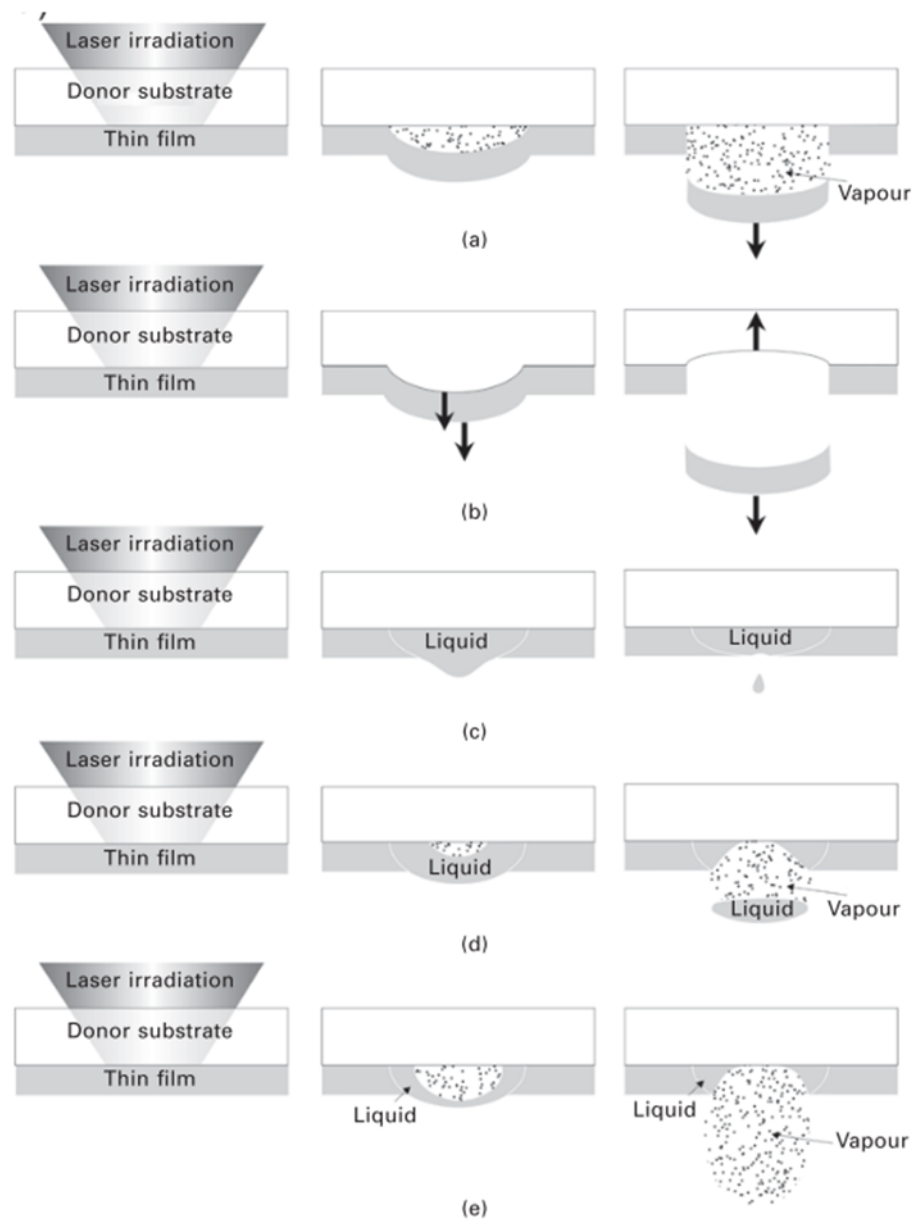


Fig. 2.2 Different mode of transfer mechanisms of LIFT without sacrificial layer at different laser fluences. (a) film fracture & partial vaporization at fluence; (b) thermal expansion and film peel-off at low fluence; (c) phase change melting at threshold fluence; (d) small volume ablation & melting at high fluence, and (e) vaporization at very high fluence [30]

In the case of Thermomechanical film tearing, heating of film generates thermal radial expansion which is accounted for a radial compression force that creates a transverse tension in the donor film. This transverse tension is perpendicular to the donor substrate towards the receiver. As a result, when this force exceeds the adhesion force with a substrate, the film gets ripped off from the donor and deposited in the acceptors' substrate. This mechanism gives the best deposition without any fragmentation with poor adhesion on the acceptor substrate. [31][32] The laser fluence just above the threshold fluences melts the thin donor film and the deposition takes place in the molten forms.

At laser fluence higher than the donor threshold limits, the irradiated regions vaporized before the expansion process ends, and the transfer takes place in the vapour form.[32] This leads to the deposition of smaller thickness material. The volume of evaporation is determined by the donor thickness and deposited material thickness on the substrates. Fig. 2.2 shows the proposed different transfer mechanisms for the solid donor thin film. The major limitation in this fluence is the shape of the pellets get shatters or even fragmented into different pieces. This can be avoided by using a digital micro-mirror device (DMD) for spatial beam shaping. DMD modulated the laser beam on a per-pellet basis and varied the intensity of the laser beam according to the different required shapes.[33][34]

The crucial challenge of the LIFT process is the generation of large mechanical thrust for the transfer of brittle materials or thicker layers in the solid form. For such cases, two different strategies were developed by the researchers. First, an ion beam is used to pre-machined 1 mm thick zinc oxide (ZnO) films up to the 0.8 mm depth, and then LIFT is used for the transfer mechanism. The pre-processing using an ion beam reduces the energy requires to break the remaining part of the donor film from the substrates and produces the debris-free micro-pellets of ZnO with extremely smooth edges and surface uniformity [35]. Second, employing laser beam shaping, that corroborates the energy to break the thick film. Two different laser fluences having different beam profiles

are merged to generate a high fluence at the edges and low fluence at the centre of the beam profile as shown in fig 2.3. The merged beam profile allows the process to deposit organic polymers for higher thickness than 1 μm without any damage as well as better resolutions [18].

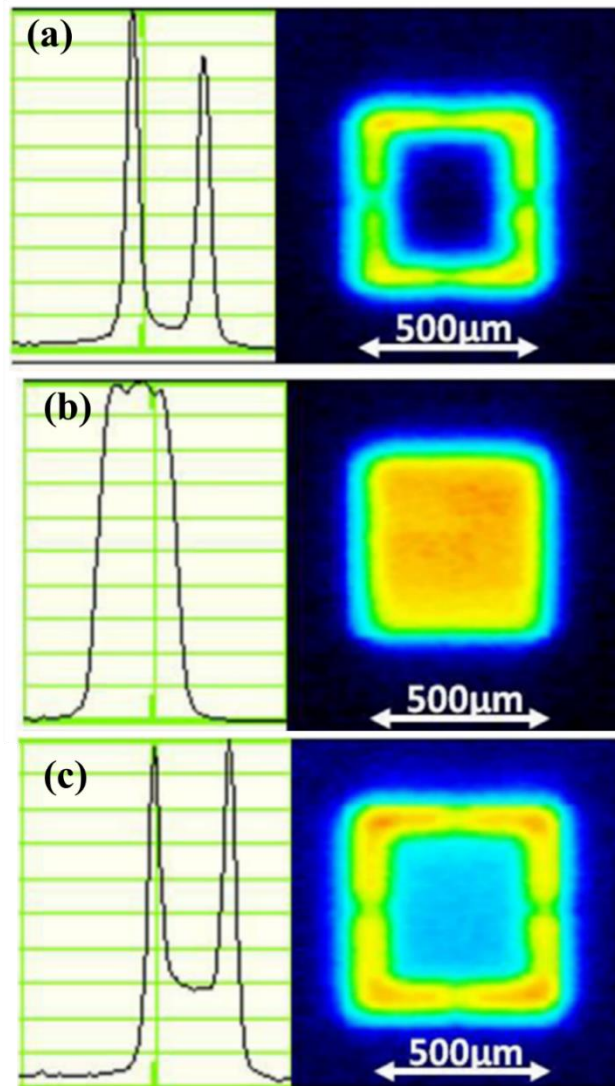


Fig. 2.3. Laser Energy profiles of different shaped beams: (a) edges-beam 1, (b) centre-beam 2, and (c) beam 1+beam 2. [18]

2.1.2 Liquid Donor

One of the advantages of LIFT is that it does not require a nozzle which avoids the clogging problem in inkjet printing, and there is no restriction on the rheological properties and viscosity of the ink or nano pastes. Various biological solutions including mouse fibroblast or storm cell, DNA, proteins [36][37], inorganic ink or paste and organic polymers

were printed for different functional applications like micro-batteries [38][39], solar cells [40][41], organic light-emitting diode [42][43] and biosensors ([44–46]). More literature is available for the parametric investigation of process parameters (laser pulse width, laser fluence, DRL layer thickness, donor film thickness and donor-receiver spacing) on the morphology (deposited shape, volume, and roughness) of the deposited materials.

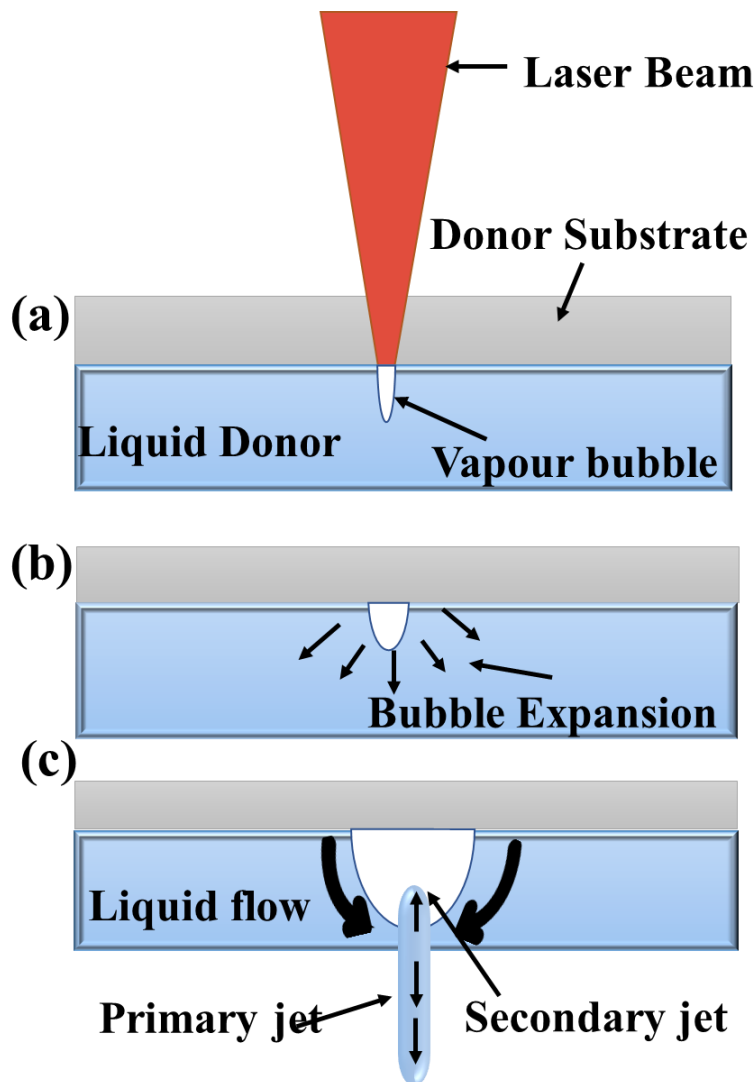


Fig. 2.4 Principle of operation of liquid transfer a) vapour bubble formation due to laser absorption (b) initial expansion of the vapour bubble (c) jet formation. [31]

The mode of operation with the liquid film is similar to the solid film, with the only difference being the state of the donor film and the thickness of donor materials. The transfer material is suspended in the

solvent to form an ink or paste which is coated on the transparent donor substrate. As the laser pulse irradiates the ink or suspension, a small amount of ink gets evaporated and generates plasma that induces high-pressure vapour bubbles in the liquid suspension. Due to the expansion of high-pressure bubbles, the pressure inside the bubbles decreases. The size of bubbles increases more towards the free surface of the donor layer because less amount of material is available to restrict the flow. As the pressure inside the bubbles falls from surrounding pressure. The reverse process starts growing hence the materials from the surrounding drawn to form a primary jet in the receiver substrate direction and a secondary jet toward the donor substrate.[47][48] A schematic shows the laser irradiation on the liquid film and bubble formation, as shown in fig 2.4. It can be noticed that the transferred materials are not overheated unlike in the case of solid donors hence this method can be used for the deposition of highly sensitive materials like inorganic materials, and fragile materials (biomolecules or even living cells).

2.1.3 Dynamic Release Layer (DRL-LIFT)

While transferring from the donor to the receiver substrate the donor material undergoes different thermal processes like heating melting and vaporization. This would affect the material characteristics of the transferred deposits with donor thin film. To avoid any thermal effect, the thin sacrificial layer is introduced in between the donor substrate and thin film (known as Dynamic Release Layer) to protect the donor material from the laser pulse heating during the transfer mechanism. The DRL is deposited on the transparent donor substrate with physical vapour deposition (sputtering, and thermal flash evaporation), doctor blade and spin coating. When the laser pulse fluence greater than the threshold fluence interacted with DRL, melting and vaporization takes place. During the expansion of the vaporized layer, it pushes the donor thin film toward the acceptor substrates shown in fig 2.5. Since there is no interaction of laser pulse with donor thin film, hence it deposited without any physical change in the transferred material. [49]

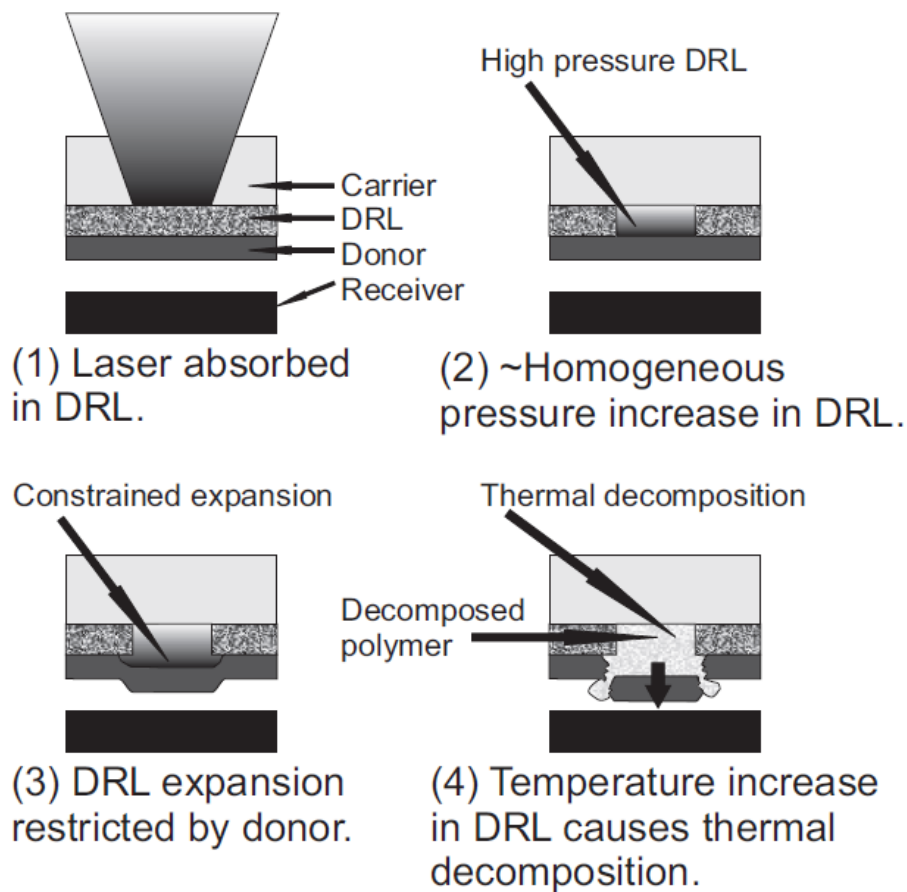


Fig. 2.5 Schematic of Dynamic Release Layer-LIFT (DRL-LIFT).

The metallic **DRL is mostly** used in LIFT for thermal sensitive materials toward laser radiation. These metallic thin films Ti [36], Au [16], Pt, Cr [20] are biocompatible and easy to coat using a physical vapour deposition technique or sputtering on the transparent substrate i.e., Quartz substrate. These metals absorb most of the laser radiation within the 100nm thickness for laser wavelengths 532nm and 1064 nm and ensure that the laser radiation is not reaching toward the donor thin films. The first work reported with 60 nm thin Titanium DRL for the transfer of salmon sperm DNA on the poly-L-lysine coated substrate. It revealed that the Titanium does not hinder the adhesion and transfer of DNA to the poly-L-lysine coated substrate. Even though the successful printing of biomolecules, metallic DRLs have the disadvantage of contamination of transferred material during the melting and vaporization process which affects the fabrication and performance of organic microdevices. Generally, the thickness of metallic DRL and the polymer DRL are in

the range of 20-100 nm and 1-5 μm respectively. The thick Polymeric DRLs overcome the limitation of metallic DRLs. In the case of polymeric DRLs, the photothermal and photochemical decomposition of organic molecules gives vapour as a by-product. Photo-decomposing polymer absorbs the laser radiation and decomposes in the gaseous fragments generating high-pressure bubbles for the transfer. Therefore, transferred material is deposited without any physical or phase change with the donor film. Triazene polymer (TP) is a widely used photo-decomposable DRL as a sacrificial layer for thermally sensitive materials (i.e.; organic nano pastes, inorganic polymers, and biomolecules) to avoid contamination in transferred material[49–52][53]. Due to having a wide range of absorption spectrum, numerous studies focused on different laser wavelengths. A solid disc of GdGaO of 10 μm diameter was deposited using aryltriazene as a DRLs layer with Ti: Sapphire laser ($\lambda = 800 \text{ nm}$ and $\tau \approx 130 \text{ fs}$) without any shattering at optimal donor-receiver spacing[50]. Aluminium, Gelatine, and Methylcellulose were transferred from the donor substrate using triazene as the sacrificial layer with a XeCl excimer laser ($\lambda = 308 \text{ nm}$, $\zeta = 30 \text{ ns}$). It was found that the laser fluence and the DRL thickness are strongly dependent on the mechanical properties of the transferred materials [49]. One of the most significant achievements in the LIFT is the deposition of an Organic Light Emitting Diode using triazene as DRL. The transparent Tin doped indium tin oxide large amount of pressure (ITO) was used as an anode and acted as a receiver substrate. On the donor substrate, cathode, and electroluminescent materials an aluminium of 80nm / MEH-PPV-90nm (poly [2-methoxy-5- (2-ethylhexyloxy)-1,4-phenylenevinylene]) bilayer was deposited over the 100nm TP layer. The laser fluence of 250mJ/cm² was applied for the transfer of the cathodic part using the XeCl laser ($\lambda=308\text{nm}$) [43].

2.2 Time-resolved Shadowgraphy

The material is transferred from the donor to the receiver substrate within a fraction of the time after the laser irradiation. Hence the time-resolved shadowgraphy technique is used for tracking transfer materials at different time frames. The process is monitored using a high-speed camera with a long-distance microscope objective lens that is focused normally on the laser beam direction at the bottom surface of the donor film. A secondary illumination source (laser source) is used for proper tracing of the deposited pellet/droplets. The illumination source is triggered with an external pulse delay generator that gives signals to it after some time delay to the laser irradiation. Material is transferred in two different phases: solid phase and liquid phase transfer.

2.2.1 Solid-phase transfer

The solid phase transfer is observed in the DRL-LIFT where the sacrificial layer is used to absorb the laser irradiation and generates a shock wave that is responsible for the material transfer in the solid form in an open atmosphere. This shock wave is generated due to the ablation of the sacrificial layer. R.fardel *et al.* studied the solid phase transfer mechanism of an 80nm thin Aluminium donor with the triazene polymer as the DRL layer.[21] Fig. 2.6 (a) presents the time-resolved images at different time frames with laser fluence 50-260 mJ/cm². The generated shock wave is visible in 1 μs images at all the laser fluences and an over pressure gas is flowing around the edge of the pellets. The over-pressure gas is released due to ablation of the TP DRL layer and is responsible for the detachments of fragments from the solid pellets. It can be observed that the velocity of pellets increases with an increase in the laser fluence and the pellets at laser fluence 50, 200 and 260 mJ/cm² fragment after travelling for 1 mm and moves faster than pellets. This is due to pellets having more surface area than the fragments hence it experience more drag force which reduces the velocity of pellets.

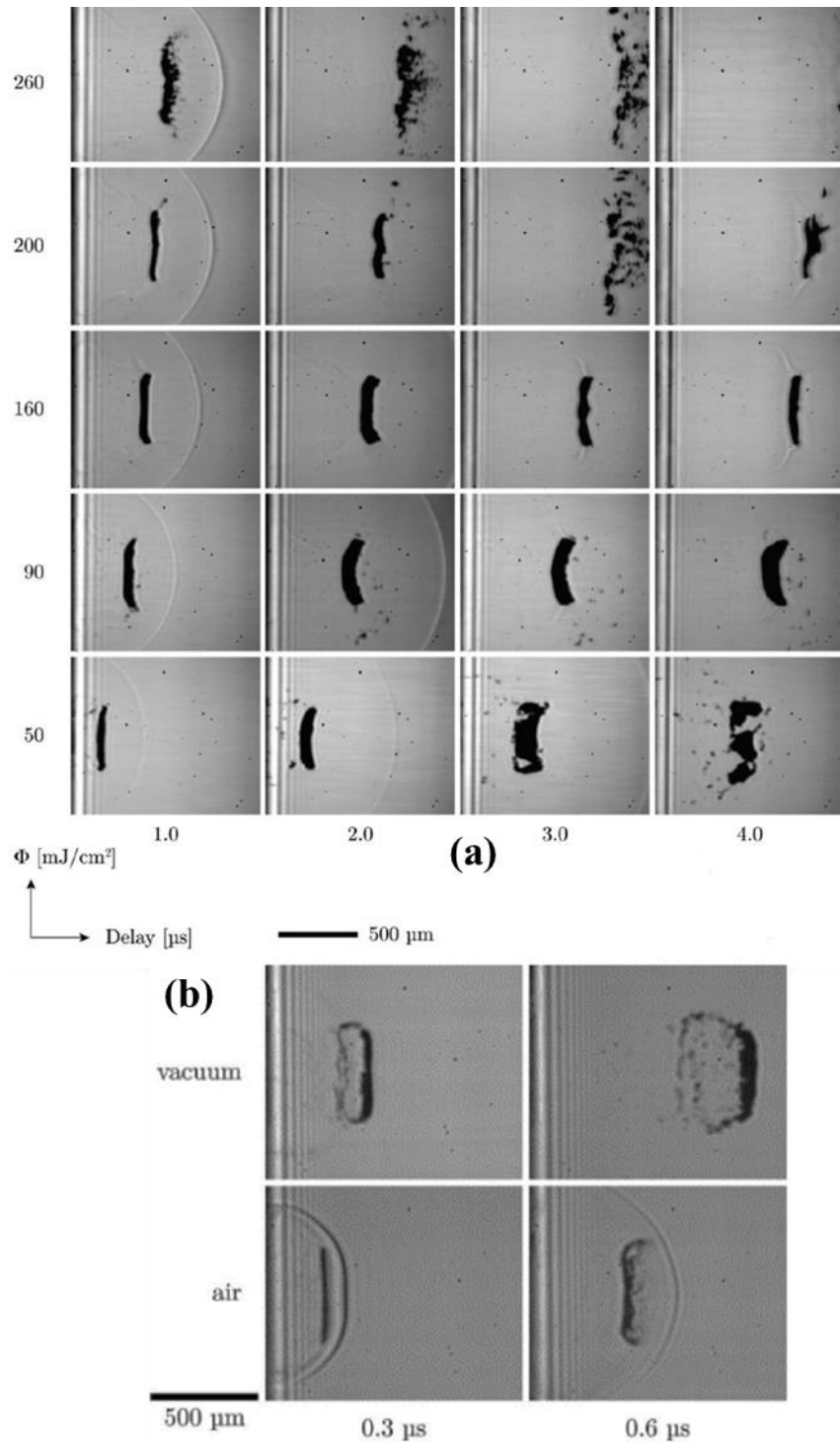


Fig. 2.6 Time-resolved image at different time frames with a donor film of 350 nm TP/80 nm Al (a) at different laser fluences and (b) at laser fluence 280 mJ/cm² in vacuum and air condition. [54]

Fig 2.6 (b) shows the time-resolved image at different frames in vacuum and atmospheric conditions. In vacuum conditions, there is no medium for propagation of shock waves and the air drag is absent results higher

velocity of pellets without shock waves. Even the decrease in laser fluences does not overcome the problem of high velocity rather than the quality of ejected flyer decreases at the lower fluences. [54] The solution to this disintegration is to compromise between the shock wave and the velocity of the flyer by using intermediate gas pressure between the vacuum and the atmospheric condition. P. Delaporte et al. suggested that Gas pressure between the 10 mbar to 100 mbar allow safe condition for better transfer of flyers for most of the materials [55]. Moreover, the velocity of the flyer also depended upon the laser pulse length (nanosecond and picosecond). The absorption depth in picosecond laser is less compared to nanosecond laser which corresponds to less ablation volume in the sacrificial layer. Hence the pressure developed by picosecond laser will generates higher velocity of the shockwaves[56].

2.2.2 Liquid phase transfer

Lee *et al.* studied the dynamics of metallic lift-off film with pulsed ND: YAG laser ($\lambda = 1064\text{nm}$, $\zeta = 250\text{ns}$) and reported that the plume is propagated perpendicular to the incident laser beam with a velocity equal to 0.75M in open-air condition [57]. Similarly, Young *et al.* investigated the dynamics of “matrix-assisted pulsed laser evaporation based direct write” MAPDLE, used for the deposition of organics, polymers, metals, and composites, with Nd: YAG laser ($\lambda = 355$ and $\zeta = 150\text{ns}$) with ultrafast microscopy and observed the plume velocity nearly 0.2 km/s [58]. Later on, different researchers studied the LIFT dynamic for the optimization of process parameters.

Duocastella *et al.* studied the systematic investigation of dynamics of liquid at the different laser fluences to understand the dynamics of material flow from the donor film [59]. The Nd: YAG laser beam ($\lambda = 355$ nm and $\zeta = 10$ ns, 1 Hz repetition rate), is focused on the top surface of liquid donor film. The liquid mixture of water and glycerol, both at a concentration of 50% (v/v), plus the surfactant sodium dodecyl sulphate dissolved at a concentration of 2.0 mg/ml. A titanium layer of 50 nm is coated over the donor substrate which acts as the DRL layer for the transfer mechanism. In fig. 2.7 it is observed that two different lumps

are generating opposite to each other, the upper lump is due to the reflection of the downward lump because of the high reflectivity of Ti coating on the donor substrate which acts as a mirror. The transfer mechanism takes place due to the laser irradiation of DRL layer generating plasma which induces the high-pressure vapour bubbles. At laser fluence lower than the threshold limit, a lump is generated as the laser irradiated the liquid film and starts growing up to $1.4\ \mu\text{s}$. With high surface tension and the resistance from sidewalls, it collapses while the central tip of the lump maintains its progression to form a jet up to $4.1\ \mu\text{s}$. Due to insufficient driving force for further expansion, these jets move back to the donor film resulting in no deposition on the receiver substrate. In fig. 2.7 (b),(c) the same phenomenon demonstrated initially with a large size lump until jet formation starts. At higher fluence (more than $5.6\ \text{J}/\text{cm}^2$), a large generated heat is transmitted to donor thin film pressure is developed that forms balloon-like vapour bubbles. The vapour bubbles push the liquid material in front of it to form the liquid jet. Once the proper jet is formed, it starts thinning with an increase in the length of the jet leading to form a high aspect ratio jet. As the process continues, continuous thinning yields the breaking of the jet into multiple droplets. This leads to a change in the morphology of the deposited materials. The formation of multiple droplets depends upon the laser fluence applied, as shown in fig. 2.7 (b) ,(c). In the case of higher fluence, the lump starts forming up to 580ns , while due to high pressure generated inside the vapour bubbles yield to bursting from its tip resulting in the deposition of fragmented droplets on the receiver substrates. Further, studies have been done to investigate the effect of particle size, the viscosity of the suspension, laser fluence, film thickness on the morphology of deposited droplets[48,60–64].

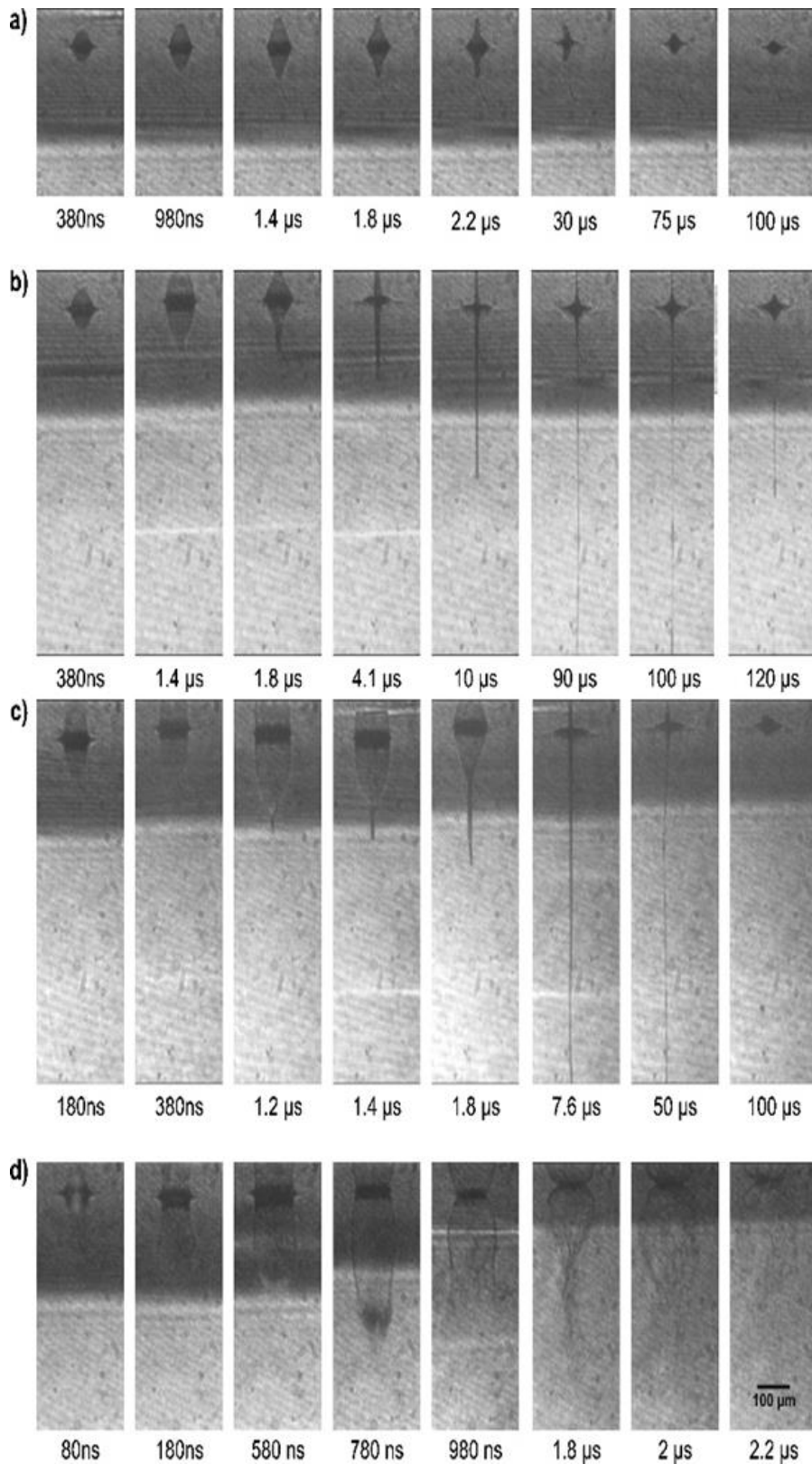


Fig. 2.7. Shadography images at different time frames after laser irradiation in the LIFT process at laser fluences: (a) 1.2, (b) 2.4, (c) 5.6, and (d) 10 J /cm². [59]

J. Miksys *et al.* studied the effect of laser pulse duration nanosecond ($\zeta = 30$ ns) and picosecond ($\zeta = 10$ ps) on the ejection velocity and morphology of the deposited nanoparticles. The nanosecond laser has more thermal diffusion length (45 times larger) than the picosecond laser for the same laser fluence. Hence the volume of vapour bubbles is more in the nanosecond laser while the picosecond laser form more confined vapour bubbles with high pressure at the interface of the donor film and substrates. This means the picosecond laser generates higher ejection velocity and more surface area of bubbles formation. In the case of higher fluence, picosecond laser generates high pressure inside the bubble and inducing more shear in the donor film results in the viscosity drop of donor materials. This drop-in viscosity yield to more amount of flow, resulting in higher velocity and a larger surface area of bubbles [65]. Similarly, A. Kalaitzis *et al.* studies the ejection regime of Newtonian and non-Newtonian ink with nanosecond laser during the LIFT process and observed that laser reduces the viscosities of non-Newtonian ink to lower than the nominal value. Both the ink shows similar ejection regimes as reported by J. Miksys *et al.* [48].

2.3 Applications of Laser-Induced Forward Transfer:

The $L\mu$ -3DP has shown its potential in the free-standing 3D structure on the microscale by stacking 2D geometry layer by layer at the same location to fabricate 3D MEMS functional components.[66] The different donor material forms are used such as solid form, high viscous liquid ink, and polymers to fabricate the micro 3D component for the micro-actuators, sensors, electronic devices, and different functional devices for MEMS applications. Moreover, the resolutions of these devices are relatively high (order of a few microns), which corresponds to the laser spot diameters. LIFT is limited for single materials deposition, but actuators and sensing applications require multi-material deposition for different shapes. For such application, a thermocouple is fabricated with multi-metal (Gold and Platinum) using $L\mu$ -3DP techniques with pulsed Nd: YAG laser ($\lambda = 532$ and $\zeta = 4$ ns) for the

inclined - shaped high-aspect-ratio pillars.[23] It was found that due to the dispersion of molten metal, droplet diameters of $12\ \mu\text{m}$ were deposited at lower fluence for a pillar height of $1.3 \pm 0.1\ \text{mm}$ with an aspect ratio of 110.

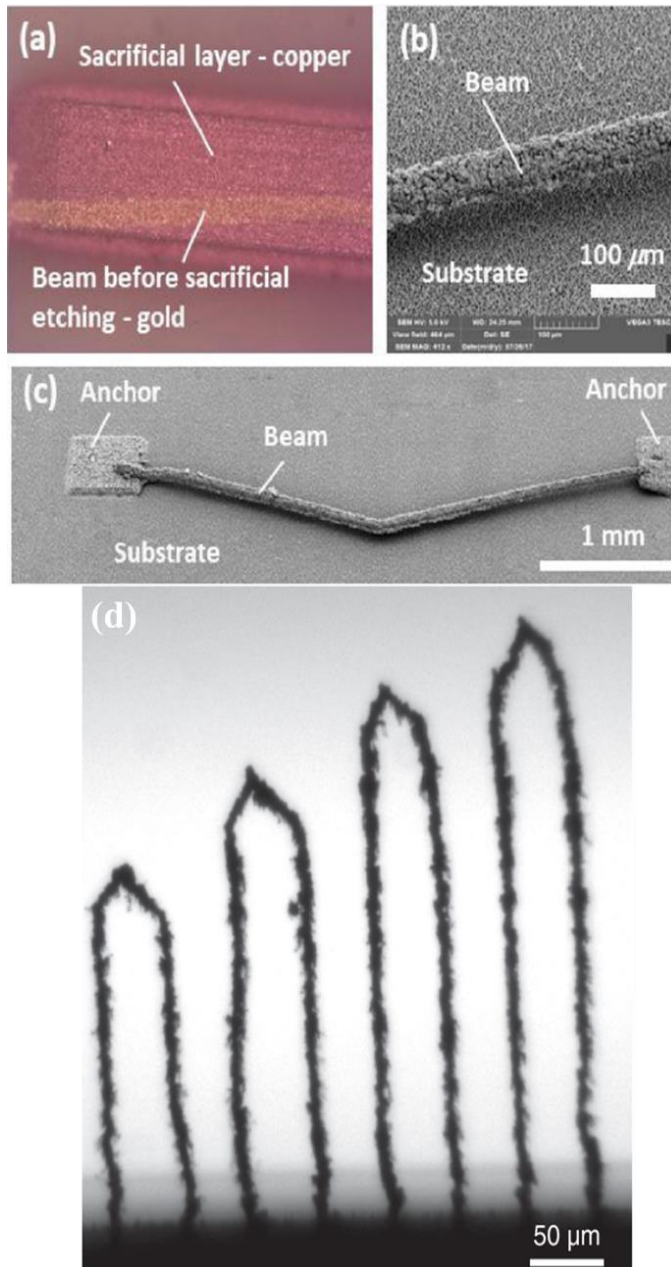


Fig. 2.8 (a) L μ -3D printed gold track printed on top of a copper support structure, (b) SEM image of the printed gold bar after etching of support, (c) SEM image of printed actuator, and (d) high-aspect-ratio multimaterial of gold and platinum structures fabricated by using ns-LIFT. [67], [23]

A free-standing 3-dimensional overhang gold structure is fabricated with L μ -3DP and chemical etching of pure metal. For the supporting structure, copper is deposited during the fabrication and removed with chemical etching in ferric chlorides as shown in fig. 2.9.[68] At threshold laser fluence droplets are probably ejected in a cap and jet regime. It is concluded that this is due to differences in viscosity, droplet impact speed and surface tension deviating from the perfect spherical shape.

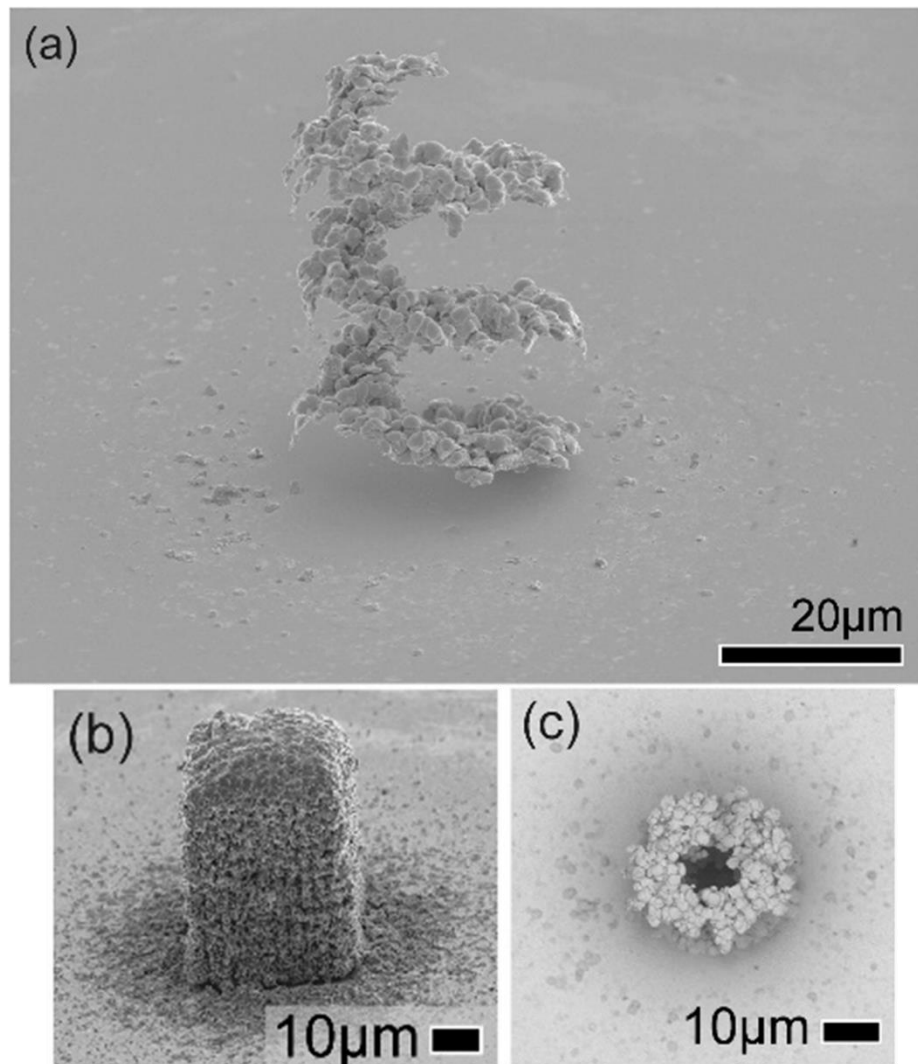


Fig. 2.9 LIFT deposited an Au helix structure (rotating out-of-plane in a clockwise direction) viewed at an angle of 60° (a) after, (b) before etching, (c) shows the helix after etching seen from the top (0°). [68]

DRL-LIFT is widely used for most biomaterials printing with a sacrificial layer such as gold, titanium, and gelatine. The above-mentioned biomolecules are mixed with hydrogel suspension having high viscosities and coated over the DRL layer. The laser irradiates the DRL layer and transfers the biomolecules. Since the laser source is not in contact with the cells, hence no stress is generated in the cell to maintain its high viability (> 95%) after the deposition. Most of the studies are related to the NIH 3T3 mouse fibroblast, salmon sperm[36] DNAs[71][72] and cells. [73]

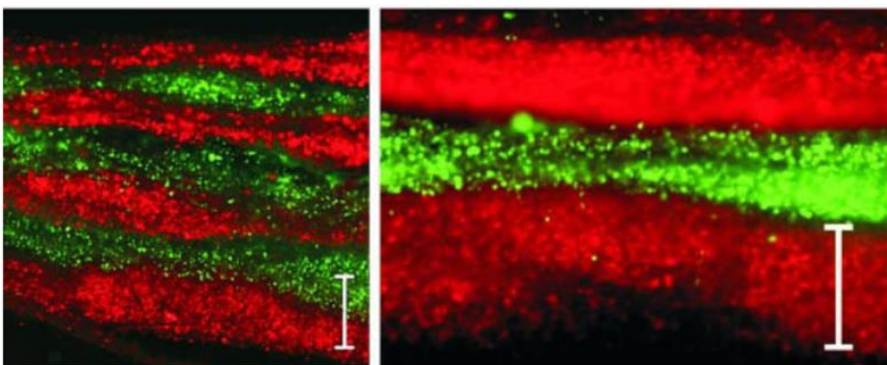


Fig. 2.10 Seven layered printed grid structure (top view) of fibroblasts (green) and keratinocytes (red) demonstrates micropatterning capabilities of LIFT. Scale bars are 500 μm . [74]

Lothar Koch *et al.* have fabricated the $L\mu$ -3D printed multi-layered 3-Dimensional cell structure based on two different types of cells (NIH-3T3 Swiss albino fibroblasts and human immortalized keratinocyte cell line, HaCaT) with the DRL-LIFT process. A 60 nm thin gold layer is used as a sacrificial layer to absorb the laser fluence and give sufficient pressure to the biomolecules donor layer for the transfer. An alternating layer of HaCaT (green) and mCherry (red) cells were printed and demonstrated its ability to fabricate the 3D cell structures.[74]

2.4 Research Gap

Several research are focused on the laser induced forward transfer of thin film in which material changes its phase due to direct interaction of laser beam with donor film. The following gaps are identified with literature survey.

- The change in phase in the donor film during transfer will change the physical properties of material. A rigorous study is required for the printing of solid pixel using a sacrificial layer for the transfer.
- The details analysis on influence of parameters on the printed solid pixels were not found.
- The solid pixels ejection and pixel deposition analysis is missing in the decal transfer process. Moreover, the mode of ejections needs to study for better understanding in decal transfer.
- Moreover, there are few literatures available using a long pulse laser system for developing three-dimensional structures which shows differences in the ejection behaviour as well as the phase transition of the donor film.

2.5 Summary

The laser-induced forward transfer shows the different pixels deposition using direct interaction of donor material with laser beam. The donor material can be either the solid thin film, high viscous fluid or by introducing the sacrificial or dynamics release layer between the donor substrate and donor film. In case of dynamic release, the material does not change its phase and retains the chemical and functional properties of the material. The particle dynamics shows the transfer of solid pixels with pressure waves and its dissociation using the short pulse after a few microseconds due to reflection of a pressure wave. However, the vacuum environment provides high particle velocity compared to open-air conditions. In the case of a highly viscous donor, a primary jet starts due to the evaporation of a thin layer of liquid while the secondary jet is due to the surface tension which tries to contract after the eject of the

primary jet. Most of the three-dimensional structures were printed by laser-induced forward transfer with phase change (solid-liquid) or (liquid-solid) that may alter the properties of the material before and after printing. From the functionality point of view, the printed structure shows a difference in mechanical and electrical properties of structures using short pulse width laser. In this regard, a laser decal transfer based μ -3D printer will be developed for printing solid thin film without phase change for three-dimensional structures.

Chapter 3

Theoretical Simulation of laser decal transfer

3.1 Temperature estimation through numerical simulation

Finite Element Analysis (FEA) is a technique that allows us to analyse complex components or systems by discretizing the entire domain into smaller elements and solving the governing differential equation for individual elements. It provides the freedom to the user to solve nonlinear problems and the coupling of two or more physics involved in the process. It leads to a reduction in production time and cost of production in the industry by reducing the number of experiments required to obtain optimal process parameters.

Theoretical simulation of laser decal transfer is performed in FEM-based COMSOL Multiphysics simulation software. In LDT, a laser absorbs in the sacrificial layer and gets ablated to form high-pressure gas hence it is essential to identify the physical mechanism of material transfer. The method involved whether in the photothermal process or photomechanical for the ejection of donor material.

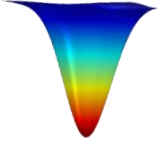
3.1.1 Thermal equation of laser material interaction

Fourier's Law of heat conduction is used to describe thermal transfer in a material by diffusion and particle collision caused by a temperature gradient. By Fourier Law "The heat transfer through a material is proportional to the negative temperature gradient," assuming the heat flow is normal to the surface. The laser energy absorbed by the material and the phase transformation is governed by the Internal energy and the enthalpy change of material. The laser source $I_0(x, t)$ is having gaussian beam profile with some pulse duration hence the energy input to the system is function of spatial and time domain $Q'(x, z, t)$. The two-dimensional heat equation is used in the simulation as shown in equation 1. Since the sacrificial layer vaporizes due to heat generated by laser absorption hence the phase change of the sacrificial layer is considered by modified heat capacity as shown in equation 2.

$$\rho C p \frac{\partial T}{\partial t} = \nabla \cdot (K \cdot \Delta T) + Q(x, z, t) \quad (1)$$

$$C p = \begin{cases} C_o & 293 < T < 550 \\ C_o + L_d * \delta(T - T_d) & 550 < T \end{cases} \quad (2)$$

Time and spatial domain of pulsed laser gaussian beam is defined in Eq. 3. The energy absorbed in the material $Q'(x, z, t)$ is the function of Laser intensity, I_o and Lambert-Beer law as shown in Eq. 4. respectively.

$$I_o(x, t) = I' * \exp\left(-2 \frac{x^2}{r^2}\right) * \exp\left(-\frac{3(t-\tau)^2}{\tau^2}\right) \quad (3)$$


$$Q(x, z, t) = I_o(x, t) * (1-R) * \alpha * \exp(-\alpha z) \quad (4)$$

Where

ρ	Material density
Cp	Modified Specific heat
K	Thermal conductivity
L_d	Latent heat of dissociation of PDMS
R	The reflectivity of thin film
α	The absorption coefficient of PDMS
r	Beam spot radius
ζ	Laser pulse width
A	Spot Area

Model geometry and Meshing

A two-dimensional rectangular block of length 2000 μm is used for the sacrificial layer and thin film of width 1.5 μm and 200 nm thickness respectively as shown in Fig. 3.1. The donor substrate is not modelled in the simulation it does not absorb the laser energy. A user-defined rectangular mesh is used for the discretization of the rectangular geometry. The laser irradiation zone and a top layer of sacrificial layer are modelled finned for a better estimation of temperature at top and central regions as shown in Fig. 3.1 (b).

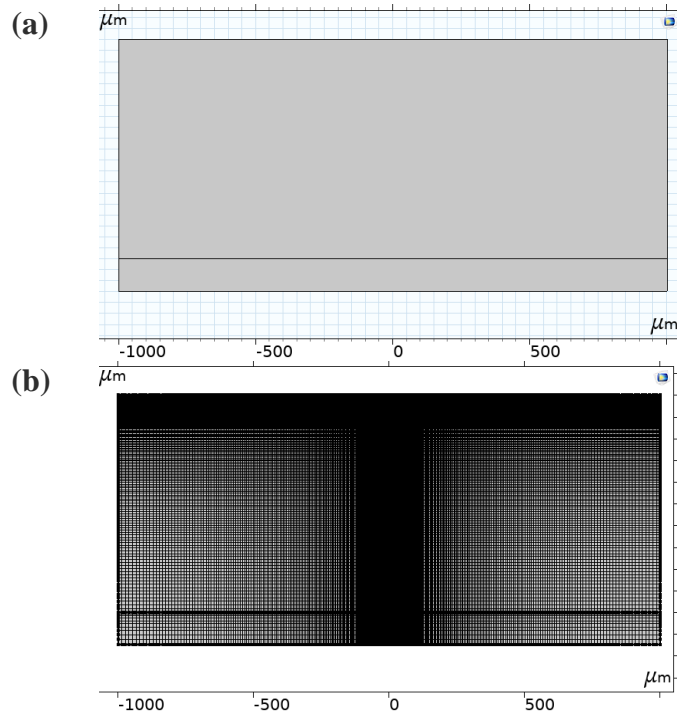


Fig. 3.1 (a) Visualization of (a) Geometrical model and (b) Meshing used in the simulation

Material Properties

The physical properties are kept constant throughout the simulation such as thermal conductivity, specific heat, coefficient of thermal expansion and density of PDMS and NiTi are incorporated in the model from the literature as shown in Table 1.[75]

Table 3.1 Material properties used in the simulation.[75]

Property	Unit	NiTi	PDMS
Heat capacity at constant pressure	J/(kg·K)	3200	1460
Density	kg/m ³	6450.0	970
Thermal conductivity	W/(m·K)	10	0.16
Coefficient of thermal expansion	1/K	$11 * 10^{-4}$	$9 * 10^{-4}$
Extinction coefficient, ϵ	μm^{-1}	-	5

Assumptions and Boundary Conditions

- The absorption coefficient of the CO₂ laser is calculated by the ratio of penetration depth in PDMS in air and in vacuum conditions.
- Material removal is not considered in simulation which leads to over estimation of high-temperature generation.
- The initial condition is taken as room temperature.
- Due to heat loss from natural convection through the air under atmospheric circumstances, the simulation's heat transfer coefficient of 10 W/(m²K), and radiation loss with an emissivity of 0.3 is taken into account as shown in fig. 3.2.
- Dissociation-induced phase change is considered. Donor substrate is not simulated in the simulation since it is transparent to laser beams.

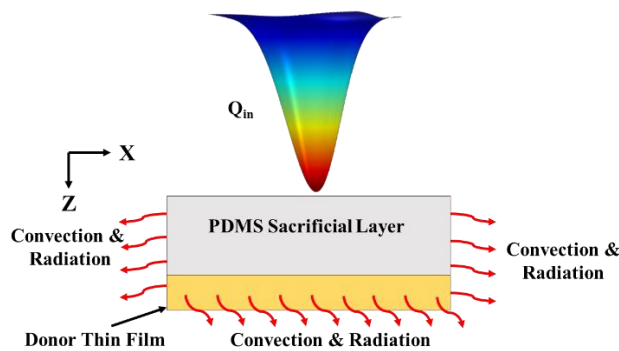


Fig. 3.2 Boundary condition and incident laser energy on modelled geometry

As a result of laser-material interaction, the laser energy absorbs in the PMDS sacrificial layer and generates heat in the system. The generated heat is transmitted to donor thin film and some energy is transferred to the surroundings via convection and thermal radiation. From table 3.1 it can be observed that the thermal conductivity of the PDMS is very low and the temperature-induced is very high results more temperature gradient between the top layer of PDMS and bottom layer of PDMS. Hence, the PDMS layer starts vaporizing from the top surface and form high-pressure gas due to vapour pressure. The high pressure leads to the

transfer of NiTi donor film without melting the donor film. Fig. 3.3 (a) shows the temperature profile generated in the sacrificial layer and heat transfer to donor thin film. Moreover, the temperature profile reflects the gaussian beam profile in the material at optimum laser fluence. The heat transfer is more than the spot diameter due to the conduction of heat within the material. However, the temperature is slightly overestimated because of following reasons:

- The constant value of physical properties of the PDMS sacrificial layer
- The absorption coefficient is calculated based on the penetration depth in vacuum and air conditions.
- The element deletion is not occurring due to vaporization of sacrificial layer. Hence the temperature keeps on increasing even after the degradation temperature.

3.1.2 Influence of laser fluence and PDMS thickness

During laser heating, the temperature of the sacrificial layer rapidly rises, giving less time for heat to diffuse at the NiTi thin film interface. As a result, the temperature difference between the top and bottom of sacrificial layer is exceptionally high, resulting in sacrificial layer evaporation without melting the PDMS. The temperature-induced at the top surface of the sacrificial layer is depicted in Fig. 3.3 (b) plots. At a fluence of 600 mJ/cm^2 , the highest temperature obtained at the top of the sacrificial layer is $3300 \text{ }^\circ\text{C}$, whereas it is $6250 \text{ }^\circ\text{C}$ at a fluence of 1000 mJ/cm^2 . Also, the pulse width of the laser light is $10 \text{ } \mu\text{s}$, but the peak temperature reaches $14 \text{ } \mu\text{s}$ due to relaxation time and heat discharge. As the temperature increases, the amount of material removed within the victim increases, resulting in increased pressure across the thin film, resulting in increased pixel transfer at higher fluences. As the impact increases, the generated temperature rises and reaches near the melting point of NiTi at a fluence of 1000 mJ/cm^2 .

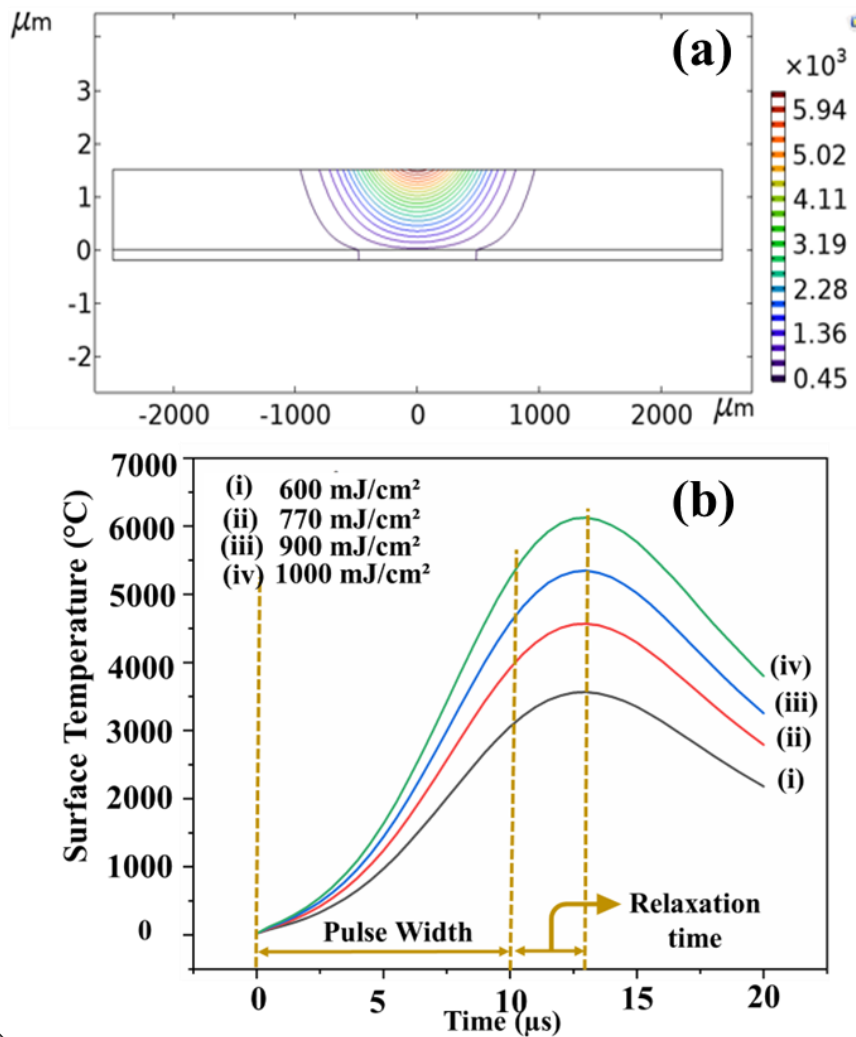


Fig. 3.3 Temperature variation by 10 μs pulse width laser irradiation (a) Gaussian temperature profile is followed at 1000 mJ/cm^2 , (b) temperature at the top of sacrificial layer with 1.5 μm thickness.

Moreover, the interface temperature does not cross the melting point of NiTi film hence the less diffusibility of CO_2 laser in the PMDS layer the material is going to transfer in a solid state only. The minimum interface temperature achieved is 627 $^\circ\text{C}$ at 600 mJ/cm^2 and the maximum temperature is 1059 $^\circ\text{C}$ at 1000 mJ/cm^2 . Fig 3.3 (b) and fig. 3.4 (a), it can be observed that the difference in the top surface of PDMS and the top surface of donor film is quite high due to low thermal conductivity and heat diffusion in the PMDS layer. Since the temperature is overestimated hence the actual temperature at interface is less than 627

°C at laser fluence 600 mJ/cm^2 . The 1000 mJ/cm^2 is fixed as the optimum fluence for the $1.5 \text{ }\mu\text{m}$ PDMS thickness. Fig. 3.3 (a) and (b) show the interface temperature between the sacrificial layer and donor film with $1.5 \text{ }\mu\text{m}$ and $3 \text{ }\mu\text{m}$ PDMS layer thickness. At a laser fluence of 3600 mJ/cm^2 , the highest interfacial temperature is less than $700 \text{ }^\circ\text{C}$. This is owing to PDMS's lower heat conductivity and higher thickness.

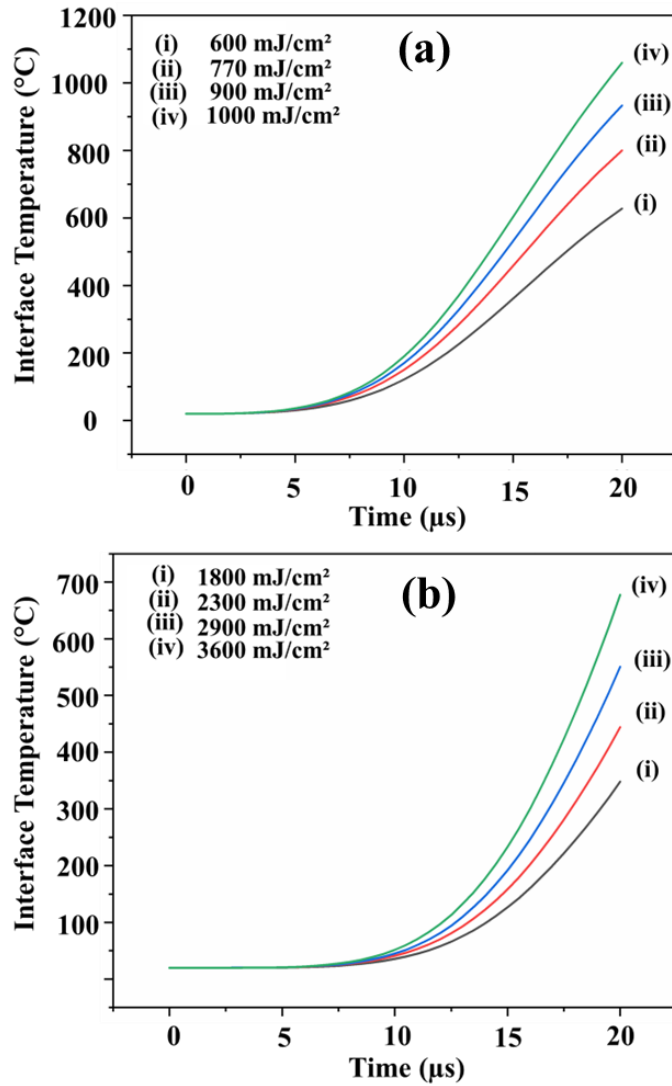


Fig. 3.4 Interface temperature at different laser fluence with a PDMS thickness (a) $1.5 \text{ }\mu\text{m}$, and (b) $3 \text{ }\mu\text{m}$

During the transfer mechanism, the particle velocity is the function of laser energy applied to the donor substrate, internal energy absorbed, and kinetic energy of the solid pixels. The energy dissipation and the bonding energy are neglected because of the vaporization of the

sacrificial layer. Hence the total energy E_t is concurrent to the internal energy E_i , causing sacrificial layer vaporization and kinetic energy E_k , providing the particle velocity from the donor to the acceptor substrate.[76]

$$E_t = E_{in} + E_d + E_k \quad (5)$$

The total energy absorbed per pulse can be calculated with the laser fluence (F) and the spot area (a). The Internal energy (E_i) is the amount of energy used for the evaporation of the sacrificial layer with the phase transformation from solid to vapour for the temperature.

$$E_t = a \times F \quad (6)$$

$$E_{in} = \rho_s \times h_s \times a [C(T_{max} - T_0)] + h_c \times (T_{max} - 273) + \varepsilon \times \sigma \times (T_{max}^4 - 273^4) \quad (7)$$

Where ρ_s , h_s , C , h_c , and ε , are sacrificial layer density, thickness, and modified specific heat capacity, convection coefficient and emissivity respectively. The modified specific heat considered the specific heat at room temperature. The initial temperature was set at room temperature (25 °C). E_d is the degradation energy for the ablation of solid to gaseous state. The extra energy available after the laser irradiation is induced by the kinetic energy of the pixels from the donor substrate that can be estimated by the

$$E_k = 1/2 \times m_d \times V^2 \quad (8)$$

$$m = \rho_d \times h_d \times a \quad (9)$$

where ρ_d , and h_d are the density and thickness of the donor film respectively. According to the laser energy conversion equation (5)- (9) temperature, and pixel velocity are two unknown variables.[76] The temperature of the pixels is estimated through numerical simulation. At the same time, the speed is calculated from the energy conservation law as the same is analysed using the time-resolved imaging of the transferred particles during the experiments.

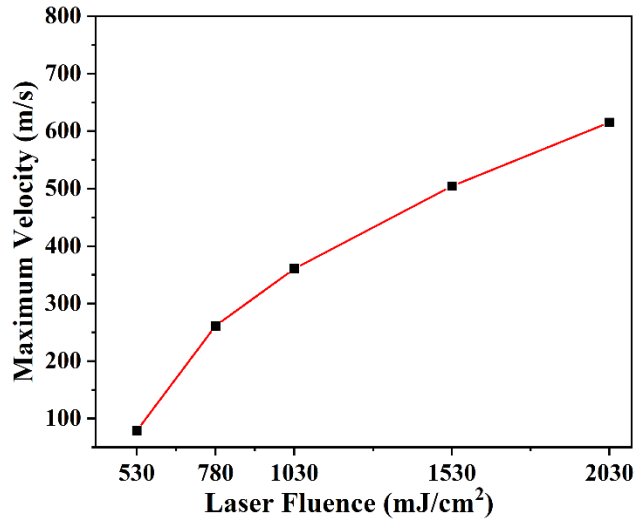


Fig. 3.5 The velocity of the pixels estimated by numerical simulation.

The velocity was calculated from the extra available energy after a reduction of 530 mJ/cm². The extra available energy is calculated using equation 1 by energy conservation, equal to kinetic energy. Hence the velocity of the pixels is evaluated by equation 8, as shown in fig. 3.5. It is observed that the pixel velocity is less than 80 m/s at 530 mJ/cm² while 504 m/s at 1530 mJ/cm². However, with an increase in fluence from 530 to 1030 mJ/cm², the pixel velocity is more compared to 1030 to 1530 mJ/cm² because velocity is the function of the square root of available laser energy at the interface. The estimated velocity is calculated based on the maximum temperature induced at the interface, which will be observed after the pixel's ejection from the donor substrate.

3.2 Summary

A FEM-based numerical simulation was performed on COMSOL Multiphysics software to investigate the influence of laser fluence on the temperature induced at the interface of sacrificial layer and donor thin film.

In case of 1.5 μm sacrificial layer thickness, the laser fluence 600, 770, 900, and 1000 mJ/cm² were varied and estimate the temperature at interface. The maximum temperature reached at 1000 mJ/cm² is 1150 °C which is less than the melting point of donor film. The minimum

temperature is more than the degradation temperature of the PDMS sacrificial layer shows the complete ablation of sacrificial layer thickness. With an increase in sacrificial layer thickness to 3 μm , the maximum temperature 750 $^{\circ}\text{C}$ at laser fluence 3600 mJ/cm^2 while the minimum temperature is 350 $^{\circ}\text{C}$ at laser fluence 1800 mJ/cm^2 . It is worth noticing that the increase in sacrificial thickness yields to increase in threshold laser fluence for the uniform transfer of line track.

The velocity of the pixels was estimated by the energy conservation principles. The excess energy beyond the threshold energy will lead to the velocity of the ejected pixels. Since the temperature was more than the degradation temperature of the PDMS sacrificial layer at 500 mJ/cm^2 hence, 530 mJ/cm^2 was used for the velocity estimation. The estimated velocity shows that the velocity is the function of the square root of the laser fluences. The maximum temperature was 1020 $^{\circ}\text{C}$ at laser fluence 530 mJ/cm^2 at the interface of the ZnO thin film and the sacrificial layer. The maximum velocity was estimated through energy conservation from the left energy after the required temperature is achieved. The maximum velocity at laser fluence 530, 1030, and 1530 mJ/cm^2 were 80, 360, and 504 m/s , respectively.

Chapter 4

Experimental Setup Specifications

Fig. 4.1 shows the schematic diagram of components of laser μ -3D printing setup for the continuous printing of pixels. A pulsed CO₂ laser is interfaced with two motion stages i.e. donor stage and acceptor stage with a minimum resolution of 10 μ m. The printing is performed by slicing the CAD drawing into multiple layers and converting it into G & M code. Based on the layer-wise G and M code the system sends the command to the laser and motion controller at the same time. The pulse delay generator delays the time between the stage movement and the pulse irradiation between two consecutive pulses. Once the first pixel is transferred the donor stage moves with the 1.5 times the spot diameter while the acceptor's stage follows the G and M code of the specific CAD drawing. As per the CAD model, the pulse generator sends the signal to the laser and motion stages. The laser beam irradiates the donor film as per the signal received and the motion stage follows the same signal with some pulse delay. As the first pixel is printed on the acceptor substrate, the second pulse will irradiate the donor film for the next pixel transfer and continues till the entire geometry is printed.

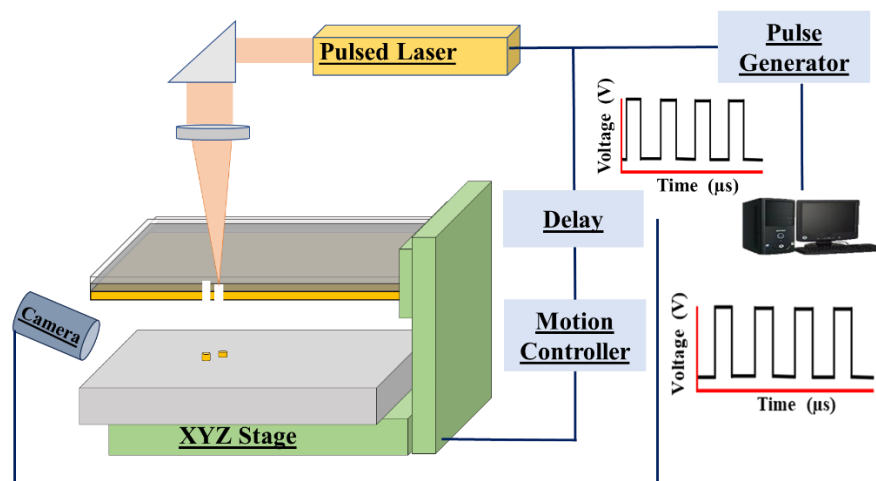
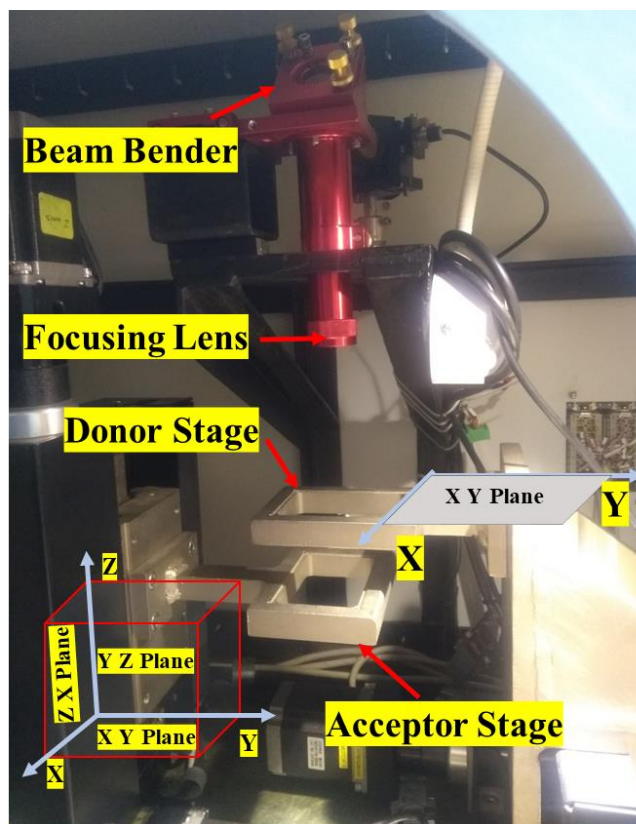


Fig 4.1 Illustrate the system design component for Laser μ -3D printing.

Fig. 4.2 shows the developed laser μ -3D printing setup with CO₂ laser and continuous control of the donor and acceptor stage. The donor stage

has 2 degrees of freedom in X and Y directions while the acceptor stage has 3 degrees of freedom in X, Y, and Z for three-dimension printing. The total build volume of the system is $80 \times 80 \times 80 \text{ mm}^3$. The laser spot is focused using different focusing lenses for variable spot sizes on the donor substrate. A substrate heater is also installed at the acceptor stage with a heating capacity of up to 300°C to heat the acceptor during the printing process. The developed setup is controlled with user interface software. The software supports the G & M code of the CAD model and then generates the signal as per the CAD geometry. The continuous line can be printed by a certain pulse overlap of pixels printed on the acceptor substrate. The system is integrated with a carbon dioxide laser working at $10.6 \mu\text{m}$ laser wavelength. Most of the electronics, optoelectronics, and photonics devices are fabricated on the silicon wafer due to its semiconductor nature, high-temperature resistance, and is chemically stable. It is also having good transmissivity with CO_2 laser in the mid-infrared region at $10.6 \mu\text{m}$ wavelength.



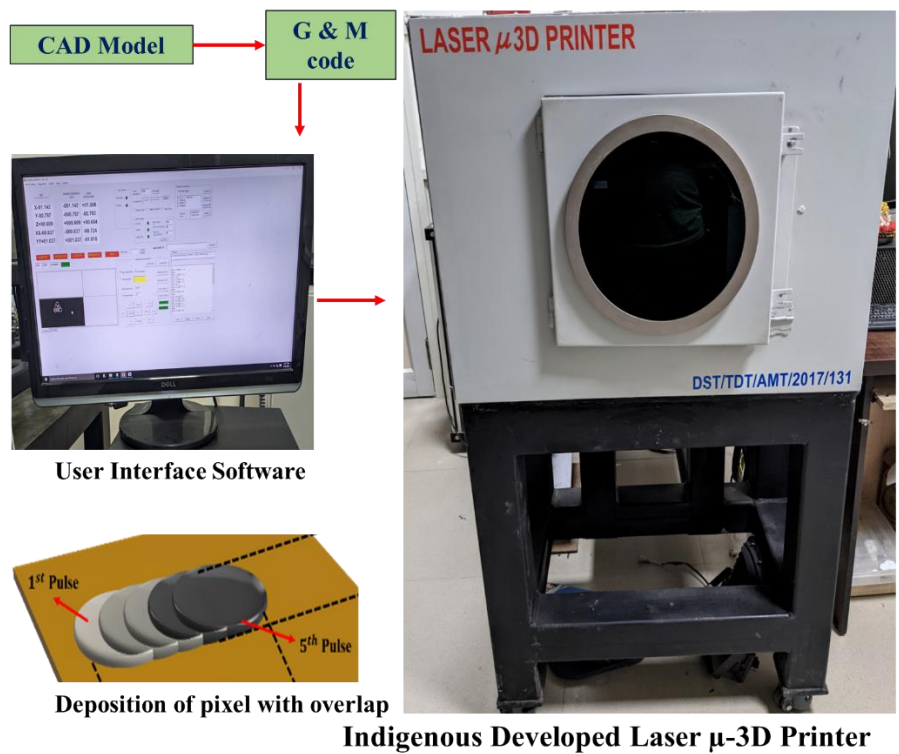


Fig. 4.2 (a) The experimental setup with degree of freedom of donor and acceptor stages and **(b)** Experimental setup of Laser μ-3D printing and strategy for line printing with pulse overlap.

4.1 Donor Preparation

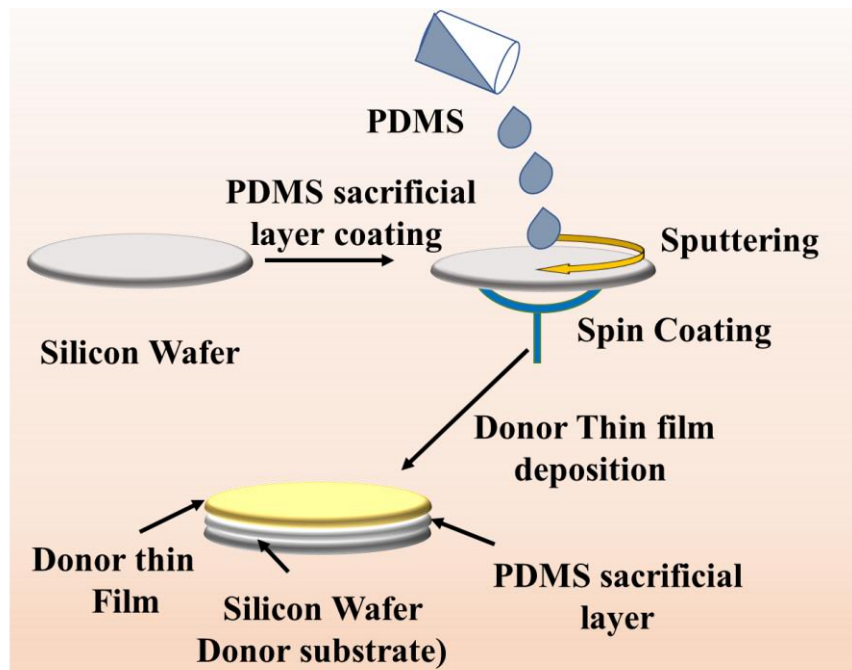


Fig. 4.3 Preparation of donor with sacrificial layer coating and thin film deposition

The transmissivity of the donor substrate should be higher to pass the laser energy through the material. In the case of 10.6 μm laser wavelength, a silicon wafer is having an 80 % transmissivity, hence it is used as donor substrate in this study. Initially, the silicon wafer is dipped in acetone and then rinsing it with deionized water to remove any imperfections or contaminants.

4.1.1 Sacrificial Layer coating

The sacrificial layer absorbs the laser energy and vaporises for the thrust mechanism hence the absorptivity of the sacrificial layer should be good. hence it is used as a sacrificial layer coating in between the donor substrate and donor film. PDMS (Sylgard 184 kit) base (A) polymer and curing agent (B) are mixed in the weight ratio of 10:1, respectively. The mixture kept in a vacuum (0.06 MPa) for 1 min for degassing process ensuring a homogeneous and smooth coating. The mixture is spin-coated on the silicon substrate at 12000 RPM and baked at 60 $^{\circ}\text{C}$ for 90 min to curing the polymer. Fig. 4.4 (a) & (b) show the silicon wafer substrate and PDMS sacrificial layer-coated Silicon substrate respectively.

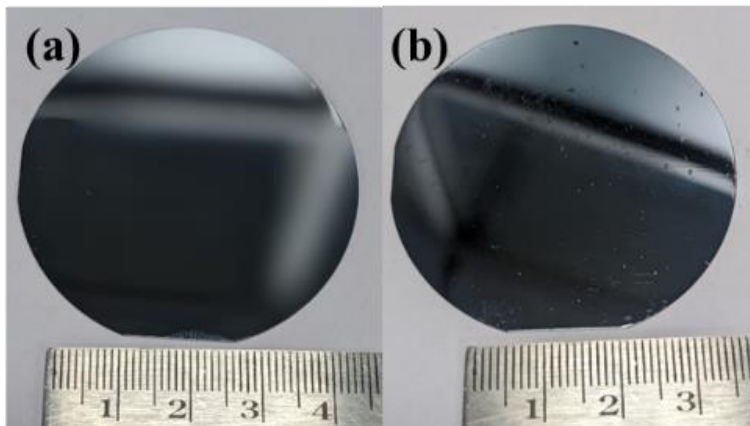


Fig. 4.4 (a) Transparent Silicon substrate at laser wavelength 10.6 μm Sacrificial layer coating on a silicon wafer

4.1.2 Donor thin film deposition

The thin film was deposited over the sacrificial layer using DC and RF sputtering technique. For electrically conductive NiTi thin film, DC

sputtering was performed while RF sputtering was used for ZnO ceramic thin film deposition. The vacuum was created using a rotary and diffusion pump to maintain about 5×10^{-5} mbar pressure inside the chamber for thin film deposition. The argon was used as inert gas and purged in the chamber at 20 l/min at 1 kg/cm² pressure inside the chamber at a working pressure 2×10^{-3} mbar. Fig. 4.5 shows the schematic and experimental setup of the sputtering process used in this study.

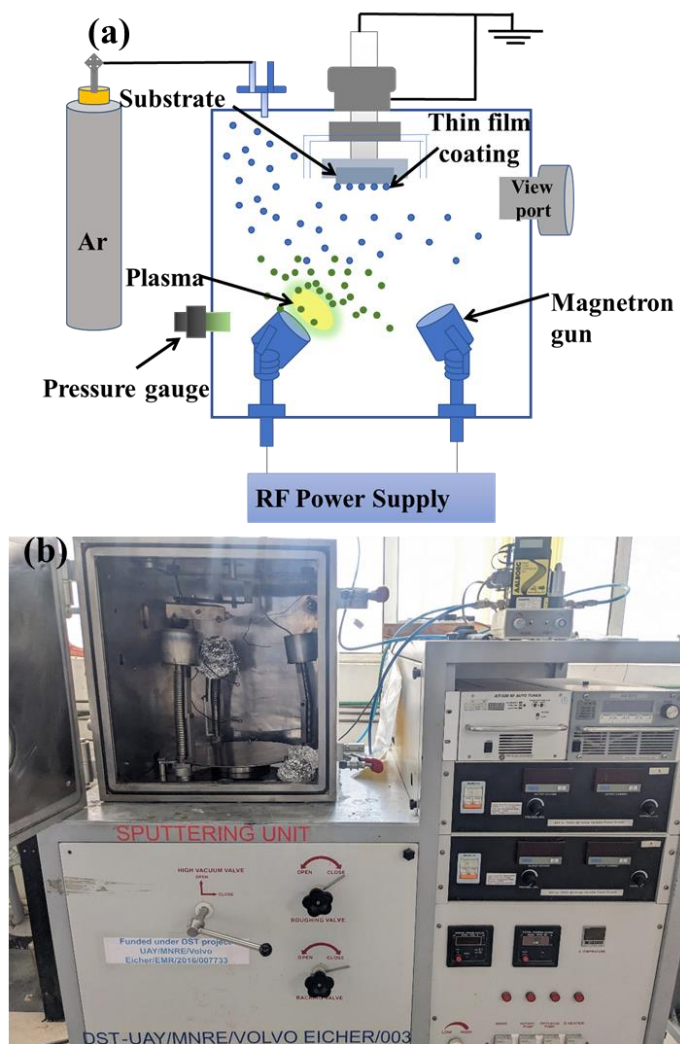


Fig. 4.5 Schematic diagram of sputtering and experimental setup with three deposition guns.

4.2 Imaging Setup

The imaging setup consists of a high-speed camera and an illumination source to track the particle coming from donor substrate. For the particle dynamics investigation, a shadowgraph was created to track the particle across time. A high-speed camera (Phantom Miro LAB310) with long distance microscopic lens (LDM) (Infinity Model K2 DistaMax) and a high-intensity white light are aligned perpendicular to the laser beam path to create the shadowgraph as shown in fig 4.6. The time resolved images of plume were post-processed and analyzed using ImageJ software.

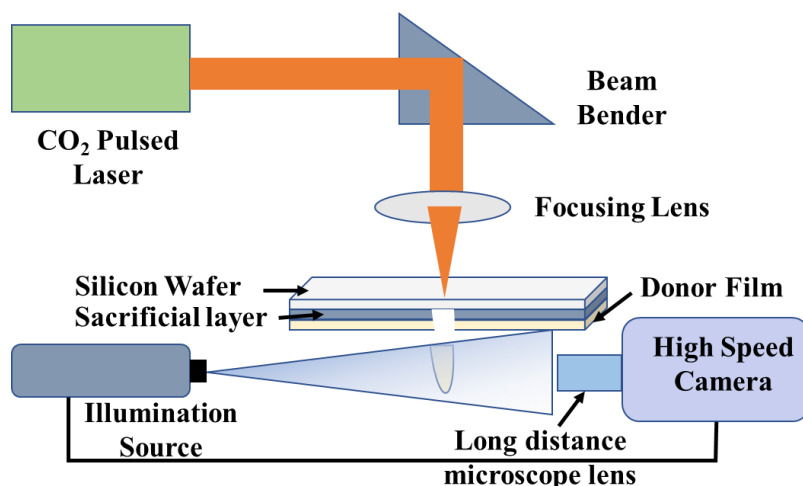


Fig. 4.6 Schematic diagram of particle dynamics experimental setup

4.3 Characterization

4.3.1 Printed Morphology and Structure

The morphology is measured using an optical microscope, scanning electron microscope and surface profilometer. The Leica microscope (Make: Leica, Model: DMS1000) with a maximum magnification of 300X is used to measure the deposited pattern. The optical surface profilometer (Profilom 3D) using the white light interference method. Scanning electron microscopy (Make: JEOL SEM, Model: JSM J7100) with Energy Dispersive Spectroscopy (EDS) for X-ray spectroscopy is used for high magnification of printed structure and elemental confirmation. The crystal structure and phase pattern were evaluated by X-ray diffraction analysis with two thetas from 30° to 70° (Rigaku Smart

Lab system). A scotch tape test was used to test the adhesion of NiTi pixels on the acceptor substrate. The weight of the tape was measured before sticking it over the printed structure. It was ensured that there are no air bubbles between the tape and the printed structure. After a few moments, the tape was pulled on the universal testing machine and weighed the scotch tape again. The difference in the initial and final weight of the tape gave the weight of the thin film that adhered to the tape and was used as a scale to compare the adhesion of the thin film.

4.3.2 The functionality of printed structures

Resistance measurement: The strain gauge is connected with copper wire with Agilent digital multi-meter (DMM) for measuring resistance using the two-wire resistance method during tensile loading at various strain rates.

Photoluminescence Spectroscopy: To quantify photoluminescence (PL) emission at room temperature, A photoluminescence (PL) spectrometer (Dongwoo Optron DM 500i) with a continuous wave He-Cd laser excitation source (excitation wavelength: 355 nm, PMT detector) was used.

Tribo-performance: A in-house build tapping machine is used for contact and separation of two surfaces for turbo-performance with tapping frequency 0-300 Hz. The linear movement is controlled by adjusting the stage in the z-direction. The output of the tribo device is measured in terms of open circuit voltage and short circuit current. The OCV is measured using an oscilloscope (Make & Model: Tektronix MDO32) while the SCC is measured using the electrometer (Make & Model: Kethley 6514).

4.4 Methodology

The donor substrate is prepared with sacrificial layer coating and thin film depositions. The PDMS sacrificial layer is coated with 1.5 μm and 3 μm thickness on the silicon wafer and the NiTi thin film is coated with 200 nm thickness over the PDMS by sputtering. Once the coating is prepared the laser micro-3D printing is deployed for the printing process.

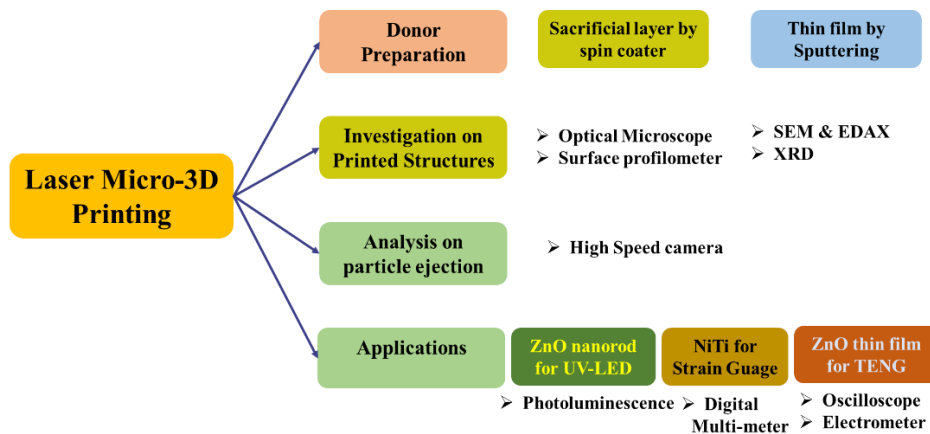


Fig. 4.7 Flowchart of the work

Chapter 5

Parametric investigation of NiTi shape memory alloy through μ -3D printing

Nitinol is a nickel-titanium alloy with shape memory effect and superelasticity behaviour. It "remember" its previous shape and return to it under specific conditions. This shape memory phenomenon is caused by a reversible phase shift inside the material. Nitinol may deform while in one phase and restore to its original shape by switching to another phase when heated. Superelasticity, on the other hand, refers to Nitinol's capacity to regain its original shape after severe deformation with external load. It can withstand huge stresses (up to 8%) and yet return to its original shape as the external force is removed.[77] The unique properties of NiTi make it suitable for the microactuators for MEMS devices, aerospace components, and medical devices (such as stents, orthodontic wires, and surgical instruments).[78][79]

In this chapter, Parametric investigation is performed to investigate the effect of different process parameter on the printing of NiTi pixels in line track and multilayer deposition. The Laser μ -3D printing is deployed for printing in solid phase NiTi using PDMS as sacrificial layer. The process parameters such as laser fluence, sacrificial layer thickness, spot overlap, substrate heating are varied and studied the influence on the uniformity, and adhesion on the acceptor substrate after deposition.

5.1 Influence of laser fluence and PDMS thickness

The optical micrographs in fig. 5.1 shows the influence of laser fluence on the geometrical characteristic of NiTi pixels printed on silicon acceptor substrate at 1.5 μm PDMS thickness. The NiTi pixels printed by micro 3D printing are shown by golden colour track while the acceptor substrate material is shown by dark colour. Uniformity of printed line is defined as a track with no interspacing gaps between two consecutive pixels on the acceptors substrate. At 600 mJ/cm^2 laser

fluence, small NiTi pixels are printed in the form of debris that yields to non-uniform deposition of pixels in fig 5.1. Due to insufficient pressure generated during laser absorption in the sacrificial layer, a discontinuous deposition is observed at a laser fluence of 600 mJ/cm^2 . This might be due to the adhesion force dominating the thrust force generated by the pressure-induced in the sacrificial layer. With a further increase in laser fluence to 770 mJ/cm^2 , homogeneous pixels are deposited at this fluence. The pixel density improves when the energy density of the laser beam increases from 900 mJ/cm^2 to 1000 mJ/cm^2 . As a result, the threshold fluence required for uniform transmission of NiTi pixels is 770 mJ/cm^2 . The surplus quantity of laser energy causes the pixels to travel faster due to higher laser fluence.[80] The higher the pixel velocity, the better the adhesion to the receiver substrate owing to plastic deformation during pixel landing.

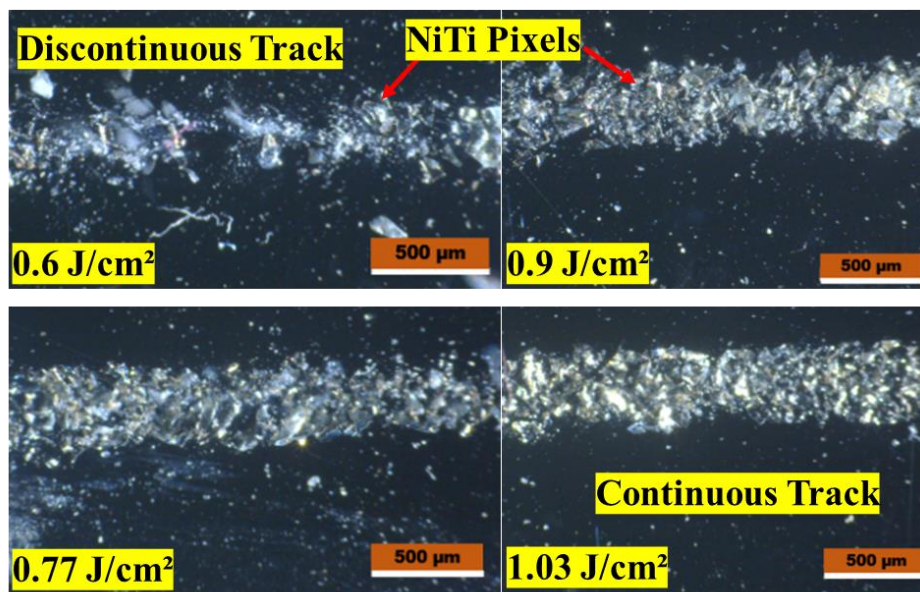


Fig. 5.1 Transferred pixel on the receiver substrate at laser fluences (a) 600 mJ/cm^2 , (b) 770 mJ/cm^2 , (c) 900 mJ/cm^2 , and (d) 1030 mJ/cm^2

The transfer mechanism begins to function following the start of sacrificial layer ablation, which causes a rise in pressure beneath the thin donor film. The volume of sacrificial layer ablation determines the pressure generated. As a result, the thickness of the sacrificial layer is a

critical component in developing sufficient laser fluence for uniform pixel transfer.

The optical micrographs of the NiTi pixels deposited at 3 μm sacrificial thickness are shown in Fig. 5.2. A small quantity of PDMS (white) is also transmitted to the receiver substrate at lower fluence levels between 1800 and 2300 mJ/cm^2 . This might be owing to an overabundance of PDMS on the donor substrate. After energy absorption, the surplus quantities of transparent PDMS expand owing to fast heating and begin dissociation in the form of residues. With higher laser fluences, a clean transfer occurs with no residues. This might be because there is enough laser energy available to vaporise surplus PDMS and provide a clean transfer of NiTi pixels. Furthermore, the deposited NiTi linear track exhibits non-uniform deposition across its width. Fig. 5.2 depicts transfer NiTi pixels deposition without residues at laser fluences of 2900 and 3600 mJ/cm^2 with a strong connection between each pixel, resulting in uniform deposition.

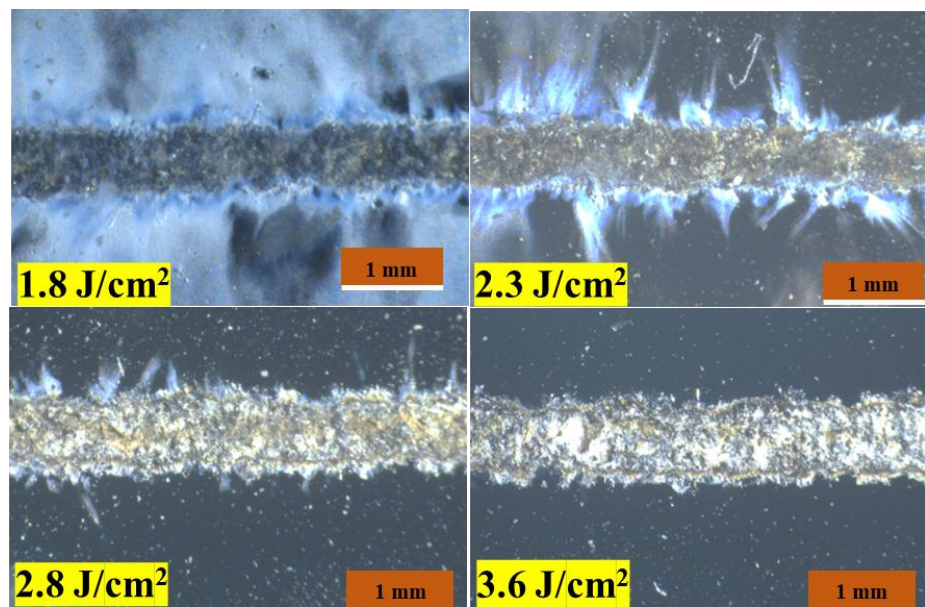


Fig. 5.2 Printed NiTi solid pixels at (a) 1800 mJ/cm^2 , (b) 2300 mJ/cm^2 , (c) 2900 mJ/cm^2 , and (d) 3600 mJ/cm^2 laser fluences.

The minimal size of feature in microdevices is one of the essential elements for device performance, hence the average width of printed

tracks are measured with PDMS thickness of 1.5 μm and 3 μm in fig. 5.3. Three separate points throughout the length at varied laser fluences are used to measure the track width. Due to an increase in the laser beam's divergence at high energy, the track width is increasing with laser fluence. As a result, the laser beam's spot size grows with fluence, resulting in a wider track. The average track width at threshold fluence is $340 \pm 20 \mu\text{m}$ with 1.5 μm PDMS thickness, whereas the track width is $680 \pm 20 \mu\text{m}$ with 3 μm PDMS thickness, as shown in Fig. 5.3 (a) and (b).

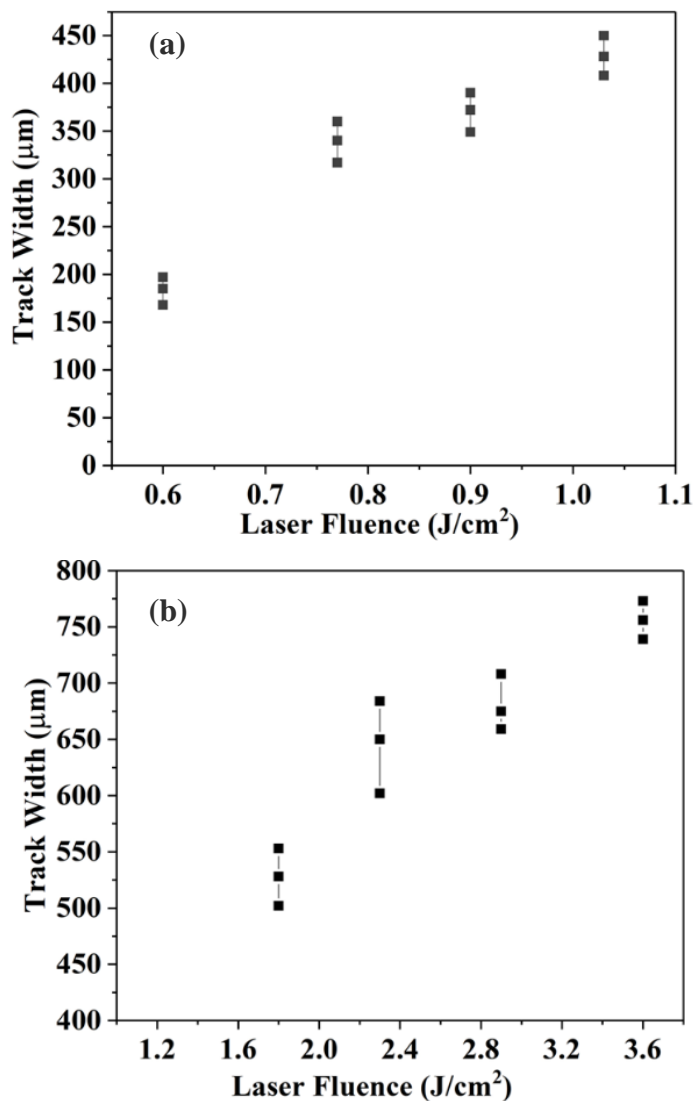
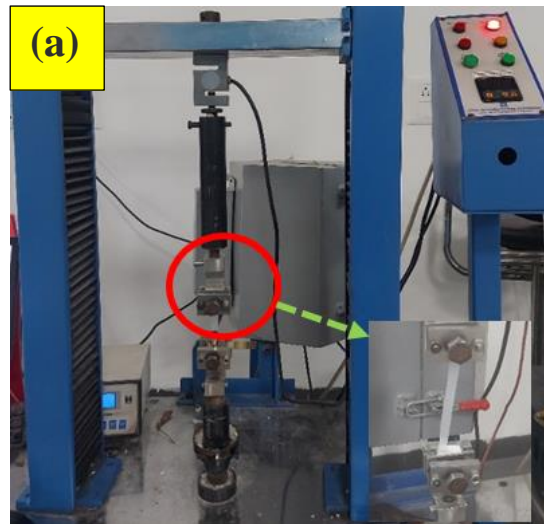


Fig. 5.3. Width of line track at various laser fluences with PDMS thickness (a) 1.5 μm and (b) 3 μm .

5.2 Effect of substrate heating

Because of the substrate condition and high pixel velocity, the transferred pixel adheres to the substrate. The pixel velocity is regulated by laser fluence, while the substrate condition takes roughness and temperature into account. During the landing, the faster the velocity of the pixels, the more tension and plastic deformation. While the substrate condition enhances the wettability of pixels on the receiver substrate, the substrate temperature is adjusted to test the effect on transmitted pixel adhesion. As illustrated in fig. 5.4, the NiTi solid pixels are deposited in pixel by pixel approach in rectangular geometry on the silicon substrate at preheat temperatures of 25 °C, 100 °C, and 200 °C at 2300 mJ/cm² laser fluence.



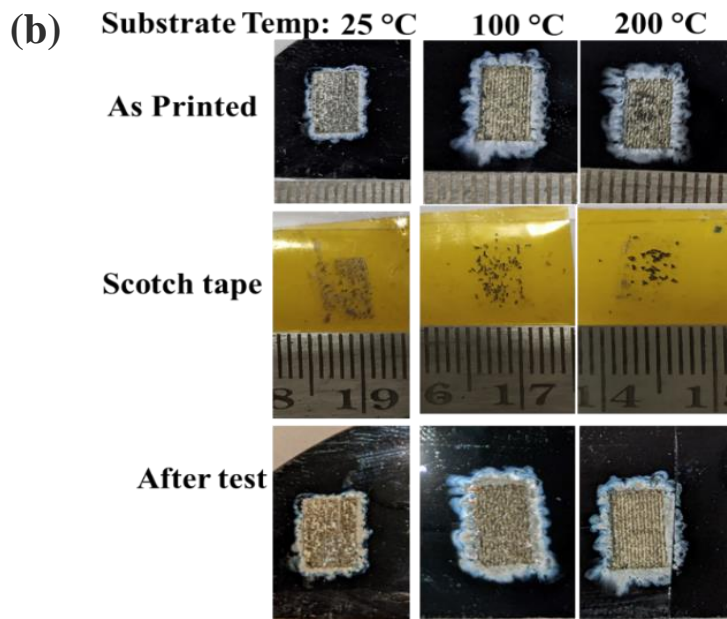


Fig. 5.4. (a) Scotch tape test on UTM and (b) NiTi printed structure at 2300 mJ/cm² laser fluence with 3 μm sacrificial layer & 25°C, 100 °C, and 200 °C substrate temperature.

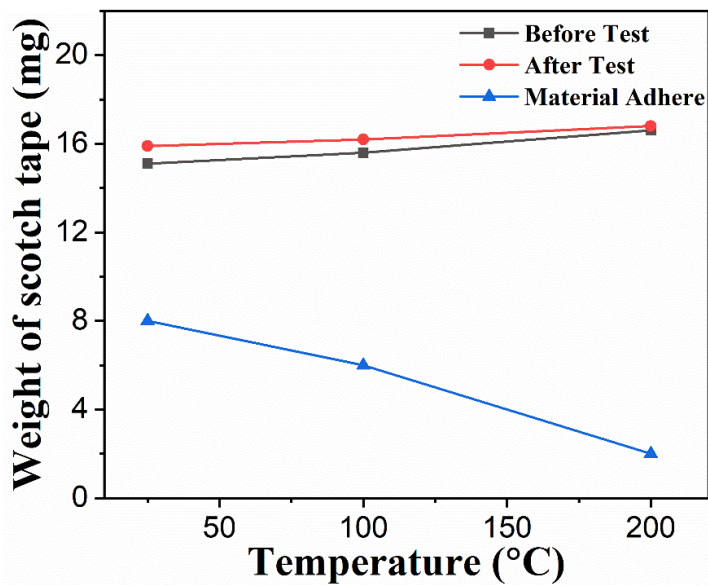


Fig. 5.5 Weight of Scotch tape before and after the test

To investigate the adhesion of the printed structure, scotch tape test is performed. The tape was stuck to the printed structure and pulled by tensile test on UTM as shown in fig. 5.4 (a). The weight of the scotch tape is measured before and after the test. The quantity of material that adheres to the tape after the test is determined by the difference in the

weight of the scotch tape. Figure 5.5 depicts the weight of the tape before and after the substrate temperature test. Because of the substance adhering to the tape, the weight of the tape increases a little after the test. Furthermore, when the substrate temperature rises, the material adherence to the tape reduces, resulting in improved adhesion with the silicon substrate.[81] This might be owing to an increase in substrate surface energy caused by the adhesive force between the pixels and silicon substrates. Furthermore, a high-temperature difference between the pixel and the substrate at lower substrate temperatures causes increased thermal stress in the deposited pixel, which causes pixels to compress after landing on the substrate.[82]

5.3 Effect of spot overlap

The precise location of each pixel adjacent to each other is required for continuous pattern deposition utilising single pixels, and it is maintained by the speed of donor and acceptor substrates, as well as the frequency of the laser beam. [83] To generate the continuous line pattern, both substrates are moving at the same speed at varying overlap percentages. For 30, 60, and 90 % spot overlap, substrate speeds are 60, 240, and 420 mm/min, respectively. The fluence is set at 900 mJ/cm² for the ejection mechanism, with a sacrificial layer of 1.5 μm thickness and a pulse frequency of 10 Hz. Fig. 5.6 depicts the line track at 30, 60, and 90 percentage beam overlap, respectively. The size of solid pixels reduces as the overlap percentage increases, while the space between two consecutive pixels reduces, which ended in a continuous track.[84][85]

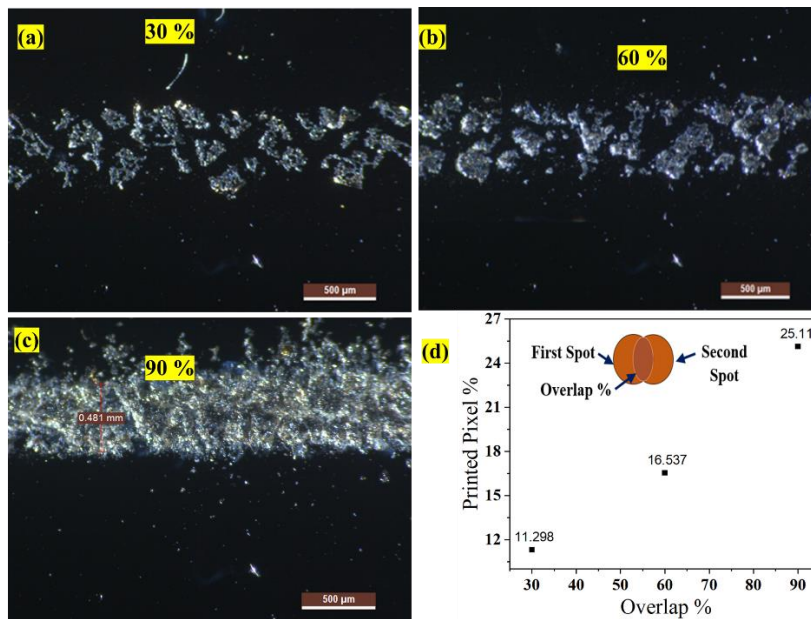


Fig. 5.6 Printed pixels in line track with beam overlap with (a) 30, (b) 60, and (c) 90 %, and (d) printed pixel % on substrate

5.4 Effect of focused and defocused condition

The focused laser beam is having small spot size compare to defocused beam due to diverging nature after the focal plane. Hence the laser intensity for the transfer mechanism will be more in focused condition. From fig. 5.7 it can observed that the focused beam transfers the material with high resolution at the edge of the line track while the defocused beam prints the NiTi pixels with spattering at the edges and broader track width. As the distance increase to 140 mm at defocused conditions, the laser intensity reduces on donor substrate and provides more divergence of the ejected particle from the donor substrate. In case of 160 mm defocused condition, the laser intensity reduces spot area in such a way that the laser intensity per unit area is not sufficient for the ejection of the material uniformly.

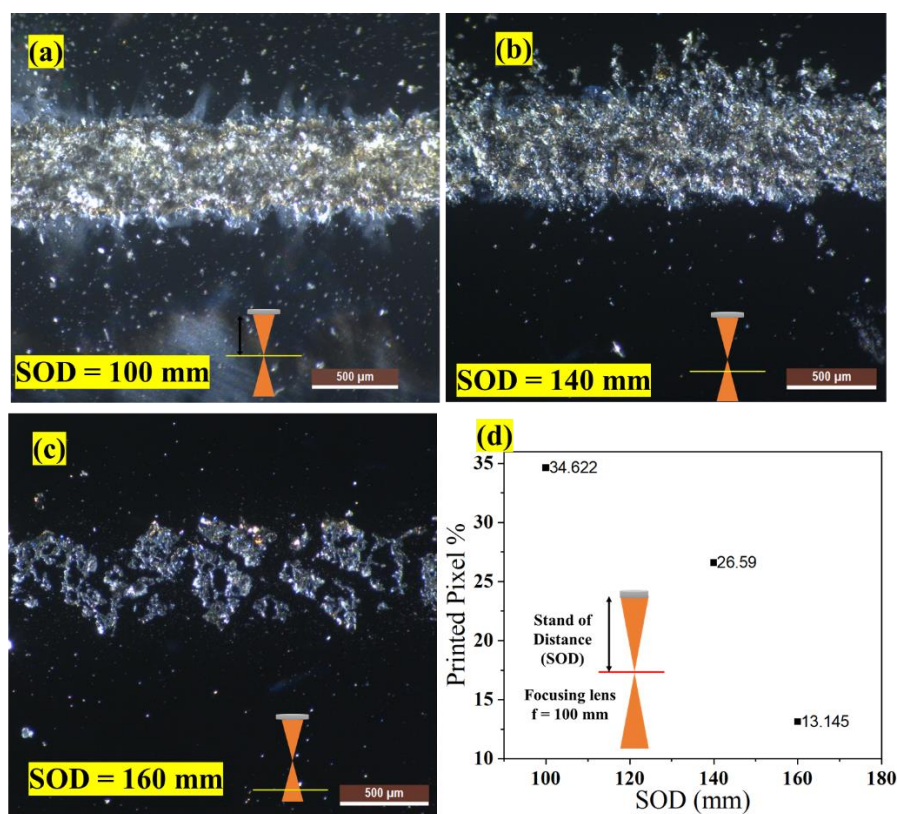


Fig. 5.7 Effect of beam condition on printed line track at laser at (a) 100, (b) 140, (c) 160 mm sod, and (d) printed pixel % on substrate

5.5 Morphology and structural characteristics.

Figure 5.8 (a) depicts the XRD pattern of a rectangular region deposited at a laser fluence of 2300 mJ/cm^2 with a thickness of $3 \mu\text{m}$ PDMS and a line overlap pattern. The deposited materials contain three Ni-rich phases of nitinol, NiTi, Ni₂Ti, and Ni₄Ti₃. The Ni₄Ti₃ 100 crystal plane is observed at $2\theta = 25.28^\circ$, and the Ni₂Ti 110 and 211 crystal planes are observed at $2\theta = 51.71^\circ$ and 51.74° , respectively. At $2\theta = 43.38^\circ$ and 58.37° , respectively, the NiTi phases martensite B19 and austenite B2 are detected. Ni, Ti, O, C, and Si are present in the transferred patterns. The oxygen concentration is due to oxidation during laser processing, whereas C, O, and Si are seen owing to PDMS sacrificial layer dissociation in Fig. 5.7 (b). Fig. 5.7 (c) shows the low and high magnification microscopic image of printed NiTi pixels in hexagonal structures.

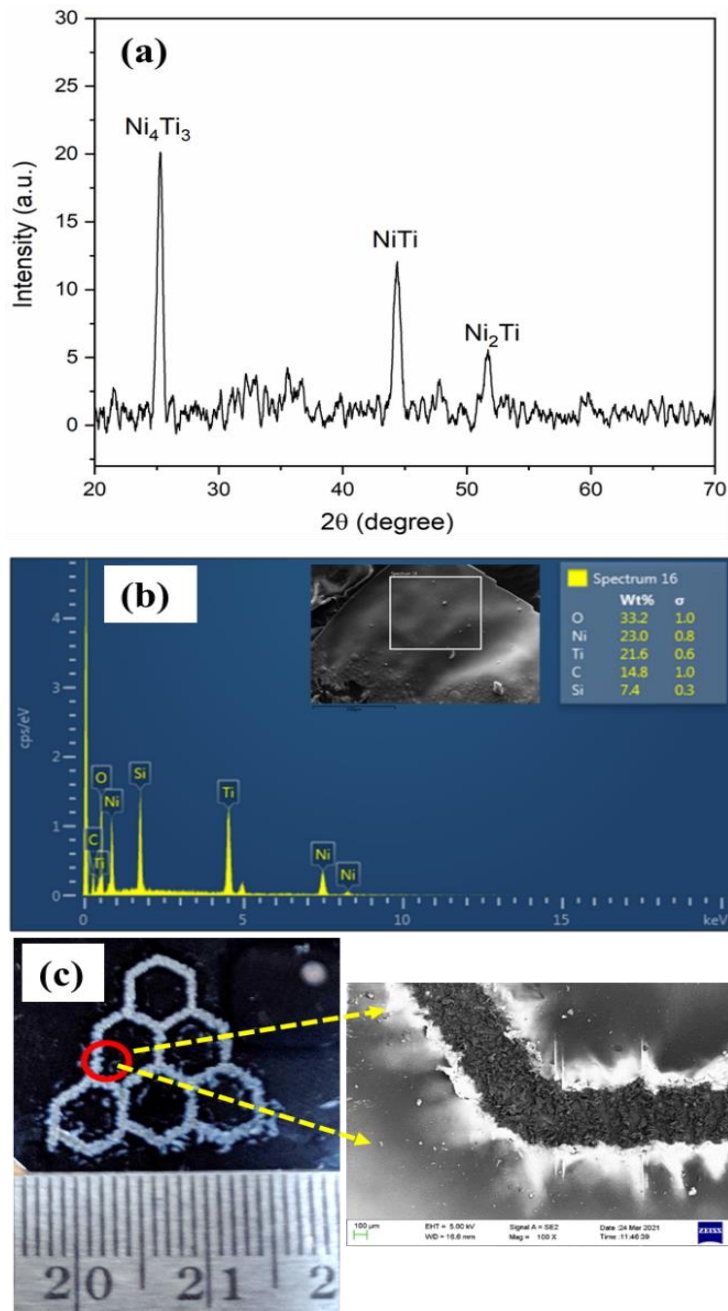


Fig. 5.8 (a) X-ray diffraction of the deposited pixel, (b) EDS elemental analysis of the deposited pixels, and (c) hexagonal pattern at laser fluence 1000 J/cm^2 with $1.5 \mu\text{m}$ PDMS thickness

5.6 Multilayer structure

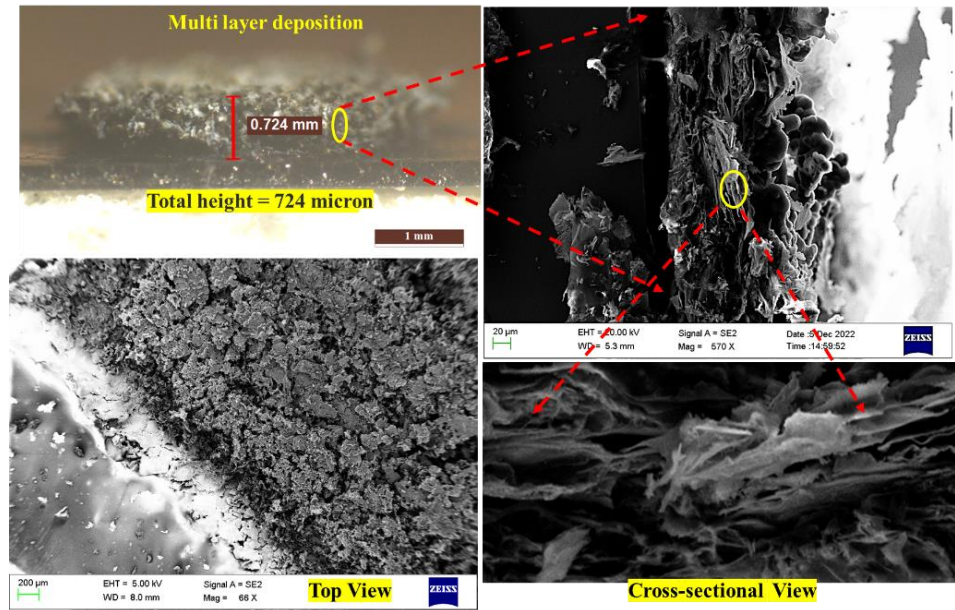


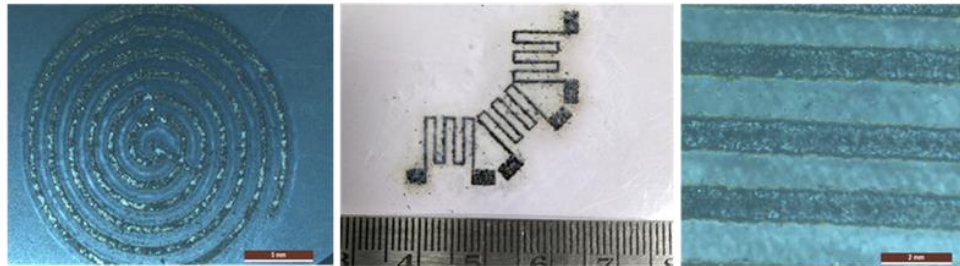
Fig. 5.9 Multilayer three-dimensional structure with top view and cross-sectional view substrate at laser fluence 1030 mJ/cm^2 .

At optimized laser fluence 1.03 mJ/cm^2 and $200 \text{ }^\circ\text{C}$, multiple layers were deployed for the printing of three-dimensional structures up to $724 \text{ }\mu\text{m}$ thickness in solid thin film form. Fig. 5.9 shows the top view and cross-sectional view of the three-dimensional structure. It can be observed that the thin film layered structure is visible in the cross-sectional view of printed structure with high roughness on the top surface. The adhesion of the next layer was due to the plastic deformation during landing of pixel over the previous layer and the substrate heating conditions.

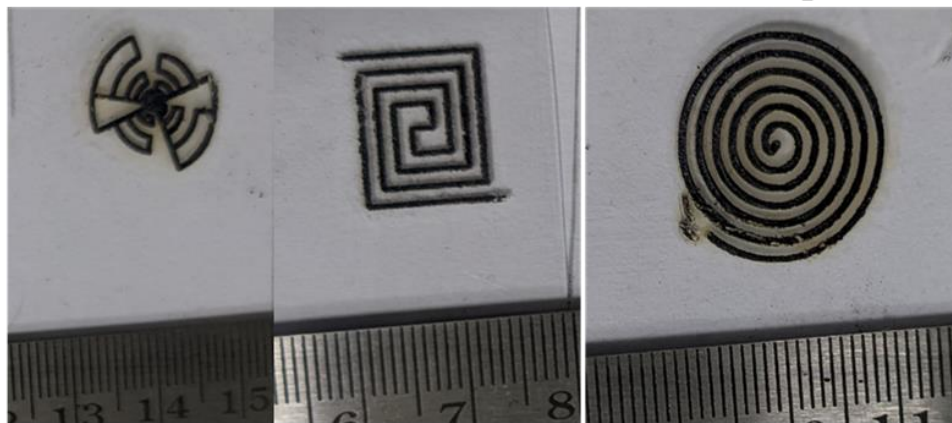
5.7 Metal printed for electronics applications

Micro patterned structures are widely employed in a variety of applications such as micro sensors, actuators, electronics circuits, and biological applications.[86–88] Figure 5.10 depicts multiple printed structure configurations on flexible PET sheets for various uses. The tiny antenna may be implanted in a circuit board to generate multiple RF frequencies for signal transmission. Similarly, depending on the designs, interdigitated structures and combinations of micro heaters can be implanted for resistive heating in specific locations. A porous structure

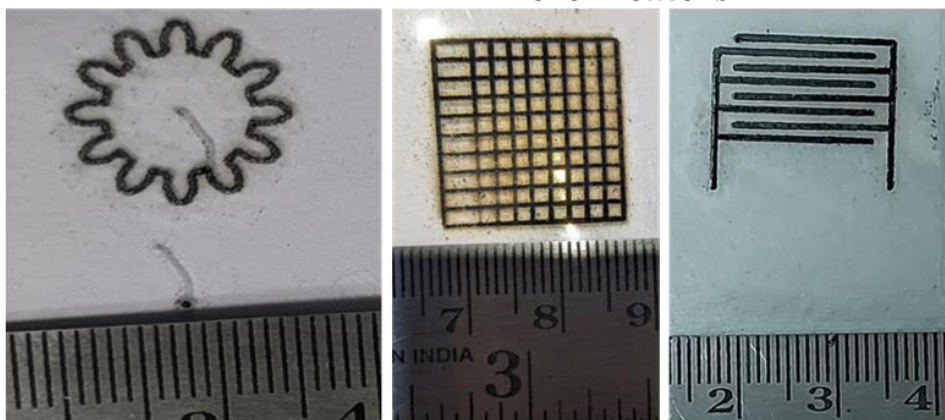
can be utilized in biomedical applications to cultivate cell cultures with varying porosity configurations. Similarly, the gradient porosity may be printed in three-dimensional structures on any substrate. The feature size may be adjusted by moving the laser precisely across the donor and acceptor substrates.



Micro Heater Rosette Strain gauge Line pattern



Micro Antenna Micro Heaters



Micro Gear for MEMS Grid Structure for cell culture Interdigitate Structure

Fig. 5.10 Laser μ -3D metal printed structure for electronics applications.

5.8 Summary

The chapter shows the printing of solid-phase NiTi pixels in a line track using a laser micro-3D printing process using a long pulsed CO₂ pulsed laser. The parametric investigation was performed to estimate the effect of different process parameters on the pixel transfer on the acceptor substrate at a distance of 50 μm. The influence of laser fluence, PDMS thickness, acceptor substrate temperature, spot overlap, and beam condition on the uniformity of printed pixels is discussed thoroughly. The study leads to the following conclusions:

- **Influence of laser fluence:** The laser fluence is the most significant parameter in this process that defines a resolution of the printed structure.
 - With numerical simulations, a process window is developed for the printing of material in such a way that the interface temperature at the donor film and sacrificial layer should be less than the melting point of the NiTi thin film.
 - The laser fluence 600, 770, 900, and 1000 mJ/cm² are varied and the maximum temperature reaches 1150 °C which is less than the melting point of donor film.
 - The minimum temperature is more than the degradation temperature of the PDMS sacrificial layer showing the complete ablation of sacrificial layer thickness.
 - The printed structure shows that with an increase in the laser fluence, the continuous printing of pixel was achieved at 1.03 mJ/cm².
 - Higher laser fluence results in wider track width due to expansion of vaporized sacrificial layer during the transfer process. Due to the increasing diverging nature of the laser beam at higher fluences, the track width of the deposited line pattern rises from 330 μm to 450 μm when the laser fluence increases from 600 mJ/cm² to 1030 mJ/cm².

- **Influence of sacrificial layer thickness:** Higher sacrificial layer thickness (i.e. 3 μm) increases the threshold limit of the laser fluence for uniform printing of the material. Moreover, the track width was also increased to 570 to 770 μm , with laser fluence from 1800 mJ/cm^2 to 3600 mJ/cm^2 .

The numerical simulation predicted the temperature generated is less than the degradation temperature of the PDMS at 1800 mJ/cm^2 . The maximum temperature was 750 $^{\circ}\text{C}$ at laser fluence 3600 mJ/cm^2 while the minimum temperature is 350 $^{\circ}\text{C}$ at laser fluence 1800 mJ/cm^2 . This might be due to less absorption length of CO_2 laser in PDMS sacrificial layer.

- **Influence of substrate heating:** The material ejected from the donor substrate and deposited on acceptor substrate with high velocity. The pixel goes to plastic deformation which leads to the adhesion of the pixel on the acceptor substrates. Moreover, to increase the adhesion of the pixel, the acceptor substrates were heated to 100 $^{\circ}\text{C}$ and 200 $^{\circ}\text{C}$ and printing was performed. The scotch tape test shows that the adhesion of the material increases with an increase in substrate temperature due to an increase in surface energy at elevated temperature.

- **Influence of spot overlap:** The continuity of the printed structures is greatly influenced by the subsequent pixel position. To achieve the effective transfer at 1030 mJ/cm^2 , three distinct spot overlaps (30, 60, and 90%) are employed. When the spot overlap was 30%, all of the particles were unable to connect, but when it was 60%, the distance between the pixels reduced. However, a continuous line was produced at the same laser fluence in 90% of the spot overlap areas.

- In the case of beam condition at the donor substrate, three different conditions were varied, focused condition (100 mm), defocused beam (140 mm) and defocused beam (160 mm). The focused beam prints the material with a sharp edge while the defocused beam at 140 mm shows printing with spattering at the edges. However, the 160

mm defocused beam shows insufficient pressure force for uniform transfer of the pixels.

- With pixel-by-pixel and layer-by-layer approach, a three-dimensional multi-layer structure was printed up to 724-micron thickness with a layer thickness of 0.5 μm . The printed structure shows the thin layered films in the cross-sectional view of the printed structures. At last, different pattern-based microelectronics devices were printed to show the capability of the process for MEMS applications.

Chapter 6

Particle dynamics Study using long Pulse in Laser μ -3D Printing

This chapter focuses on the investigation of plume size and correlation between the printed features on the acceptor substrate. The particle gets transfer from the donor substrate to the acceptor substrate with a specific velocity which is governed by the amount of energy absorb by the sacrificial layer. This leads to the formation of high-pressure gas between the donor film and the donor substrate. Due to short pulse width, the intensity of energy is so high that melts the donor film.

Fig. 6.1 shows the heat diffusion in the sacrificial layer and the ZnO film is observed with a time frame after the laser irradiation at laser fluence 1530 mJ/cm^2 . The ablation of a sacrificial layer and the temperature profile reflects the amount of pressure-induced over the thin ZnO film that leads to ejection velocity of the ZnO particle from the donor substrate. It is also observed from fig. 6.1 (b)-(d) the heat starts diffusing to the ZnO thin film from the sacrificial layer after $5 \mu\text{s}$ to $25 \mu\text{s}$. The temperature increase leads to vaporizing of the entire PDMS after $20 \mu\text{s}$ of irradiation. The temperature rise in the material is estimated using the internal energy absorbed in the sacrificial layer. Fig. 6.2 (d) illustrates the surface temperature of the PDMS sacrificial layer at three different laser fluences.

It can be observed that at all three laser fluences, the temperature is beyond the vaporization temperature of the PDMS, which induced the kinetic energy of the ZnO solid pixels. However, the laser pulse width is $10 \mu\text{s}$, but the maximum temperature is nearly $24 \mu\text{s}$. This might be due to the relaxation time of the energy absorbed in the materials. Once the temperature is achieved at maximum value, it starts decreasing due to the heat loss by convection and radiation.

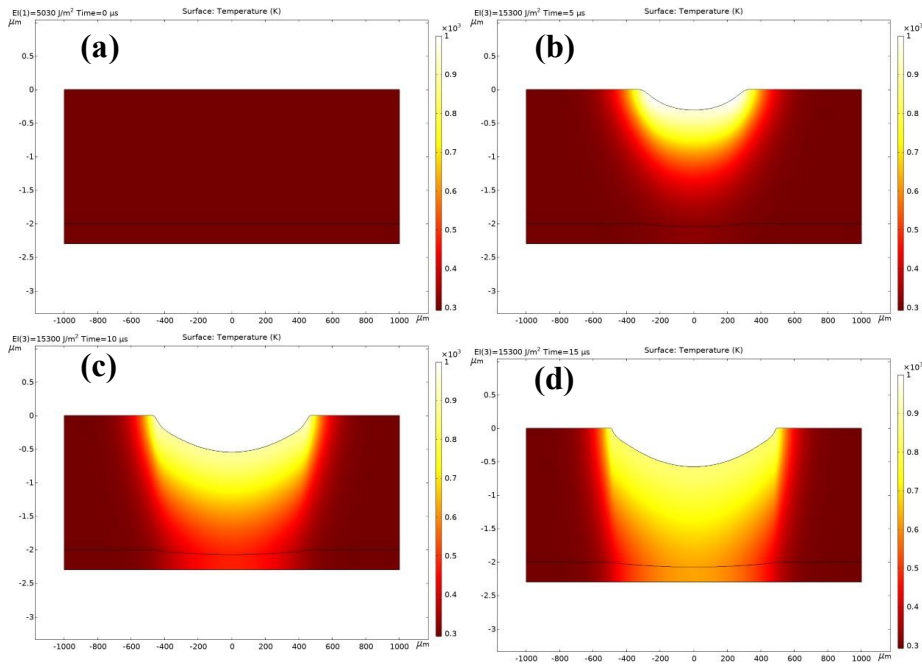


Fig. 6.1 The ablation of a sacrificial layer at laser fluence 1530 mJ/cm² with time frame after laser irradiation

The profile's slope shows the temperature rise rate in the material. The rate of the temperature rise at high fluence is higher than at low fluence. This might be due to the higher temperature gradient at higher fluence; hence the heat dissipation in the material is faster as compared to the lower fluence. Fig 6.2 (a)-(c) shows the ablation depth and temperature induced by PDMS and laser absorption at laser fluence 530, 1030, and 1530 mJ/cm² respectively. The ablation depth and width are increasing concerning laser fluence similar to the plume formation in the shadowgraph images. The PDMS starts degradation at 400-600 °C hence the crater starts forming over this temperature[89]. Moreover, the temperature at the interface increases up to 20 μs because of heat dissipation from the top surface. The maximum temperature at 1530 mJ/cm² is nearly 988 K which is higher than the degradation temperature in the simulation because of extra energy availability.[76] The extra available energy is incorporated into the pixel's velocity for the transfer mechanism. Moreover, the temperature at the interface of PDMS and ZnO is also increasing with an increase in laser fluence that corresponds to an increase in induced pressure for the transfer process.

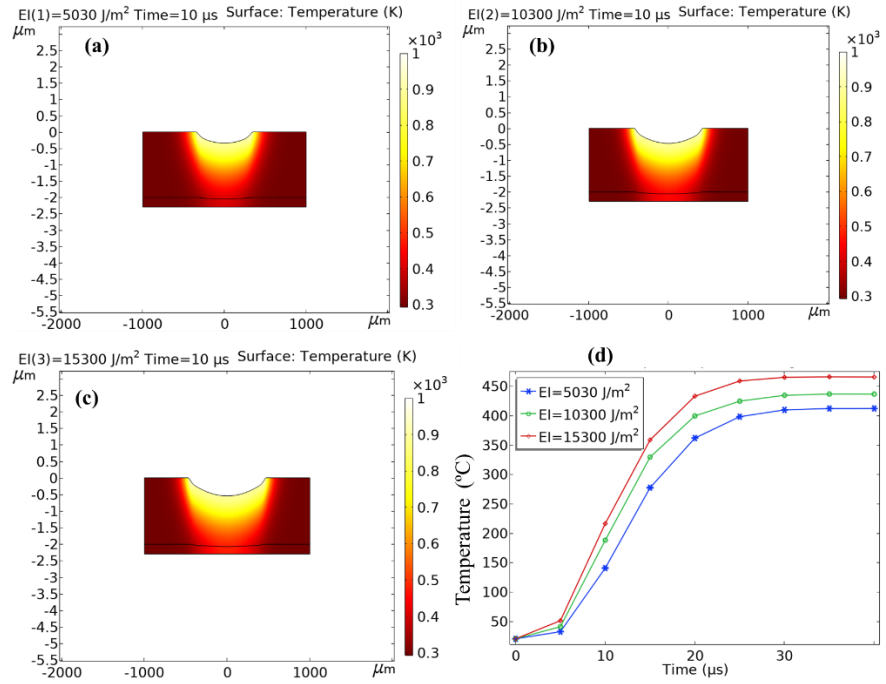


Fig. 6.2 (a) The PDMS sacrificial layer surface temperature at different laser fluences at a pulse duration of 10 μs, and (b) the temperature at the interface of a sacrificial layer at ZnO donor film.

6.1 Micro 3D printing

The ZnO structure is deposited in a thin film on the PDMS-coated silicon wafer to transfer the ZnO pixel using a laser decal transfer process. For three-dimensional structures, the minimum feature size is an important parameter for fabricating complex systems on the micron scale. Hence LDT is deployed for micro 3D printing for the line track with 90 % pulse overlap for uniform continuous and high-density pixel transfer [22]. Fig. 6.3 (a) illustrates the ZnO sputtered on the PDMS-coated donor substrate. Fig. 6.3 (b) – (d) shows the track deposited with 90 % pulse overlap at a laser fluence of 530 mJ/cm², 1030 mJ/cm², and 1530 mJ/cm², respectively. It can be observed that the track width is increasing with an increase in the laser fluence.

Furthermore, at laser fluence 1530 mJ/cm², the spattering amount is higher than 1030 and 530 mJ/cm². It is also observed that the printed structure at lower fluence shows a better surface finish than at higher fluence.[22] The track width is increasing concerning laser fluence due

to the high divergence of laser beam at higher fluences after the expansion of vapourised sacrificial layer. The temperature gradient influences the growth of the vapourised gas on the donor substrate after laser irradiation. The temperature gradient is responsible for the transfer quality of the materials on the receiver substrate. As the pressure increases, the transfer's ejection velocity will increase, which defines the printed structures' minimum resolution.

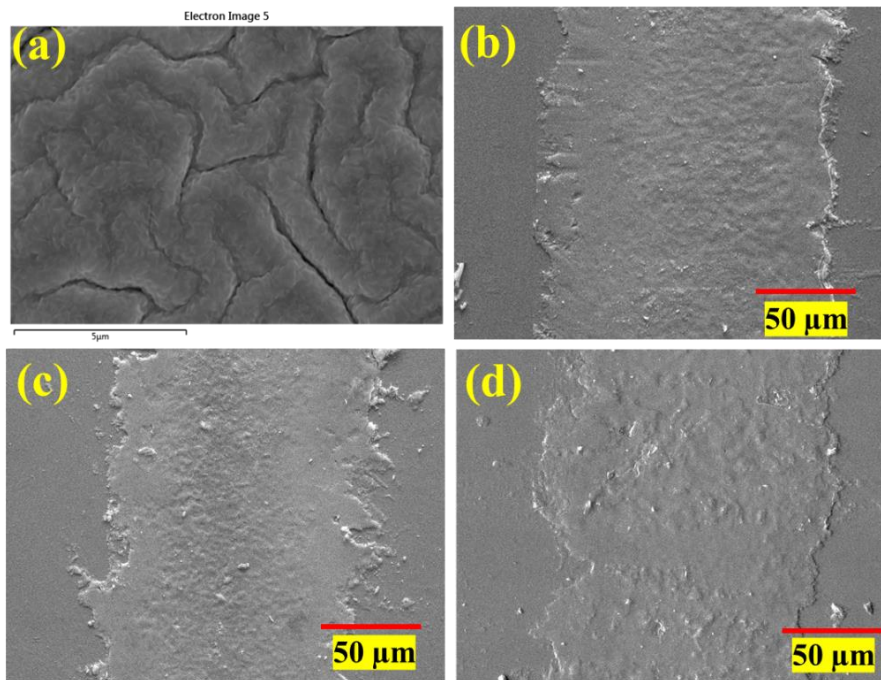


Fig. 6.3 (a) RF sputtered ZnO on the donor substrate. Micro 3D printed ZnO line track with 90% pulse overlaps at laser fluence (b) 530 mJ/cm², (c) 1030 mJ/cm², and (d) 1530 mJ/cm².

Fig. 6.4 shows the deposition thickness and track width of the printed line pattern. It can be worth noticing that with an increase in laser fluence, the track width is increasing while the deposition thickness is reduced. Moreover, the high fluence gives more irregular surfaces while the lower fluence provides less variation in the thickness of the deposited track. The spattering at the edge was more at 1530 mJ/cm² while it was uniform at the edges at laser fluence 530 mJ/cm² for high-resolution printing.

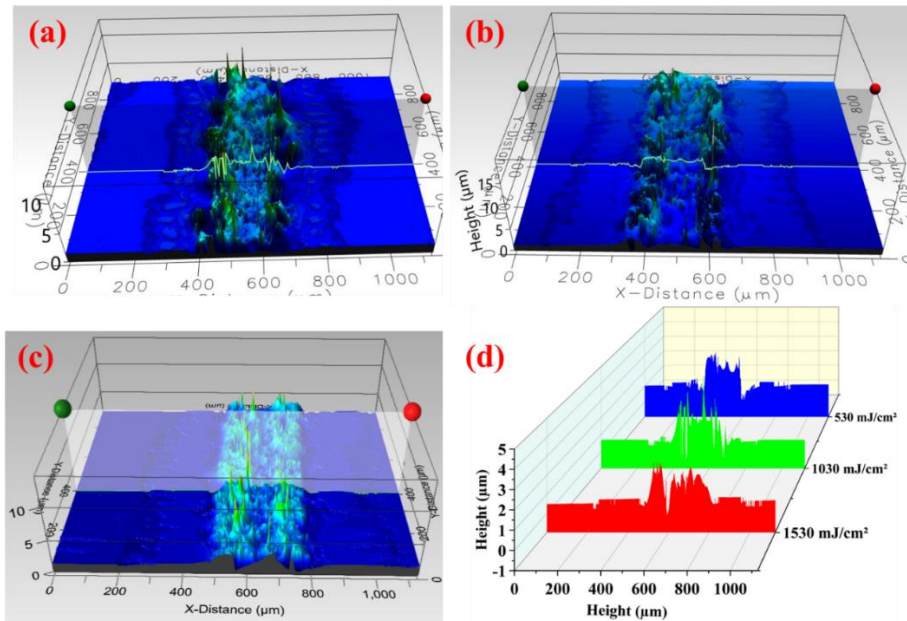


Fig. 6.4 The ZnO track printed on a silicon wafer at laser fluences (a) 530 mJ/cm², (b) 1030 mJ/cm², and (c) 1530 mJ/cm²

6.2 Plume formation

The shape of the plume is governed by the pressure developed by the vapourised PDMS sacrificial layer after laser irradiation. As the material is ejected from the plume, the pressure gets released with a decrease in the volume of the plume. Hence the plume shape can be correlated with the pressure developed by PDMS before the material ejection, similar to the ejection process of the high viscous liquid transfers [61]. Fig. 6.5 shows the shape of the plume at different time frames at laser fluence 530 mJ/cm² with an interval of 20 μs. It is interesting to observe that the plume has a dome shape and is growing with respect to the time frame before the material ejection from the substrate. The gaussian distribution of the laser beam governs the plume shape.

Furthermore, it can be observed that the plume starts forming after 20 μs of laser irradiation and reaches a maximum of 100 μs. After 100 μs, the material begins ejecting from the tip of the dome that, releases the pressure below the ZnO thin film.[48] Hence, there is no further increment in the plume length and width, as shown in fig. 6.6. The energy density of the gaussian beam profile is more at the central region.

At the same time, it decreases in the radial direction of the laser spot; hence, the materials' ejection starts at the dome's tip [90]. Fig. 6.6 illustrates that the maximum plume length and width before material ejection at 530mJ/cm² are 120 μm and 265 μm, respectively.

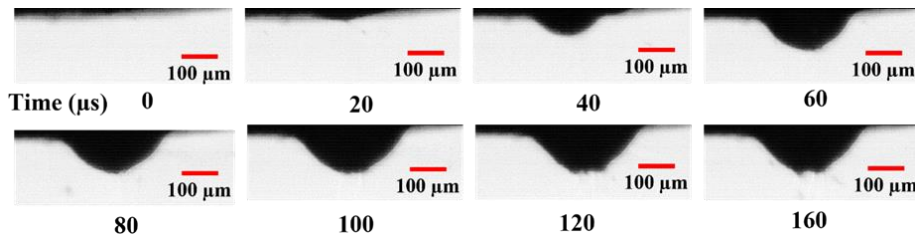


Fig. 6.5 The plume formation and expansion in laser decal transfer with time at laser fluence 530 mJ/cm²

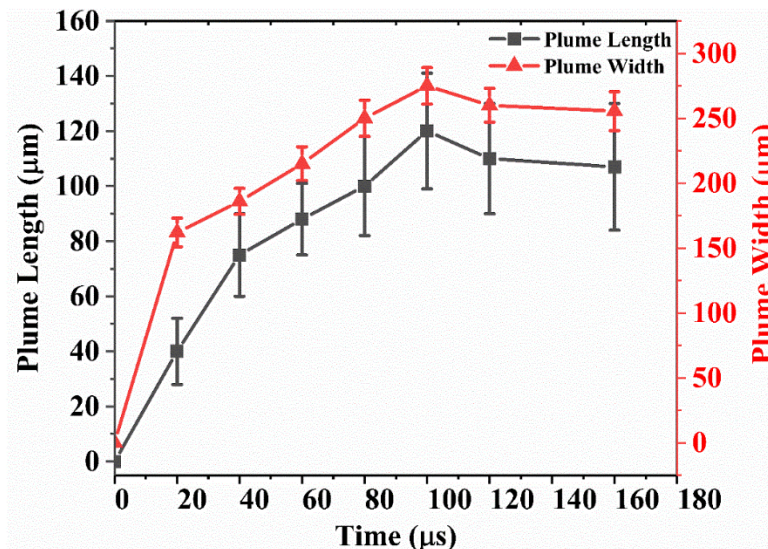


Fig. 6.6. The Plume length and width with a different time frame at laser fluence 530 mJ/cm²

6.3 Influence of laser fluence on plume

The time-resolved image of shadowgraphy is used to trace the particle at different time frames at three laser fluence 530, 1030, and 1530 mJ/cm². The PDMS sacrificial layer absorbs the laser energy and vaporizes due to the high temperature-induced. The vaporized PDMS induced high pressure over the ZnO thin film. This high pressure tries to decrease its pressure by expanding, which increases the plume size towards the laser beam direction.[91] Fig 6.7 shows the expansion of the plume shape with a time frame at different laser fluences, the plume

started forming after 40 μs of the laser irradiation and expanded with an increase in plume length and width to 160 μs . As the ultimate strength of the ZnO structure is reached, the ZnO plume gets ruptured at the dome of the plume heading towards the ejection of the material in single pixel form. It is worth noticing that the DRL layer is vaporized at 20 μs while the material is ejecting 160 μs due to expansion of high-pressure gas between substrate and donor film.

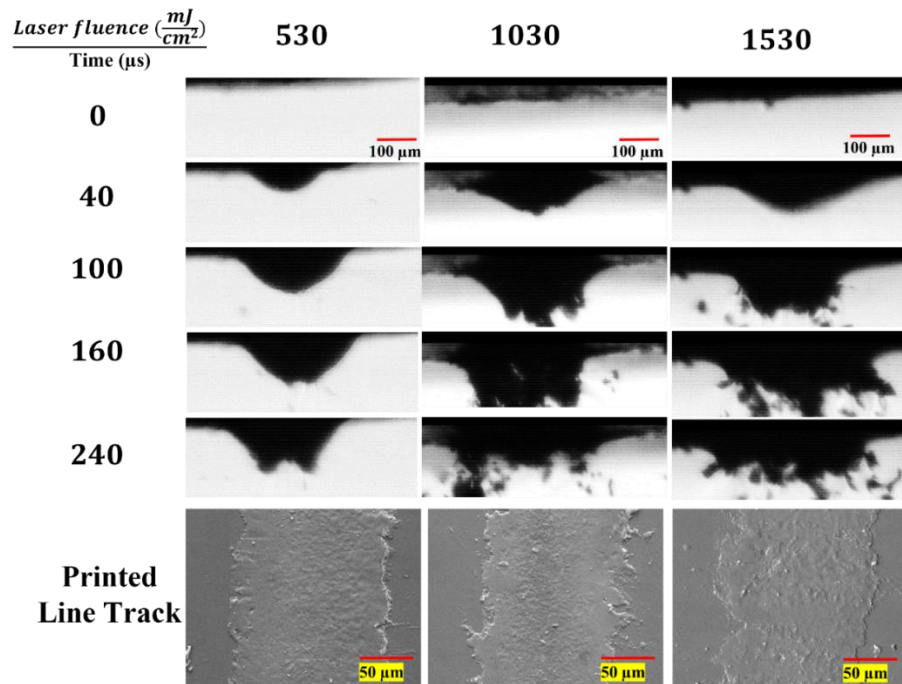


Fig. 6.7 The time-resolved image at different laser fluences 530 mJ/cm^2 , 1030 mJ/cm^2 , and 1530 mJ/cm^2 and printed line track on acceptor substrate at respective laser fluences.

In the case of 1030 mJ/cm^2 , the shape of the plume is larger than the 530 mJ/cm^2 , and ejection starts after 100 μs . This might be due to the early formation of plume because of high pressure developed before 40 μs . After 170 μs , the ejected materials crossed the frame of the high-speed camera image; hence it is not visible in this case. To measure the particle velocity, a central portion of the plume is the selection, and its position is traced with a time frame in the debris and bursting mode regime.

At laser fluence 1530 mJ/cm^2 , the plume gets busted before 100 μs in the form of fragmented particle that leads to the spattering of the material on the receiver substrate with poor resolution. However, the

track width of the printed line increases with laser fluence because of the higher deviation angle. In the case of 1530 mJ/cm^2 , the deposition width is uncertain because particles get fragmented in the small parts, leading to more spattering of the material.[92] The printed structure of ZnO with a $50 \text{ }\mu\text{m}$ spacing gap between the donor and acceptor is shown at different laser fluences. Hence it is difficult to quantify the deposition width in the busted mode of the transfer. The error bar shows the uncertainty in the pixel selection for the velocity measurement and the width of the printed structure. At higher fluence, the error bar is more due to several fragmented pixels available after the bursting in fig. 6.8. As the fluences increase to 1030 mJ/cm^2 , the length and width increase to $147 \text{ }\mu\text{m}$ and $331 \text{ }\mu\text{m}$. It is worth noting that the plume width is more than the spot size of the laser beam, i.e., $300 \text{ }\mu\text{m}$. This corresponds to an increase in the width of the track printed compared to the 530 mJ/cm^2 .

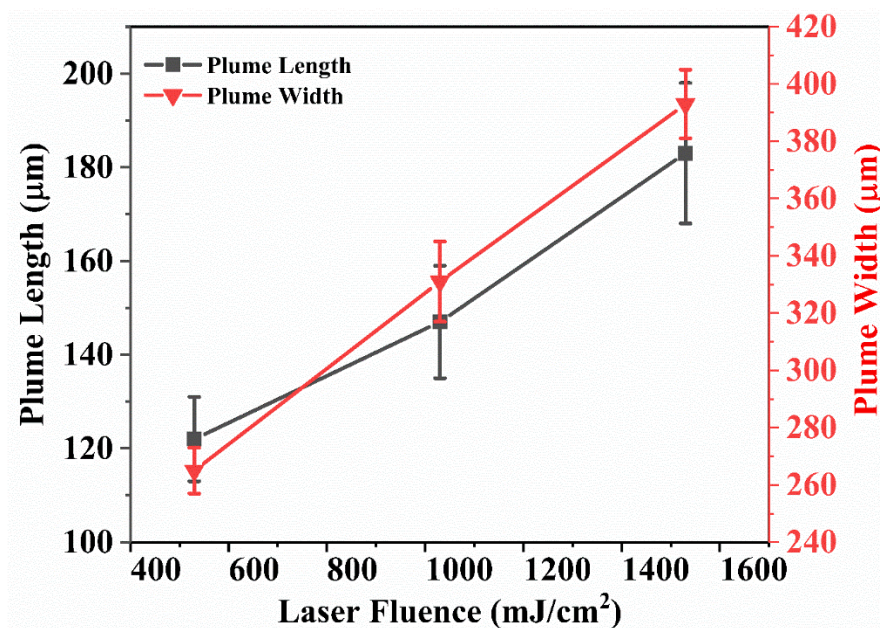


Fig. 6.8 Maximum plume size before material ejection at different laser

6.4 Mode of transfer

The angular deviation of the pixels from the laser beam path just after ejection defines the mode of the transfer process. The blue line shows the laser beam direction, and the red line shows the maximum

divergence of particle just after ejection Fig. 6.9 (a)-(c) shows the schematic of a mode of transfer of material while (d)-(f) shows the high-speed camera images using shadowgraphy at laser fluence 530 mJ/cm^2 , 1030 mJ/cm^2 and 1530 mJ/cm^2 respectively. It is observed that the angular deviation is $0\sim 1^\circ$, 13° , and 34° , as shown in fig 6.9 (d)-(f) from the laser beam line. This corresponds to an increase in the deposition feature size of the structure. Furthermore, from the time-resolved image, angular deviation less than 5° leads to the cap ejection mode, as reported by Ralph Pohl.[93] The plume formation is similar in the case of highly viscous fluid, while the ejection of the particle is similar to the transfer of metal from the donor substrates. The angular deviation of more than 30° leads to a bursting mode of the transfer where particles are ejected in multiple fragments, which leads to the material's spattering on the acceptor substrate. In the case of angular deviation $5 > \theta > 30^\circ$, the transferred material deposited with a larger size with some debris. Hence it is known as debris mode. It can be concluded that for the efficient transfer of material, the ejection of particles should be a cap regime. In contrast, for the continuous deposition of thin patterned structures, the debris regime will work for the three-dimensional structure building.

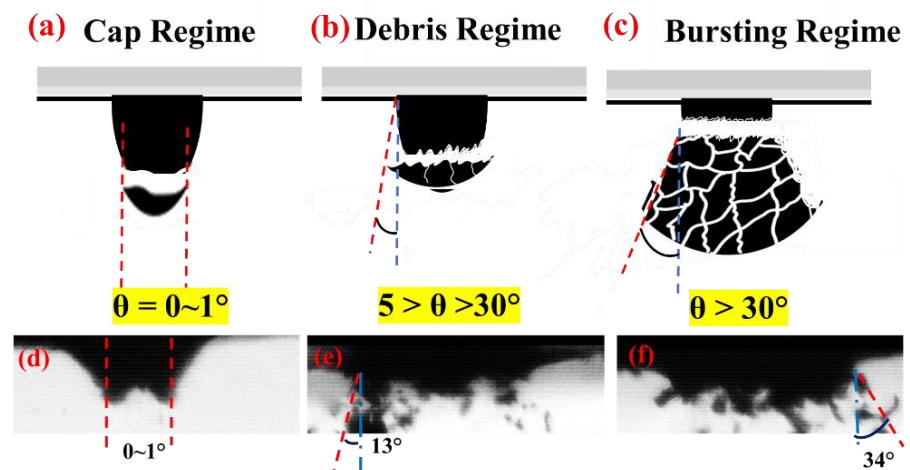


Fig. 6.9 Schematic of particle ejection mode in laser decal transfer process with angular deviation (a) cap regime with $\theta < 5^\circ$, (b) debris regime with $5 > \theta > 30^\circ$, (c) Bursting mode with $\theta > 30^\circ$, (d)-(f) shows the three modes of ejection at a laser fluence of 530 mJ/cm^2 , 1030

mJ/cm², and 1530 mJ/cm² respectively in time-resolved image just after the material ejection

6.5 Summary

In this work, solid-phase ZnO pixels are transferred in the line pattern using a Laser micro-3D printing process with a CO₂ pulsed laser at different laser fluence. A theoretical model is developed based on energy conservation, and numerical simulation is performed to estimate the temperature at the interface of the PDMS sacrificial layer and ZnO thin film. The theoretical model estimated the velocity of the material during the transfer mechanism. The following conclusions can be derived from the work:

- The maximum temperature is 1020 °C at laser fluence 530 mJ/cm² at the interface of the ZnO thin film and Sacrificial layer. The maximum velocity is estimated through energy conservation from the left energy after the required temperature is achieved. The maximum velocity at laser fluence 530, 1030, and 1530 mJ/cm² are 80, 360, and 504 m/s, respectively.
- The printed structure shows the uniform line printing at laser fluence 530mJ/cm², while the laser fluence 1030 mJ/cm² prints a more spattered edge with higher track width. In case of 1530 mJ/cm², the printed line shows high roughness more track width and more spattering at the edge of the line track.
- As the result of laser material interaction, the laser beam absorbs the sacrificial layer and induces a high-pressure gas bubble beneath of donor film that leads to the formation of a plume on the donor film. Due to high-pressure gas, the vaporized gas tries to expand and leads to an increase in the size of the plume shape.
- The angular deviation just after the ejection defines the mode of transfer of DRL-based micro 3D printing. If the angular deviation $\theta < 5^\circ$ known as cap regime, $5 > \theta > 30^\circ$ debris regime and $\theta > 30^\circ$ Bursting mode.

- The time-resolved image shows that the ejection mode in DRL-based micro 3D printing is a combination of ejection of LIFT of thin film with melting and high viscous liquid. The plume formation caused by the sacrificial layer suggested a LIFT of a high-density liquid regime, whereas the cap regime suggested a LIFT of a thin film with melting.

•

Chapter 7

Competences of μ -3D printing μ -scale structures for MEMS Applications

This chapter focuses on the different application of Laser μ -3D printing for the sensors fabrication that can be deployed in MEMS devices. The NiTi metals and ZnO material (nanostructure and thin film) was printed using μ -3D printing for sensing material. In this regard, a NiTi pixels were printed in solid phase to fabricate strain gauges on the flexible PET substrate for strain measurement. Moreover, the capability of same phase printing was more evident by the selective printing of ZnO nanostructure without any distortion in shape and its functionalities. At last, a ZnO based triboelectric nanogenerator was fabricated using continuous line printing of ZnO followed by hydrothermal growth for energy harvesting system application.

7.1 NiTi-based Strain Gauge.

Strain gauges are used on the surface of mechanical structure under tensile, compressive or fatigue loading condition to measure the strain or deformation in various engineering components. Conventially, it is made up of a flexible metallic foil, wire or specific material with a particular resistance that varies when subjected to strain. The most industrial strain gauges are made up of nichrome wire having good sensitivitry with change in deformation. These strain gauges have conventionally fabricated by using specialised procedures such as etching or wire bonding. With advances in technologies, it permitted the fabrication of strain gauge printing using 3D printing.[87]

Strain gauge printing includes depositing strain gauge material onto a substrate using additive manufacturing processes such as screen printing, contact printing or inkjet printing.[86][94] These technique has various advantages, including cost-effectiveness, design flexibility, and the possibility to develop customised strain gauges for specific applications. Researcher has explored different sensing material for the strain measurement such as silver nanowires[95], Layered Percolative

Films[96], CB-PDMS and CNT-PDMS [95][97]. NiTi is an alternative material having its super elasticity property that leads to high sensitivity towards mechanical strain. In this regard, a three-layer and five-layered NiTi strain gauge is printed on a flexible PET sheet of thickness 250 μm using laser μ -3D printing at laser fluence 1.03 J/cm^2 for strain measurement applications. The performance of the strain gauge is measured on universal testing machine during tensile loading condition at strain rate of 10 mm/min.

7.1.1 Morphology

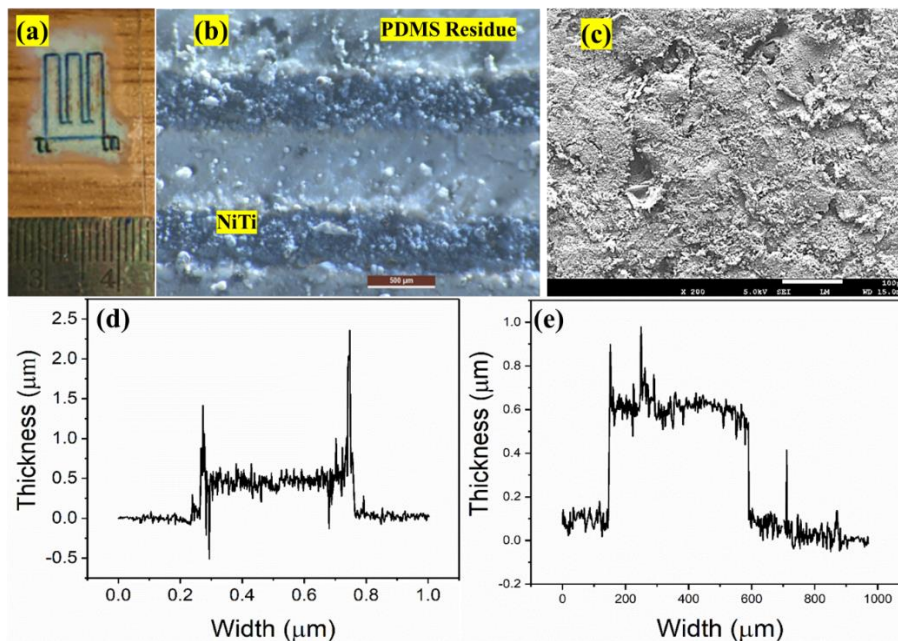


Fig. 7.1 (a) The NiTi printed strain gauge on the flexible PET sheet, (b) The NiTi pixel deposited on the PET substrate, (c) high magnification surface morphology of three-layer NiTi at laser fluence 1.03 J/cm^2 , (d) and (e) thickness of three-layer and five-layer strain gauges respectively.

The five-layer printed strain gauge is shown in fig 7.1. It can be observed that the NiTi-transferred pixels are well connected which leads to shoes the resistance of the printed strain gauge. A few amounts of PDMS residue are also deposited on the PET sheet along with NiTi pixels. The 3-layer gauge and 5-layer gauge have average thicknesses of 0.54 μm and 0.64 μm , respectively. The five-layer structure shows lower

thickness than anticipated value because of its material loss owing to spreading during printing. However, the width of the printed line is 450 μm , which is more than the laser beam's spot diameter (300 μm) due to a more gap between both the substrate.

7.1.2 Performance analysis

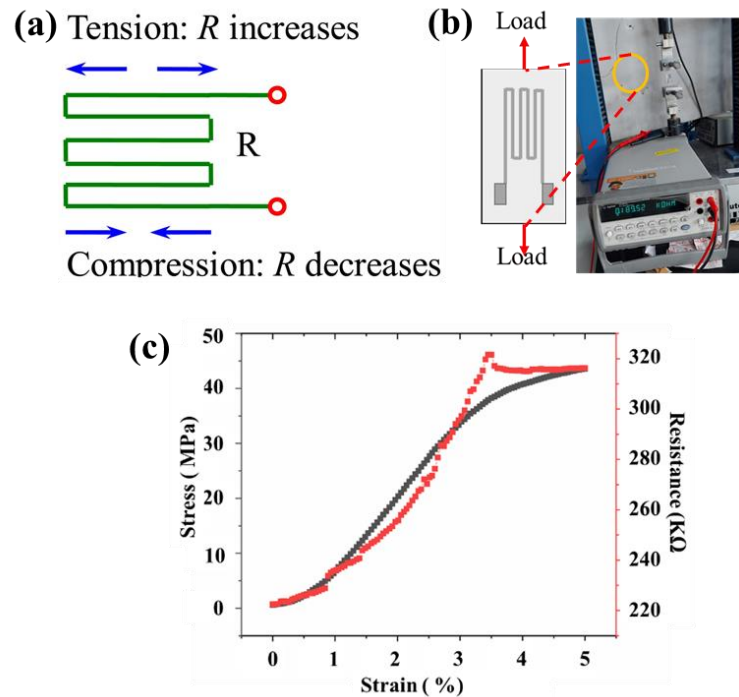


Fig. 7.2 shows (a) The principle of the strain gauge, (b) strain gauge loading condition on the universal testing machine and (c) stress induced on the PET sheet and the performance of strain gauge in terms of resistance.

A copper wire of 0.5 mm diameter with resistance 0.2 Ω is connected with both the terminal of the strain gauge and the connected digital multi-meter. Two probe method is used for the resistance measurement during the tensile loading in an axial direction. Fig. 7.2 (a) show the electromechanical response of the strain gauge. The resistance R increases when tension is applied to it and it decreases when it is compressed as shown in The response of strain gauge shows linear variation in the resistance with respect to strain in longitudinal directions.[98] However, the PET shows the ductile mode of failure due to elastic and inelastic regions in the stress and strain curve. A similar

behaviour is observed in the resistance of NiTi pixel, and it reaches to a maximum value at the upper yield point of the PET sheet and starts decreasing. The resistance of the printed sensor is varied due to an increase in the intermetallic spacing between the NiTi pixels.[99]

$$\mathbf{G.F} = \left[\frac{\frac{\Delta R}{R}}{\varepsilon} \right] \quad \mathbf{6.1}$$

The gauge factor evaluates the sensor's sensitivity. As a result, the larger the gauge factor, the greater the sensitivity to strain %. The gauge factor (G.F) of the printed sensor is calculated by eq. 6.1

Figure 7.3 (a) depicts 5 layered strain gauge responses with strain percentage. It turns out that the resistance and $\Delta R/R$ have a linear fit with $R^2 = 98\%$. Furthermore, the reaction at low strain % is significantly less linear due to insensitivity at low strain %. Furthermore, strain above 2% causes more variance in resistance, making the sensor more sensitive to higher strain percentages. The linear fluctuation of $\Delta R/R$ with strain % in Fig. 6.3 (b) corresponds to a constant gauge factor of printed sensors. The gauge factors of 3-layered strain gauges and 5-layered strain gauges are 9 ± 3 and 13.5 ± 1.5 , respectively.

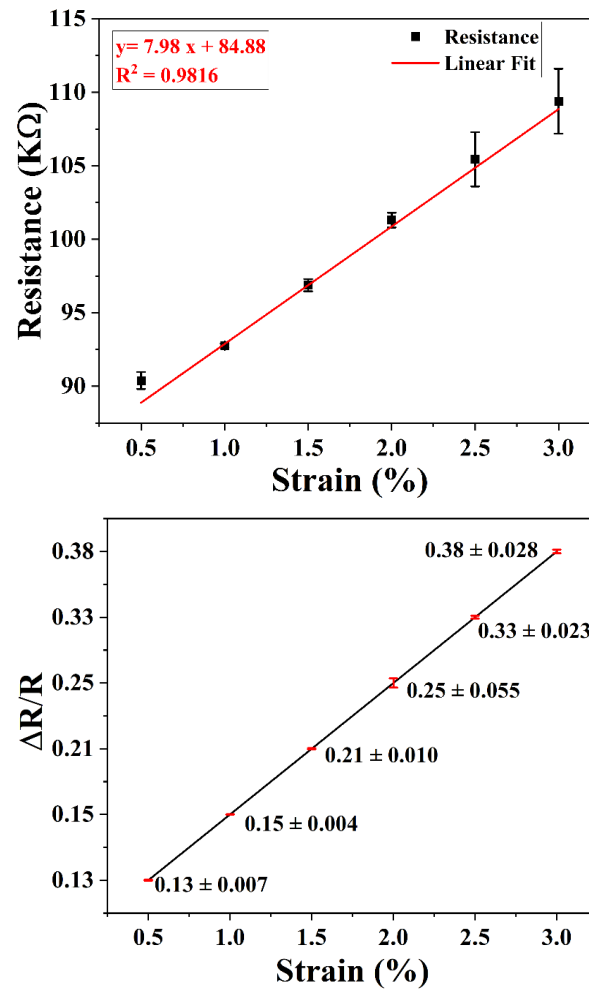


Fig. 7.3 (a) Resistance and $\Delta R/R$ with different strain % of 5 layered strain gauge

- **Three-dimensional strain measurement by rosette strain gauge**

A rosette strain gauge is a group of strain gauges organised in a certain design to measure stresses in many directions. It is widely utilised in engineering and scientific applications that involve complicated strain measurements in engineering components. The rosette form of strain gauges allows for the assessment of both the amount and direction of strain along distinct axes. The three-element rosette known as rectangular rosette is the most popular form of rosette strain gauge layout. It is made up of three strain gauges that are at right angles to each other. Typically, the angles between the gauges are 0° , 45° , and 90° , making a symmetrical pattern. Strain measurements may be taken along the axial, transverse, and shear axes using these angles. Fig. 7.4 (a)

Shows the 7-layer rosette strain gauge printed on the flexible PET substrate by micro 3D printing. The copper wire is fixed at a pad of each strain gauge using silver paste and copper tape. Fig 7.4 (b) and (c) closer view of the printed strain gauge at higher magnification. It is evident from the EDX analysis that the NiTi material is deposited nearly in equiatomic percentage as shown in fig. 7.4 (d). The loading condition is shown in fig. 7.4 (e) with each strain gauge concerning the direction of loading. The printed strain gauge is mounted on the universal testing machine, and tensile force is applied along the strain gauge's longitudinal axis with 2 different straining speeds of 0.1 mm/min and 1 mm/min. The electromechanical response is measured during the loading condition in the form of resistance.

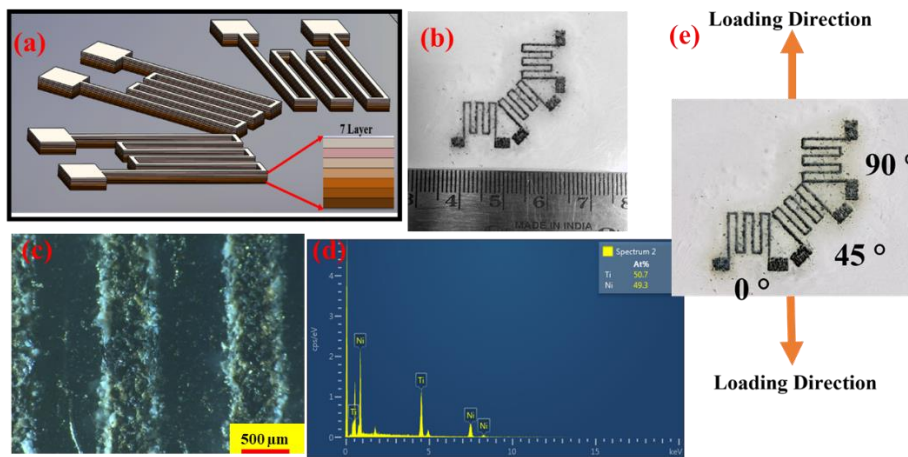


Fig. 7.4 (a) CAD model of 7-layer rosette strain gauge, (b) printed Strain gauge, (c) optical image of gauge at higher magnification, (d) EDX analysis, and (e) Loading condition

Fig 7.5 shows the $\frac{\Delta R}{R}$ and stress-induced in the PET sheet in all the loading conditions. It is evident from the plot that the percentage $\frac{\Delta R}{R}$ increases with an increase in strain and stress in the deposited materials.[86] Moreover, the 0-degree strain gauge shows the highest response while the 90 degree shows the least response due to less stress induced in the latitudinal direction. Also, it can be seen that the printed strain gauge shows a better response at lower strains. As the strain

increases the sensitivity is not uniform. This might be due to an increase in the pixel-to-pixel distance at higher straining of the substrate.

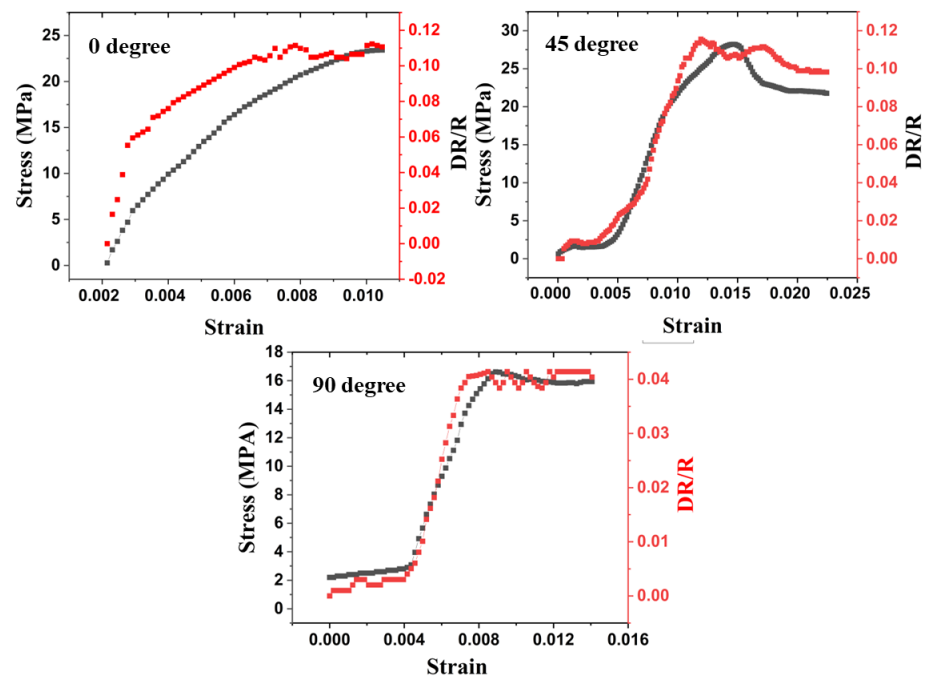


Fig. 7.5 Electromechanical response of the strain gauge at strain speed 1 mm/min.

Fig. 7.6 shows the response of the strain gauge at 0.1 mm/min strain speed. It can be observed that the stress at a higher strain rate is less compared to the low strain rate due to the high impulse force generated during loading. Furthermore, the electromechanical response in 45° and 90° are nearly equal while 0° shows a higher percentage change in resistance value.

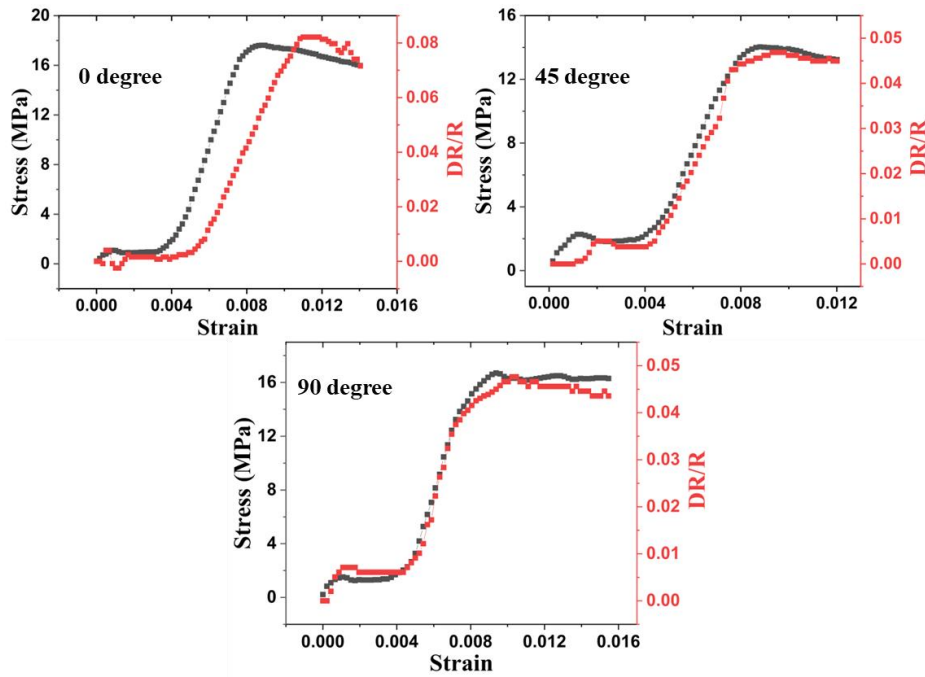


Fig. 7.6 Electromechanical response of the strain gauge at strain speed 0.1 mm/min.

7.2 ZnO-based UV-LED for opt mechatronics application.

Due to the high flexibility and its simplicity of process, researchers have played with a variety of materials, including metal, polymers, and organic materials, for the fabrication of optical and electronic devices, including alcohol-soluble polyfluorene (PFN)-based LEDs [101], organic light-emitting diodes (OLEDs), tri-color OLEDs, and optical waveguide circuits [100] etc. Similarly, ZnO is a functional material having affinity to absorb UV light efficiently and create electron-hole pairs, resulting in tangible photocurrent or photovoltage outputs. ZnO nanostructures are ideal for UV applications, which are widely employed in optoelectronics, photonics, and piezoelectric applications in the electronic industries.[102][103] The broad energy bandgap (3.37eV), biocompatibility in various forms (nanorods, nanowires) [10,11], excellent transparency in the visible spectrum, and heavily doped with loose electron density are all advantages of this material. It also possesses low-temperature thin-film fabrication capacity, cheap material costs, and is non-toxic, making it excellent for LEDs, biosensor applications [106], thin-film solar cells, and high-temperature

electronics devices.[107] ZnO's most essential piezoelectric feature makes it appropriate for most actuator and sensor applications.[108] For the low-temperature synthesis of ZnO nanorod surfaces, several patterns were deposited utilising the LIFT technique under air and vacuum conditions.[109][110] An attempt is made to transfer ZnO nanostructure using laser decal transfer based Laser μ -3D printed for selective deposition of ZnO nanostructures on the flexible PET substrate. To retain the morphology, of nanostructured a short pulse laser i.e. (pulse width 9 ns) is used to avoid any detrimental effect on the morphology and functionality of the nanostructure. The process undergoes thermal heating and vaporization that may distort the ZnO nanostructures hence, a numerical simulation was performed to select the process window for transfer of nanostructures for optoelectronics applications.

7.2.1 Numerical modelling of ITO sacrificial Layer and ZnO donor film

The sacrificial layer and ZnO are represented as a rectangle with a thickness of 100 nm and a length of 3000 μ m, while the donor materials of a thickness of 500 nm and a length of 3000 μ m. the laser beam hit at the central top of sacrificial layer. The complete geometry is represented by a quadrilateral mapped mesh with element sizes of 10 nm for thickness and 50 nm for length. The COMSOL material library's for ZnO thermal and structural characteristics are utilised.[111,112]

Table 7.1 Input Parameters & material properties

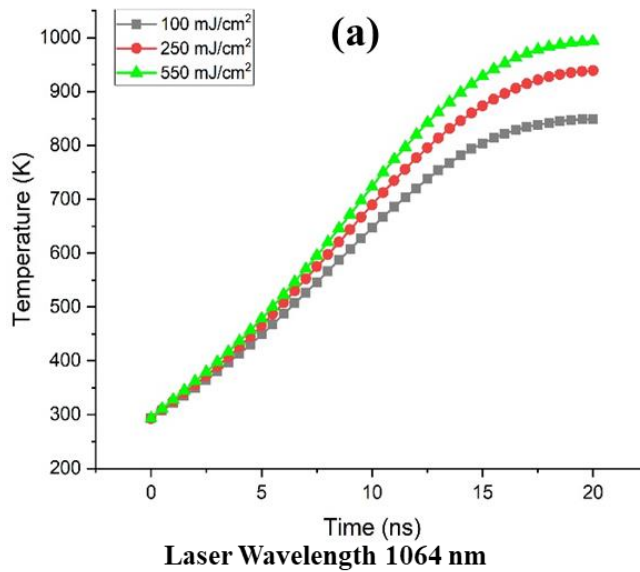
Parameters/Properties	Values	ITO	ZnO
Laser Spot Diameter	1 mm		
Pulse Duration	9ns		
Laser Fluence	100, 250, and 550 mJ/cm ²		
Convection heat coefficient	10 W/K		
Emissivity	0.3		
Density		7120 kg/m ³	5510 kg/m ³
Thermal Conductivity		10 W/mK	35 W/mK
Specific heat		340 J/kgK	620 J/kgK

Table 7.2 Optical properties of ITO sacrificial layer

Wavelength / <i>optical parameter</i>	355nm	532nm	1064nm
R	0.31	0.11	0.01
α (m^{-1})	4×10^6	7.9×10^5	1.1×10^6

- **Influence of laser wavelength and laser fluence**

The ITO sacrificial layer is used to avoid the heat dissipation to ZnO nanostructures at with nanosecond pulsed laser. The wavelength dependent absorption coefficient is used for the numerical simulation. Three different laser fluence 100, 250, 550 mJ/cm^2 and three different laser wavelength 1064, 532, and 355 nm are used in the simulation. The maximum temperature will achieve at high laser energy and minimum temperature will achieve at lower laser fluence i.e. 550 mJ/cm^2 and 100 mJ/cm^2 respectively.



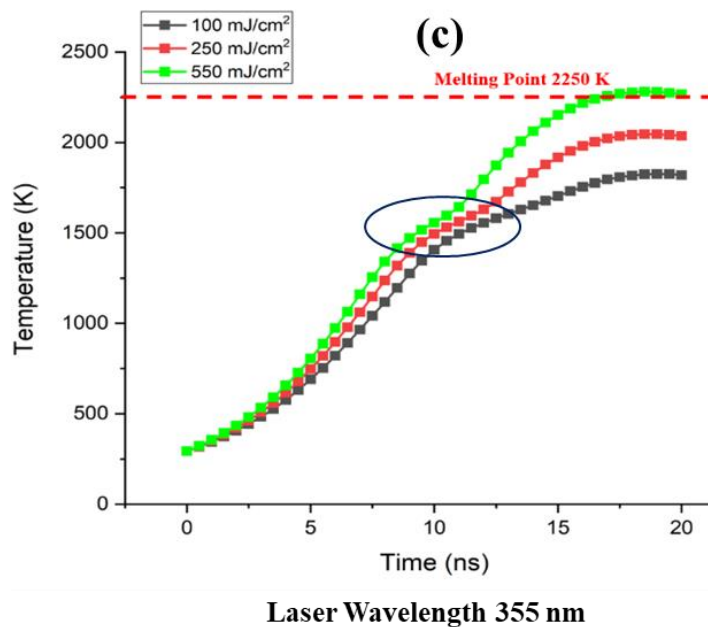
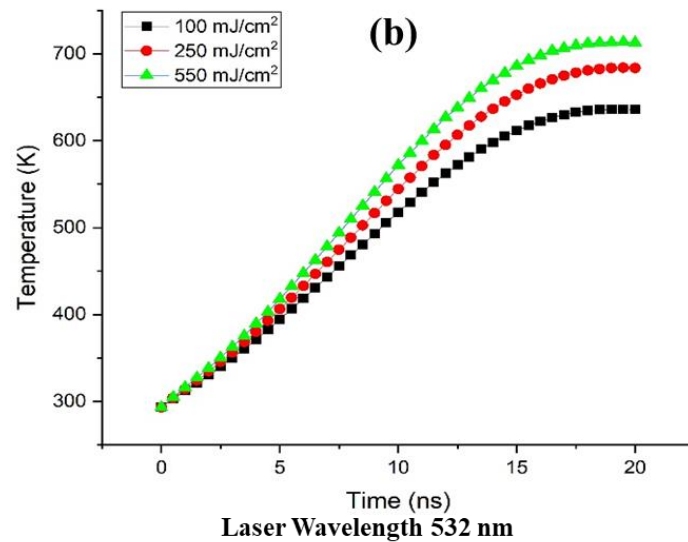


Fig. 7.7 The temperature induced with 9 ns pulse width at interface of ITO and ZnO film at various laser wavelength and fluence.

Fig. 7.8 (a) plot shows the interface temperature of ITO sacrificial layer and ZnO donor film at 1064 nm wavelength with 9 ns. The plot shows that the maximum temperature is reaches nearly 1000 K at 550 mJ/cm² while the minimum temperature is 840 K. In case of 532 nm laser wavelength, the maximum and minimum temperature are 730 and 640 K respectively. This shows that the ITO sacrificial layer absorbs 1064 nm laser better than 532 nm. In case of 355 laser wavelength, the

maximum temperature is crossed the melting point of ZnO i.e. 2250 K while the minimum temperature is 1835 K. Hence it can be concluded that the 355 nm laser wavelength absorbs maximum amount of laser energy in ITO sacrificial layer as shown in fig. 7.5. Moreover with 355 nm wavelength, the plot shows the change in the slope at 10 ns marked in blue circle signify the phase change of the ITO sacrificial layer over 1500 K.

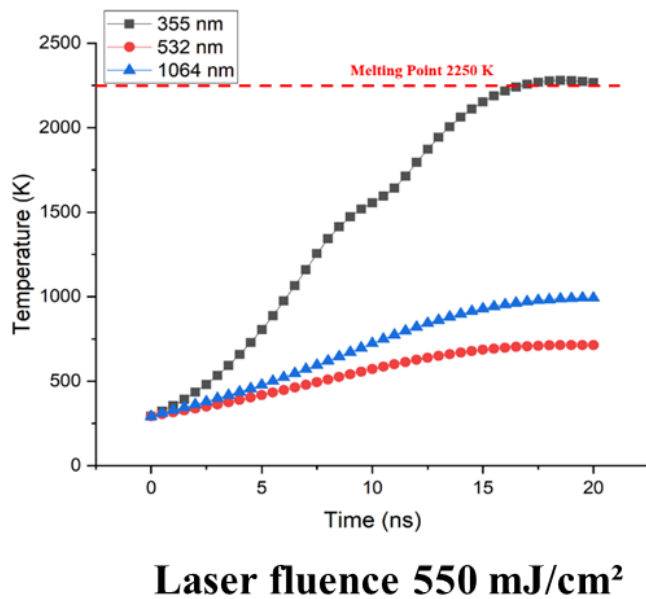


Fig. 7.8 The variation in interface temperature different wavelength with laser fluence at 550 mJ/cm²

- **Influence of sacrificial layer thickness**

The sacrificial layer ablates the transfer the material by retaining the donor physical and chemical properties of the donor film. Hence the sacrificial layer thickness plays an important role for the ejection of material. Four different thickness of ITO were varied at laser fluence 550 mJ/cm² at 355 nm laser wavelength. Fig. 7.9 shows that with increase in sacrificial layer thickness from 50 nm to 100 nm the temperature at interface is increasing while the further increment in does not shows the same increment in the temperature rise at 150 nm. At 200 nm thickness the temperature is same as 150 nm. This is due to the penetration depth in the ITO sacrificial layer of laser beam. As the

sacrificial thickness is more than the penetration depth the temperature is not rising over at interface. Hence, the optimum sacrificial layer should not cross the penetration depth of the laser beam.

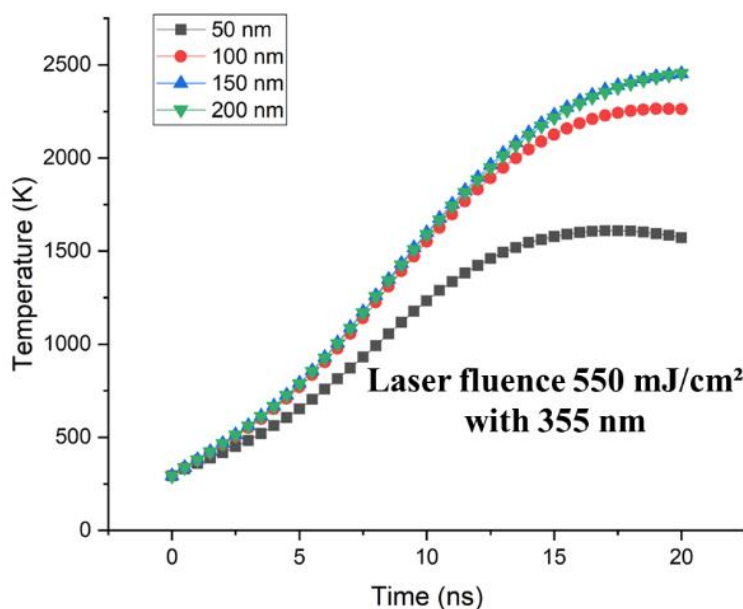


Fig. 7.9 The interface temperature at different sacrificial layer thickness with 550 mJ/cm² laser fluence.

7.2.2 ZnO nanostructure printing

Figure 7.10 (a) and (b) demonstrate the surface morphology of ZnO nanostructure on donor film before transfer and an acceptor substrate. The FESEM picture revealed an as-developed homogenous ZnO structure from the donor film. At 550 mJ/cm², the material shows complete ablation from donor substrate and the transferred material shows complete melting of the ZnO nanostructure. In Fig. 7.11 (a), the high-speed camera picture depicts material transfer from donor to acceptor substrate after 5 s of laser irradiation. Furthermore, the time-resolved imaging approach determined the velocity of material during transfer to be 960 m/s. Figures 7.11 (b) and (c) show FESEM images of the donor and acceptor substrates after they have been transferred.

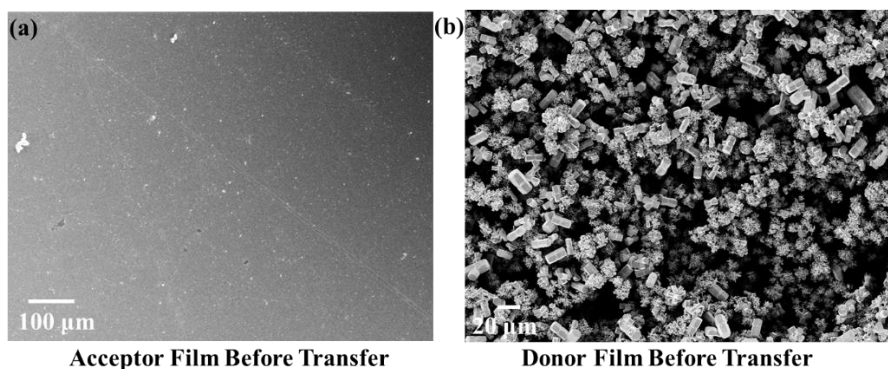


Fig. 7.10 The acceptor substrate and donor substrate before the transfer of ZnO nanostructure

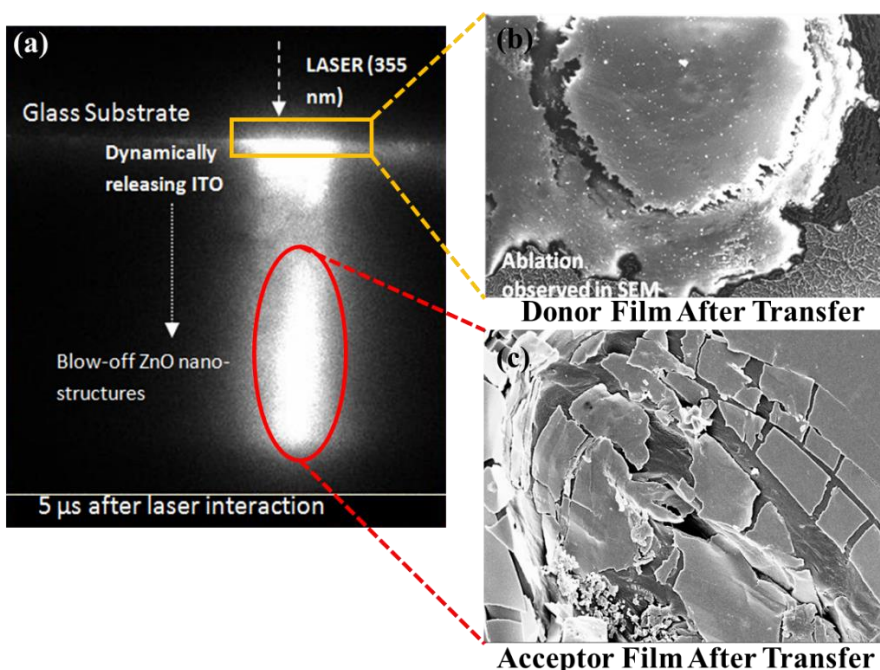


Fig. 7.11 (a) Time resolved image at 550 mJ/cm^2 laser fluence with high speed camera, (b) donor substrate after transfer, and (c) melted ZnO on acceptor substrate.

Figure 7.12 depicts the LIFT of ZnO nanostructures with the same donor at a laser fluence of 250 mJ/cm^2 . The ejection velocity reached 200 m/s using time-resolved imaging, with some fragmentation in the form of nanorods. It is worth noting that the size of the nanorods decreases from the donor substrate owing to ZnO thin film separation heating, which compromises the shape of hexagonal nanorods. The numerical

simulation reveals that the temperature is almost 2000 K when the phase of ZnO nanostructures begins to change.

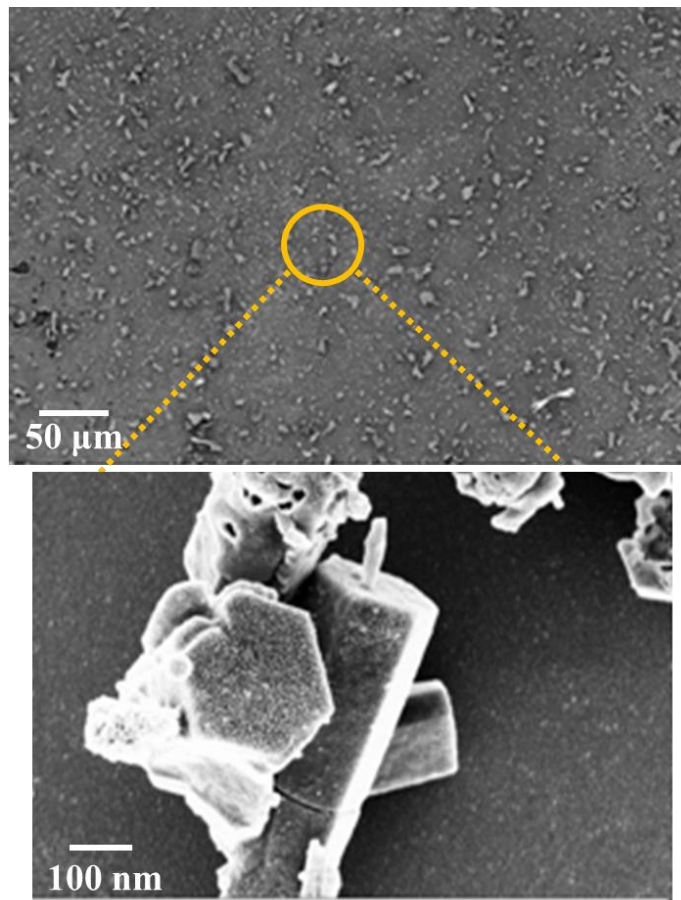


Fig. 7.12 (a) Low and High magnification image of printed ZnO at 250 mJ/cm².

Similarly, with a laser fluence of 100 mJ/cm², the deposition speed is just 90 m/s. Fig. 7.13 illustrates the deposited ZnO nanorods are in the shape of clusters with considerable fragmentation; comparable results were achieved by F. Claeysens [109]. The length of the implanted

nanorods is greater than $250\text{mJ}/\text{cm}^2$. It should also be mentioned that more nanorods are found in $100\ \mu\text{m}^2$ at $100\ \text{mJ}/\text{cm}^2$ than at $250\ \text{mJ}/\text{cm}^2$.

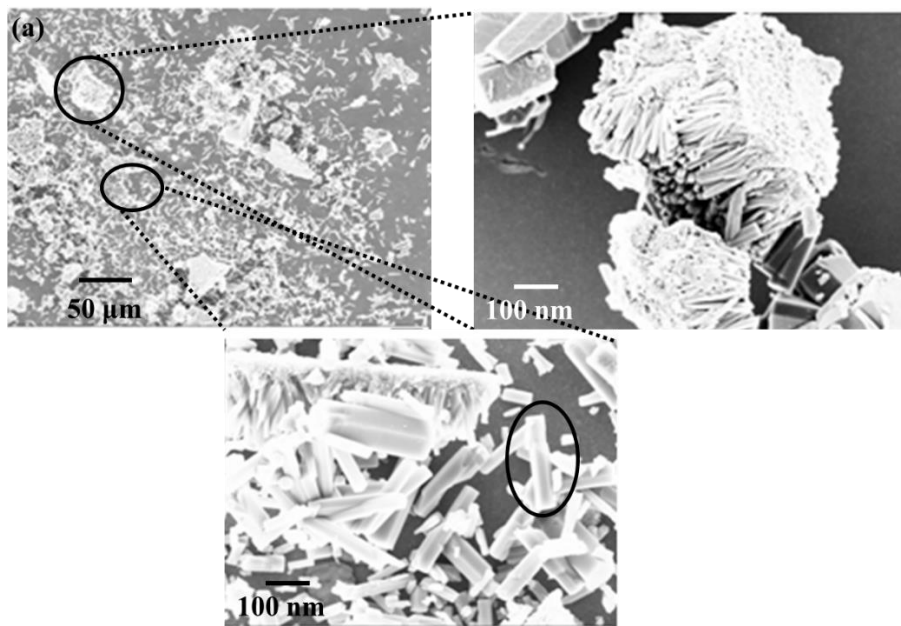


Fig.7.13 (a) The transferred ZnO nanorod at $100\ \text{mJ}/\text{cm}^2$. A cluster of nanostructures on acceptor substrate in high magnification image.

X-Ray diffraction is used to analyse the structural characteristics of ZnO nanorods on both the donor substrate and the acceptor substrate before and after the transfer. The XRD patterns of pure and transferred ZnO samples at $100\ \text{mJ}/\text{cm}^2$ are shown in Figs. 7.14 (a) and (b), respectively. JCPDS data (36-1451) is used to observe and confirm the crystallinity and crystal phases of pristine and transplanted ZnO nanorod. Between 32 and 37.5 angles, the usual ZnO hexagonal nanorod patterns are noticed. In addition, both the pristine and transferred ZnO samples—apart from substrate material show no secondary phase. When the laser interacts with the donor substrate during the deposition, thermal strain is produced that causes the noticeable peak deterioration to be seen in the transferred ZnO layer.

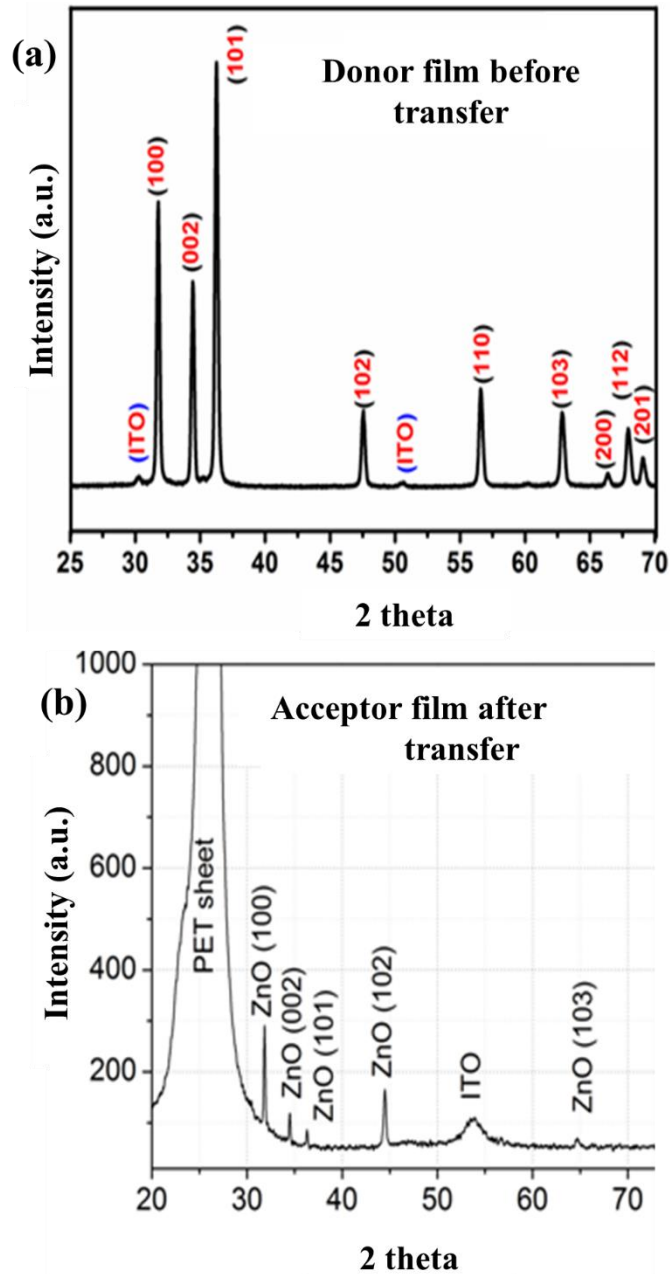


Fig. 7.14 (a) and (b) XRD spectra of donor before printing and acceptor after printing at laser fluence 100 mJ/cm^2

Photoluminescence spectra of the ZnO donor film and the LIFT deposited ZnO across a broad range (300-800 nm), respectively, are shown in Fig. 7.15 (a) & (b). The samples exhibit both Near Band Emission (NBE) and Defect Level Emission (DLE). Additionally, the intensity ratio of DLE to NBE for the material's defect condition is computed. It is observed that the imperfection was reduced from 3.6 (donor film) to 0.16 (LIFT deposited ZnO). It is also demonstrated that

the near band emission of ZnO is excited by laser energy at 355 nm. As a result, following the deposition, the intensity of near band emission at 370 nm rises. The yellow-orange defects in the donor film can be seen in the defect band emission, which is shifting towards the red defect in the LIFT deposited defects.

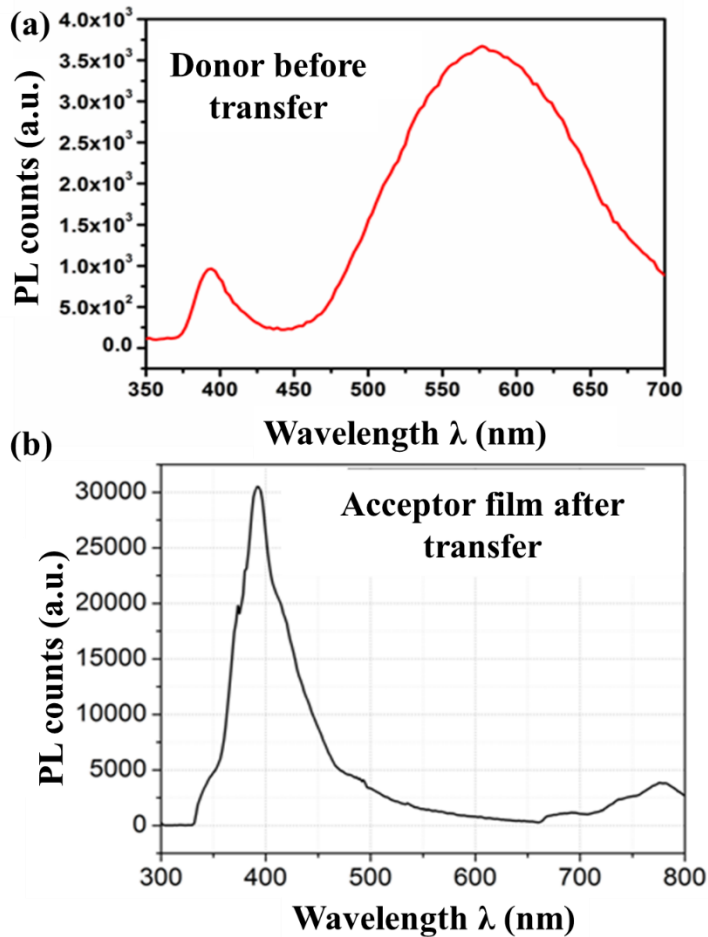


Fig. 7.15 (a) PL spectra of donor film and acceptor a at laser fluence 100 mJ/cm^2 .

7.3 Micro-3D printed ZnO based Triboelectric nanogenerator.

A triboelectric nanogenerator (TENG) is an energy harvesting device that converts mechanical energy into electrical energy by using the triboelectric phenomenon. The triboelectric effect is a phenomenon that occurs when specific materials come into contact with another material and subsequently separate. A TENG's basic operation entails two layers or surfaces formed of different materials. One material is having affinity to accept the charge known as tribonegative material, while the another

material is having affinity to donate the charge known as tribo-positive material. When these surfaces come into contact the tribo-positive surface donate the electron and tribo-negative accept the electron leading a flow of current in bothe electrode. As they start separation, the charge transfer takes place due to electro static induction hence current and voltage starts decreasing slowly as shown in fig. 7.16.[113][114]

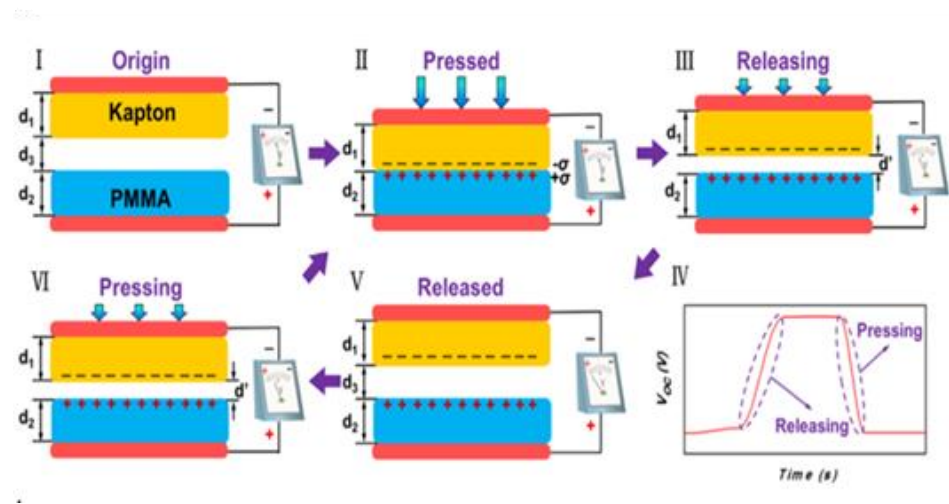


Fig. 7.16 The operating principle of the contact mode TENG.

TENG materials are selected wisely to have varied triboelectric characteristics, which means they tend to acquire or lose electrons when in contact. Typically, one material is an electron donor (loses electrons) while the other is an electron acceptor (gains electrons). Both the materia/ electrode can be configured in a variety of ways, including vertical contact-separation mode, lateral sliding mode, and single-electrode mode. These arrangements govern how the two surfaces interact with one another and how mechanical energy is turned into electrical energy.[115][116]

Currently, TENGs have received a lot of interest in recent years because of their ability to capture energy from numerous vibration sources in our surroundings. They may be used to gather energy from human motion, such as walking or tapping one's fingers, as well as natural sources like as wind, water, and vibrations.[117] Its has high energy conversion efficiency, a lightweight and flexible design, and compatibility with a

wide range of applications . It is used in a variety of applications, including self-powered wearable devices, smart textiles, biomedical sensors, wireless sensors, and portable electronics. It has potential to provide a sustainable and renewable source of power for small-scale electronic devices, decreasing the need for batteries and other energy sources.

In this regard, a triboelectric nanogenerator were fabricated using ZnO as tribo negative material and FEP as tribo positive substrate. ZnO material were printed using laser μ -3D printing on ITO coated glass substrate in line pattern as seed layer for the nanostructure growth. The FEP sheet has copper tape attached from the back side to collect the charge from the surface while the curved polyimide is used for the separation mechanism.

The ZnO seed donor film is coated using RF sputtering on PDMS coated silicon wafer and then the laser μ -3D printing is deployed for the transfer of ZnO pixel on ITO coated glass substrate. Copper coated FEP is used as tribo-positive for the triboelectric devices. Fig. 7.16 (a) shows the schematic of the ZnO based triboelectric nanogenerator for energy harvesting and (b) shows low and high magnification of ZnO printed on the glass substrate of $2 \times 2 \text{ cm}^2$. The ZnO nanostructures are printed in line track with track width of $600 \mu\text{m}$.

- Device fabrication and Structural morphology

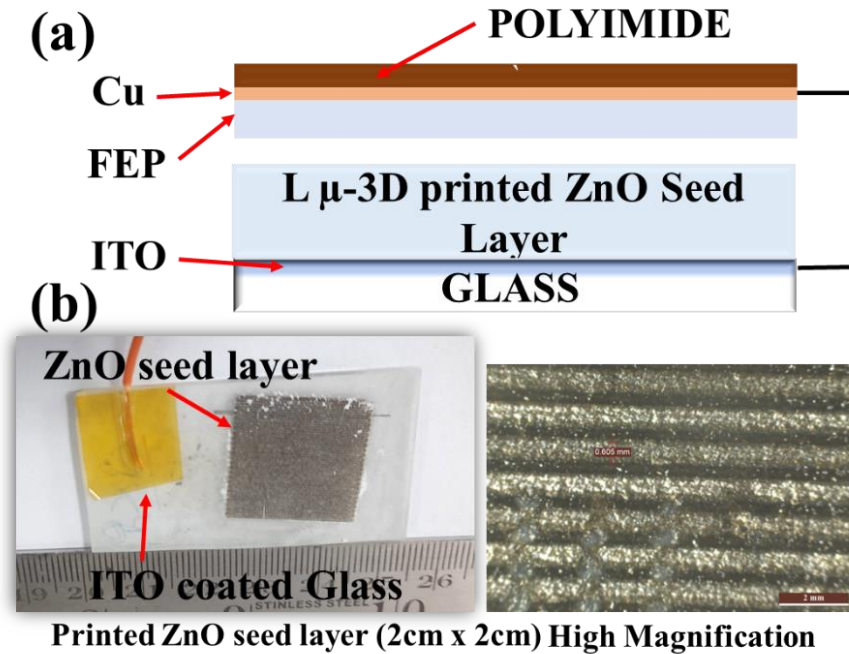


Fig. 7.17 (a) Schematic of ZnO base triboelectric nanogenerator and (b) L- μ 3D printed ZnO seed layer printed on ITO coated glass.

ZnO nanostructures are grown by hydrothermal process dipping the printed seed layer on ITO glass in mixture of 0.1 M Zinc Nitrate and 0.1 M HMTA in distilled water. The solution is kept in oven at 110 °C for three hours.[118] Fig. 7.17 (a) shows the grown nanorod over the line pattern seed layer,(b) and (c) high magnification area scan the elemental composition of ZnO by EDS analysis. Since the seed layer is transfer on the acceptor substrate hence the growth of nanostructure is not in same phase as observed in the x-ray diffraction peak in fig. 7.14 (d). ZnO and ITO peaks are identified with respect to printed device. ZnO peaks are at 2 theta 33.29° (100) plane, 37.50° peak of (101) plane, 65.8° (103) plane and at 78.5°C (202) plane. The substate phases are also observed at ITO (440) and (622) planes. Fig. (e) shows the final device for testing.

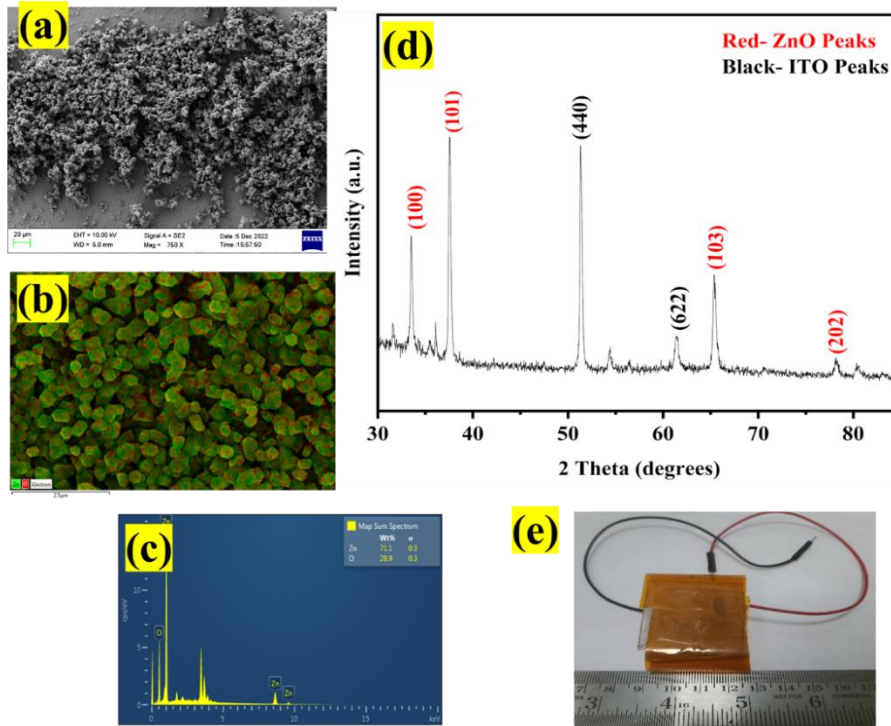


Fig. 7.18 ZnO nanostructures grown on the Laser μ -3D printed ZnO seed layer, (b) composition of nanostructure by EDS analysis, (c) X-ray diffraction of ZnO shows different phases of ZnO and ITO substrate, (d) final triboelectric nanogenerator.

- **Performance analysis**

The performance of Tribo-electric nanogenerator is measured in terms of open circuit voltage and short circuit current. The open circuit voltage is measure using an oscilloscope and short circuit current by an electrometer. The fabricate device is configured in vertical contact and separation mode, hence a continuous tapping is done at different tapping rate (RPM) and response is measured. Fig. 7.18 show the current and voltage harvested at tapping rate 200 rpm, 350 rpm.

As the FEP sheet (tribo-positive) starts coming towards the ZnO tribo-negative surface, due to the electrostatic induction the potential difference is induced between both the electrode and induces the charge transfer from tribo-positive to tribo-negative surface. This results the voltage and current rise in positive direction. In such condition, both the

surface shows same potential hence the voltage came to zero after certain time interval. As both the electrodes start separating to each other the same peak is observe in the negative directions. It is worth to notice that with increase in tapping rate, the open circuit voltage across the electrodes is same while the peak short circuit current increase from 1000 nA to 2000 nA. This suggest that the rate of charge increase with tapping rate due to more charge transfer at higher contact and separation process. Also, from fig. 7.18 (a) and (c) the number of peak upto 0.8 sec were increased that suggest the more numbers of time of contact and separations. However, it is worth to notice that the peak voltage in positive sides and negative side is not same. This is due to the charge affinity of tribo-positive and tribo-negative surfaces. In positive cycle, the charge is transfer from tribo-positive to tribo-negative surfaces while in negative side, the tribo-negative is transferring the charge which is reversed to its nature of the electrode. Hence the peak voltage is less in negative cycle of the contact and separation modes. The improvement in the current was more dure to reduced charge recombination phenomena. The reduced charge combination phenomenon produces positive and negative charges on triboelectric surfaces when it comes into contact before being converted into electrical energy. At higher tapping rate charge recombination takes place with shorter time that leads to greater portion of charges may be properly gathered and added to the TENG's output.

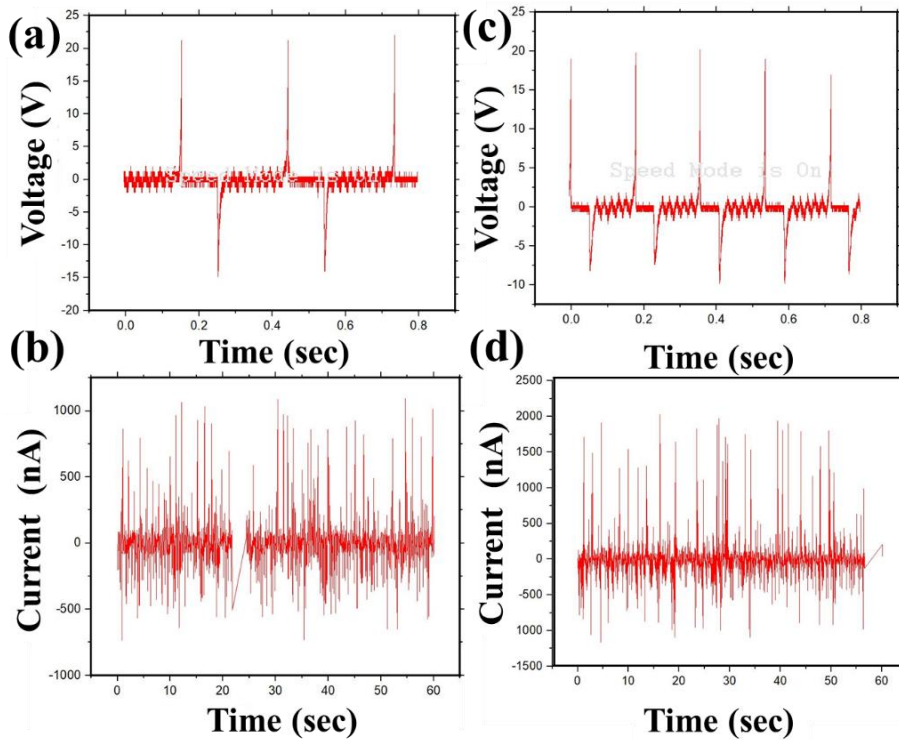


Fig. 7.19 Open circuit voltage and short circuit current at different tapping rate (a &b) 200 rpm, and (c & d) 350 rpm respectively.

The peak power is calculated by the multiplication of peak open circuit voltage and short circuit current and was observed that the as printed structures show the no change in peak power with increase in tapping rate as shown in fig. 7.19. However, after the ZnO nanostructure growth the peak power has higher peak power harvested compare to as printed structures. This might be due to the charges transfer through nanostructures shows high conductivity as compared to thin film hence the performance is improving. The peak power was $42 \mu\text{W}$ and $62 \mu\text{W}$ at tapping rate 200 RPM and 350 RPM The peak power decrease with increase in tapping rate from 200 RPM to 250 RPM and again start increasing beyond 250 RPM. The decrease in peak power was due to the increase in contact and separation between the electrode at 250 RPM.

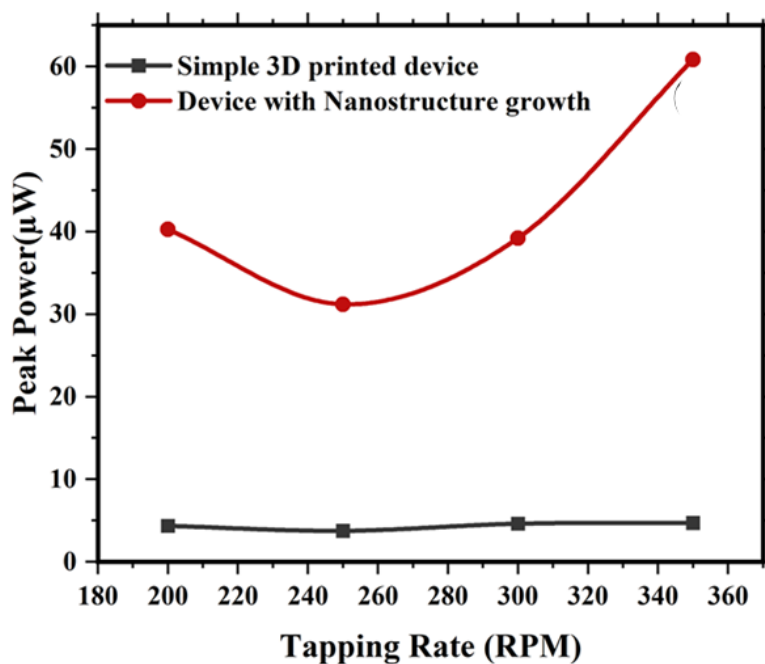


Fig. 7.20 Total peak Power developed at various tapping rate.

With further increase in rate, the peak power increase due to increase in frequency of contact and separation of both the electrodes. Moreover, at higher RPM, the number of current and voltage peaks were increased and gives less time of contact and separation between electrodes. Since the electrode potential is same but the time of charge transfer were decreased that leads to high rate of charge transfer from one substrate to another substrates. Hence, the current generated were increasing at constant voltage output.

7.4 Summary

The Laser μ -3D printing is deployed to show its capabilities towards different forms of material transfer such as NiTi metal thin film, ZnO nanostructures, and ZnO thin film for various sensing applications in MEMS devices.

- **NiTi Strain gauges**

The NiTi is printed using pixels by pixel and layer by layer fashion for the fabrication of three-dimensional strain gauge on flexible PET sheet. The strain gauge shows electro-mechanical response in terms of the strain and resistance of the printed structure. The resistance of the three-layer and five layers printed strain gauge were $220 \pm 10 \text{ k}\Omega$ and $88 \pm 8 \text{ k}\Omega$ printed structure were strained on UTM and resistance change were recorded. It was observed that the stress and resistance shows similar behaviour with increasing strain % in both three layer and five layered strain gauges. Moreover, the sensitivity of the strain sensor was defined by the gauge factor of printed strain gauge and observed that it is increasing with respect to number of layers printed due to more contact of metal thin film that leads to more conductivity and response of the sensors. While the sensitivity exhibits linear fit with more than 1% strain rate, the resistance exhibits linear fit with strain percentage. NiTi demonstrated significant reversible strain due to its extreme elasticity, which raises the printed strain gauge's strain percentage.

To measure the three-dimensional strain, a seven-layer rosette strain gauge were printed on same flexible substrate. It was observed that the position of the strain sensors shows different change in resistance of the sensor. The maximum change were observed in longitudinal direction and line parallel to the loading condition. Moreover, the sensitivity of the gauge was more at lower strain rate.

- **ZnO nanostructure for UV LED applications**

Most of the sensors were fabricated by nanostructures which show better functionality compared to thin film. Hence Laser μ -3D printing were

deployed to transfer the ZnO nanostructures selectively for sensing applications. For the processing of ZnO nanostructures, long laser pulse may distort the geometrical features hence a short laser pulse was used in this case. Due to its complexity, the laser parameters (laser wavelength and laser fluences) were estimated using numerical simulations and μ -3D printing was performed at that parameter.

It was observed that the laser fluence at 550 mJ/cm^2 starts melting the ZnO nanostructures in numerical as well as experimental results. However, at laser fluence 250 mJ/cm^2 , the transferred nanostructures show some distortion on the acceptor substrate while at 100 mJ/cm^2 , the intact nanostructures were transferred on the acceptor substrate. Moreover it was also observed that there was no phase change before and after the printing of ZnO nanostructure hence retain the properties of the parent materials. The functionality of the nanostructures was studied using the photoluminescence spectrum and observed that due to the defect were reduced after the printing mechanism. This might be due to the 355 nm excites the near band emission of ZnO. Thus, the intensity of near band emission near 370 nm increases after the printing process which improves the performance of UV-LED for opto-mechatronics applications.

- **Triboelectric nanogenerator**

The laser μ -3D printing was deployed for printing of ZnO thin layer deposition in line patterns followed by hydrothermal growth of nanostructure to improve the performance of triboelectric nanogenerators. The ZnO nanostructure were used as tribo-negative electrode while the copper coted FEP were used as tribo-positive electrode. The TENG device was fabricated with contact and separation mode and continuous tapping was performed with tapping rate of 200 RPM to 350 RPM. It was observed that the peak to peak voltage has less influence on the tapping rate while the short circuit current was improve from 1000 nA to 2000 nA in case of 200 RPM and 300 RPM respectively due to high rate to charge transfer in less time duration. Moreover, the peak power was calculated and observed that the as printed structure shows insignificant variation in the peak

power with tapping rate while after hydrothermal growth the performance was improved from 42 μ W to 62 μ W.

Chapter 8

Conclusion and Scope for Future Work

8.1 Conclusion

To retain the functionality and chemical composition, the PDMS sacrificial layer was used to absorb the laser energy and prints the material without phase change. The following conclusions are drawn from the mentioned objectives in chapter 1:

Objective 1: Demonstration of thin film-based μ -3D printing.

The laser decal transfer-based laser μ -3D printing setup was developed by integration of long pulsed CO₂ laser for the processing for electronics devices. The material was printed in same phase from donor substrate without altering the functionality and structural change. The developed setup is used for the fabrication of thin film-based sensors for micro-electro-mechanical systems. The following are the specifications of the developed setup

- The laser decal transfer based μ -3D printing is developed with the build volume of $80 \times 80 \times 80 \text{ mm}^3$ using long pulsed carbon dioxide laser source (wavelength - $10.6 \text{ }\mu\text{m}$) with lateral resolution of 2 micron for micro scale three-dimensional structure.
- A long-pulsed CO₂ laser system is employed for printing thin metal films avoid structural and functional alteration during printing.
- The developed setup has three degrees of freedom of acceptor stage while the two degrees of freedom for donor stage with substrate heating capability up to $300 \text{ }^\circ\text{C}$ having a 10-micron minimum resolution. As the laser pulse irradiates the donor substrate, a donor pixel ejects and deposited on the acceptor substrate. The donor stage displaced the donor substrate with 1.5 times of spot diameter for the complete spot transfer.
- The acceptor stage follows the CAD model geometry based on the CNC code with some spot overlap for continuous printing of the structures.

Objective 2: To investigate the influence of process parameters on the features size & resolution

This objective is investigated by performing parametric investigation of process parameter on the printed features size without phase change. The laser μ -3D printing was performed for printing thin film pixels in pixel by pixel and layer-by-layer fashion for the fabrication of micro scale three-dimensional structures. The process parameter involves, laser fluence, sacrificial layer thickness, spot overlap percentage, and substrate temperature.

The most important variable is laser fluence, which controls the pressure force for material to be ejected from donor substrate. It controls the induced pressure for the transfer mechanism and the printing feature size with high resolutions. Low laser fluence results in inadequate thrust force across the donor thin film for the transfer mechanism, but high fluence produces a wider track width because more gas is expanded during vaporisation. The adhesion of the particle on acceptor substrate can be improved by preheating the acceptor substrate before the printing that improved the adhesive force between the particle and substrate molecules.

- The continuity of the printed structures can be maintained by using proper spot overlap on the acceptor substrate.
- The sacrificial layer thickness should be more than the optical absorption length to absorb maximum amount of laser energy and induce necessary thrust force for transfer. However sacrificial layer thickness increases the threshold limit of laser fluence for pixel ejection in solid phase.

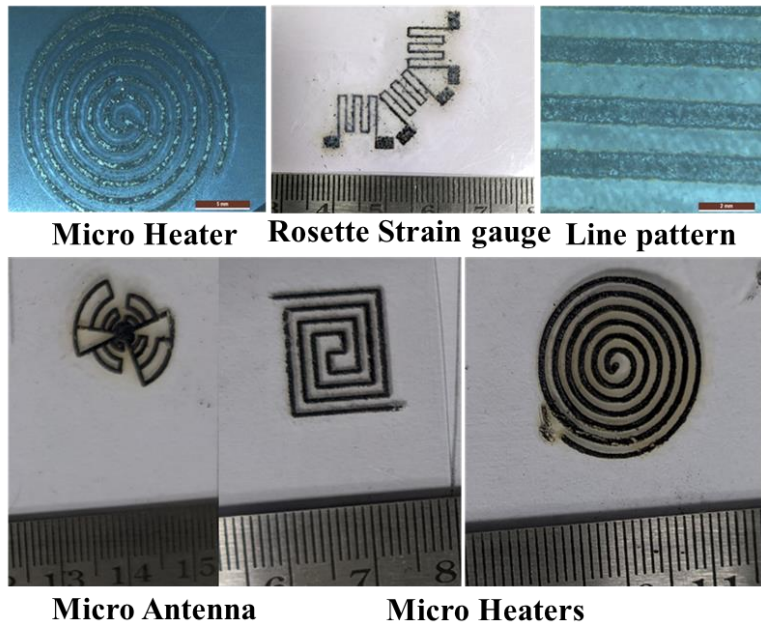


Fig. 8.1 Laser μ -3D printed metal microdevices for MEMS application

Objective 3: To analyse the mode of ejection using long pulsed laser with sacrificial layer.

The donor substrate was traced by high-speed camera using time-resolved shadowgraph technique. The laser beam absorbs in the sacrificial layer and form high pressurized plume beneath of donor film. The following conclusions are drawn from time resolved shadowgraph technique:

- The high-pressure gas, the vaporised gas seeks to expand and increases the size of plume and it reflects in the features of the printed structures.
- The angular deviation of particles just after the ejection from the laser beam (θ) defines the mode of transfer of DRL-based micro 3D printing and relates the printed features size. If the angular deviation $\theta < 5^\circ$ known as cap regime, $5 > \theta > 30^\circ$ debris regime and $\theta > 30^\circ$ Bursting mode.
- The thickness of the printed features is more in the cap regime while the bursting mode exhibits less thickness and more spattering of transferred particles in the form of debris.

- The time-resolved image shows that the ejection mode in DRL-based micro 3D printing is a combination of ejection of LIFT of thin film with melting and high viscous liquid. The plume formation caused by the sacrificial layer suggested a LIFT of a high-density liquid regime, whereas the cap regime suggested a LIFT of a thin film with melting.

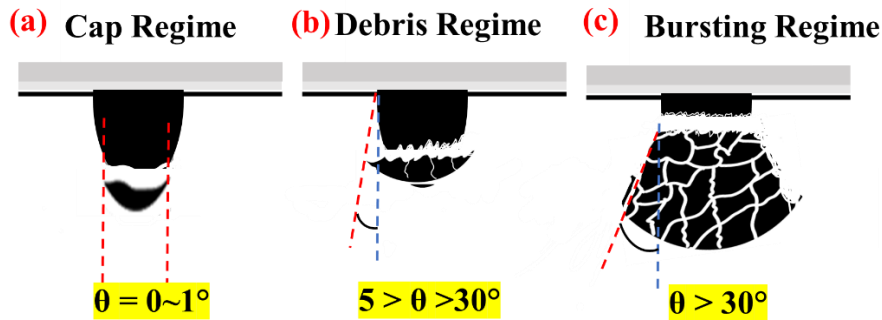


Fig. 8.2 Different mode of ejection with long pulsed laser system

Objective 4: Laser μ -3D printing capability towards functionalities and its behaviour.

Laser μ -3D printing was deployed for the printing of NiTi metal, ZnO thin film and ZnO nanostructures for the fabrication of functional devices for mems structures. The multi-layered NiTi material was printed in pixel-by-pixel and layer-by-layer fashion for the fabrication of a three-dimensional strain gauge on the flexible PET sheet. The printed structures show electromechanical response in terms of resistance with strain percentage. It was concluded that the sensitivity of the printed structure shows dependency on several printed layers due to more amount of NiTi pixels involved in the strain sensing. Similarly for three-dimensional strain measurement, the rosette strain gauge was printed and observed that the gauge parallel to the loading condition shows maximum response due high component of strain in that direction.

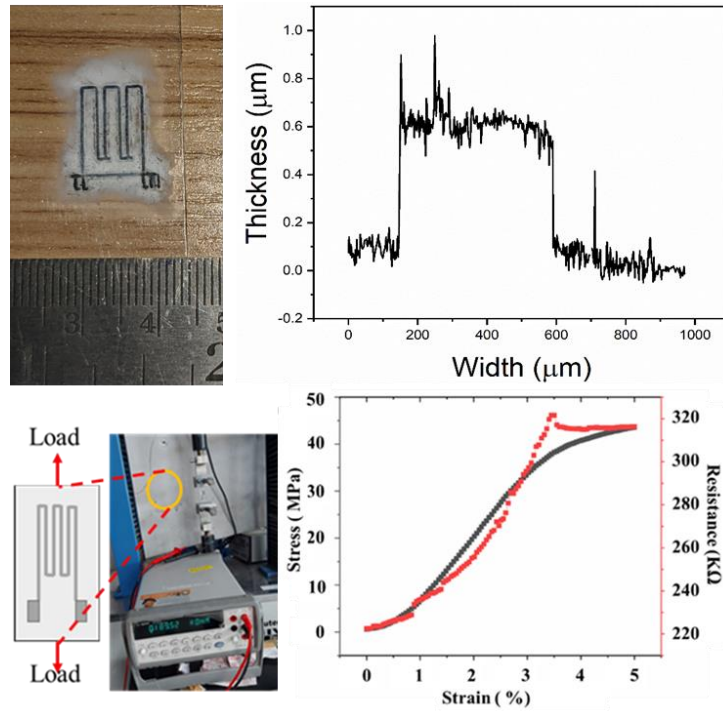


Fig. 8.3 laser μ -3D printed strain gauge and its performance

To retain the functionality of ZnO nanostructure, a short pulse laser was deployed for the printing of the nanostructure on the PET sheet for UV-LED applications. The numerical simulation shows that the higher fluence at 550 mJ/cm^2 reaches beyond the melting point of ZnO and the same was observed during the experiment. The printed morphology was melted, and nanostructure was not observed on the acceptor substrate. It was concluded that at 100 mJ/cm^2 , the bundles of nanostructures were printed, and no secondary phases were observed before and after the printing process. Moreover, the functionality of printed nanostructure was improved close to near band emission due to excitation by 355 nm laser wavelength.

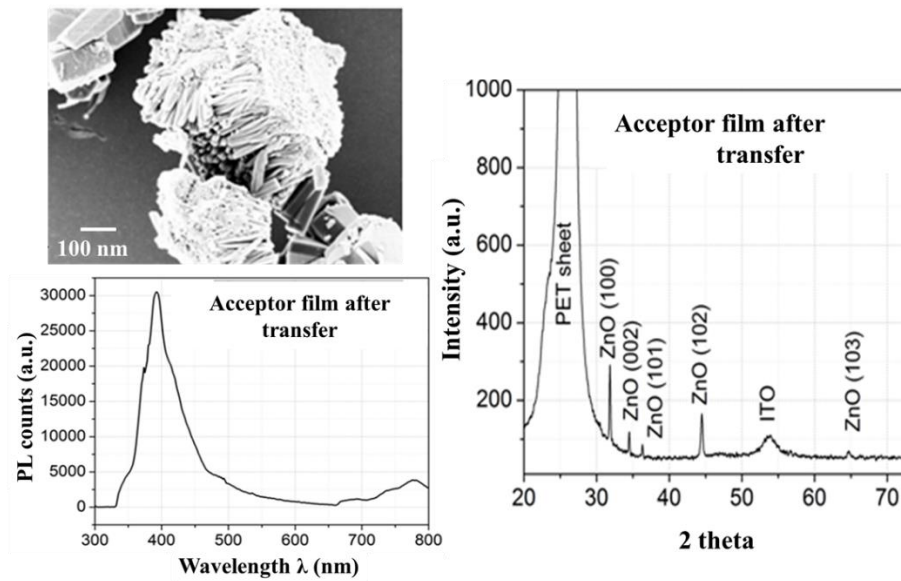


Fig. 8.4 Selective deposition of ZnO nanostructure for UV-LED application

At last, a triboelectric nanogenerator was fabricated to harvest vibration energy into electrical energy. The ZnO line pattern was printed using Laser μ -3D printing followed by a hydrothermal process for the fabrication of contact and separation mode triboelectric nanogenerator. ZnO nanostructure was used as tribo-negative surface while the copper-coated FEP were used as tribo-positive surface. The contact and separation were performed at different tapping rates and it was concluded that the tapping rate has less influence on the open circuit voltage (18-20 V) while influence was more in short circuit current (1000nA to 2000 nA). The peak power was harvested from 42 μ W to 62 μ W at tapping rates of 200 and 350 RPM respectively.

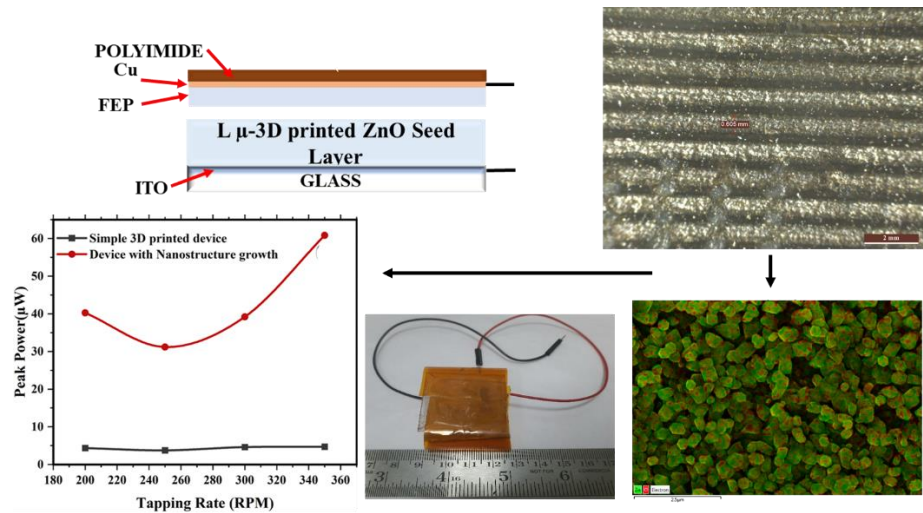


Fig. 8.5 Laser μ-3D printed ZnO based triboelectric nanogenerator

The above results show that Laser μ-3D printing is an effective microfabrication process for smart sensor and device fabrication in micro-electro-mechanical systems.

8.2 Future Scope

The current study focused on the printing of a micron scale structure with single material while most MEMS device requires multi-materials for the distinct functionalities to enhance the performance. Moreover, the MEMS devices are having complex curved surfaces and overhang members in their structures which should be considered using a thin film-based micro 3D printing process. Chapter 6 shows the material ejection from the donor substrate after the laser absorption but the mechanics of material printing on the acceptor substrate should be considered for better understanding of the process.

The below-mentioned suggestion can be the future work:

1. Investigation of multi-material deposition by laser μ-3D printing
2. Investigation of the overhang structure for curved surfaces.
3. Investigation of mechanics and dynamics of particle during landing on the acceptor substrate.
4. Large area printing to increase the production rate.

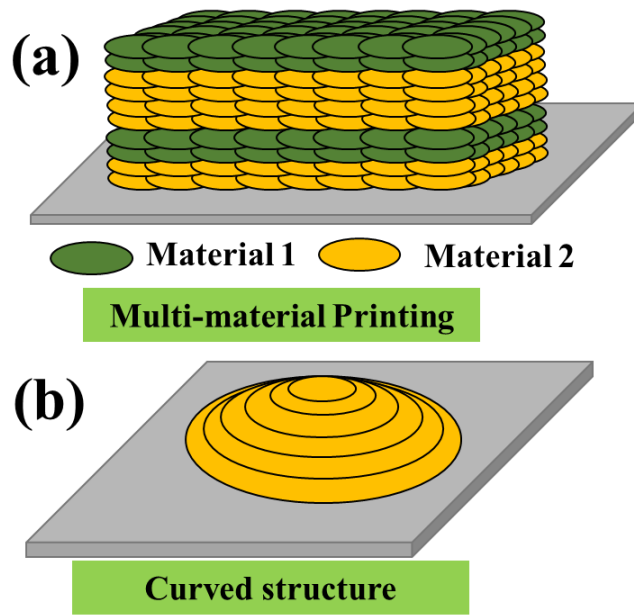


Fig. 8.6 Multi-material Printing using Laser μ -3D printing, and (b) Overhand curved structure.

References

- [1] N.-T. Nguyen, In *Micro and Nano Technologies*, in: *Micromixers, Micromixer*, William Andrew Publishing, 2012: pp. 113–161. <https://doi.org/10.1016/b978-1-4377-3520-8.00004-8>.
- [2] M. Li, W.H. Li, J. Zhang, G. Alici, W. Wen, A review of microfabrication techniques and dielectrophoretic microdevices for particle manipulation and separation, *J. Phys. D. Appl. Phys.* 47 (2014). <https://doi.org/10.1088/0022-3727/47/6/063001>.
- [3] N. Zhang, W. Sun, S.P. Rodrigues, K. Wang, Z. Gu, S. Wang, W. Cai, S. Xiao, Q. Song, Highly Reproducible Organometallic Halide Perovskite Microdevices based on Top-Down Lithography, *Adv. Mater.* 29 (2017). <https://doi.org/10.1002/adma.201606205>.
- [4] T. Blachowicz, A. Ehrmann, 3D printed MEMS technology-recent developments and applications, *Micromachines.* 11 (2020) 1–14. <https://doi.org/10.3390/MI11040434>.
- [5] J. Huang, Q. Qin, J. Wang, A review of stereolithography: Processes and systems, *Processes.* 8 (2020). <https://doi.org/10.3390/PR8091138>.
- [6] A. Piqué, Laser-Based Micro-Additive Manufacturing Technologies, in: *Three-Dimensional Microfabr. Using Two-Phot. Polym.*, Elsevier Inc., 2016: pp. 1–19. <https://doi.org/10.1016/B978-0-323-35321-2.00001-7>.
- [7] M. Vaezi, H. Seitz, S. Yang, A review on 3D micro-additive manufacturing technologies, *Int. J. Adv. Manuf. Technol.* 67 (2013) 1721–1754. <https://doi.org/10.1007/s00170-012-4605-2>.
- [8] A.C. Fischer, M. Mäntysalo, F. Niklaus, Inkjet Printing, Laser-Based Micromachining and Micro 3D Printing Technologies for

- MEMS, Elsevier Inc., 2015. <https://doi.org/10.1016/B978-0-323-29965-7.00026-9>.
- [9] L. Qi, J. Luo, H. Shen, H. Lian, *Metal Micro-Droplet Based 3D Printing Technology*, 1st ed., Springer Singapore, 2023. <https://doi.org/10.1007/978-981-99-0965-0>.
- [10] P. Sood, S. Jayachandran, P. Rajagopalan, K. Akash, V. Singh, I.A. Palani, Parametric investigations on developing copper micropatterns on flexible film using solid state nd:yag 532nm laser induced forward transfer, *Mater. Today Proc.* 5 (2018) 8612–8617. <https://doi.org/10.1016/j.matpr.2017.11.559>.
- [11] V.P. Veiko, E.A. Shakhno, V.M. Smirnov, A.M. Miaskovski, G.D. Nikishin, Laser-induced film deposition by LIFT: Physical mechanisms and applications, *Laser Part. Beams.* 24 (2006) 203–209. <https://doi.org/10.1017/S0263034606060289>.
- [12] V. Schultze, M. Wagner, Laser-induced forward transfer of aluminium, *Appl. Surf. Sci.* 52 (1991) 303–309. [https://doi.org/10.1016/0169-4332\(91\)90072-R](https://doi.org/10.1016/0169-4332(91)90072-R).
- [13] V. Sametoglu, V. Sauer, Y.Y. Tsui, Nanoscale laser-induced forward transfer through patterned Cr films, *Appl. Phys. A Mater. Sci. Process.* 110 (2013) 823–827. <https://doi.org/10.1007/s00339-012-7159-0>.
- [14] I. Zergioti, S. Mailis, N.A. Vainos, P. Papakonstantinou, C. Kalpouzos, C.P. Grigoropoulos, C. Fotakis, Microdeposition of metal and oxide structures using ultrashort laser pulses, *Appl. Phys. A Mater. Sci. Process.* 66 (1998) 579–582. <https://doi.org/10.1007/s003390050717>.
- [15] A. James, A. Greer, E. Thomas, Laser -induced forward transfer of metal oxides to trim the frequency of surface acoustic wave resonator devices, in: *Excimer Beam Appl.*, 1988: pp. 113–125.
- [16] J.A. Barron, P. Wu, H.D. Ladouceur, B.R. Ringeisen, *Biological*

- laser printing: A novel technique for creating heterogeneous 3-dimensional cell patterns, *Biomed. Microdevices*. 6 (2004) 139–147. <https://doi.org/10.1023/B:BMMD.0000031751.67267.9f>.
- [17] M. Colina, P. Serra, J.M. Fern, L. Sevilla, J.L. Morenza, DNA deposition through laser induced forward transfer, *Biosens. Bioelectron*. 20 (2005) 1638–1642. <https://doi.org/10.1016/j.bios.2004.08.047>.
- [18] L. Rapp, C. Constantinescu, Y. Larmande, A.P. Alloncle, P. Delaporte, Smart beam shaping for the deposition of solid polymeric material by laser forward transfer, *Appl. Phys. A Mater. Sci. Process*. 117 (2014) 333–339. <https://doi.org/10.1007/s00339-014-8305-7>.
- [19] J. Shaw Stewart, T. Lippert, M. Nagel, F. Nüesch, A. Wokaun, Red-green-blue polymer light-emitting diode pixels printed by optimized laser-induced forward transfer, *Appl. Phys. Lett*. 100 (2012). <https://doi.org/10.1063/1.4717463>.
- [20] C. Boutopoulos, V. Tsouti, D. Goustouridis, S. Chatzandroulis, I. Zergioti, Liquid phase direct laser printing of polymers for chemical sensing applications, *Appl. Phys. Lett*. 93 (2008) 24–27. <https://doi.org/10.1063/1.3025596>.
- [21] K.S. Kaur, R. Fardel, T.C. May-Smith, M. Nagel, D.P. Banks, C. Grivas, T. Lippert, R.W. Eason, Shadowgraphic studies of triazene assisted laser-induced forward transfer of ceramic thin films, *J. Appl. Phys*. 105 (2009) 113119. <https://doi.org/10.1063/1.3132822>.
- [22] A. Sahu, I.A. Palani, V. Singh, Parametric investigations on laser-induced forward transfer based micro-3D printing of NiTi alloy, *Mater. Manuf. Process*. 37 (2022) 1310–1319. <https://doi.org/10.1080/10426914.2022.2072877>.
- [23] J. Luo, R. Pohl, L. Qi, G.W. Römer, C. Sun, D. Lohse, C.W.

- Visser, Printing Functional 3D Microdevices by Laser-Induced Forward Transfer, *Small*. 13 (2017) 1–5.
<https://doi.org/10.1002/sml.201602553>.
- [24] O. Fogel, S.S. Cohen, Z. Kotler, Z. Zalevsky, Mechanical properties of 3D metallic microstructures printed by laser induced forward transfer, in: 10th CIRP Conf. Photonic Technol., Elsevier B.V., 2018: pp. 285–289.
<https://doi.org/10.1016/j.procir.2018.08.112>.
- [25] C.W. Visser, R. Pohl, C. Sun, G.W. Römer, B. Huis In 't Veld, D. Lohse, Toward 3D Printing of Pure Metals by Laser-Induced Forward Transfer, *Adv. Mater.* 27 (2015) 4087–4092.
<https://doi.org/10.1002/adma.201501058>.
- [26] M.L. Levene, R.D. Scott, B.W. Stryj, Material Transfer Recording, *Appl. Opt.* 9 (1970) 2260–2265.
<https://doi.org/10.1364/ao.9.002260>.
- [27] J. Bohandy, B.F. Kim, F.J. Adrian, Metal deposition from a supported metal film using an excimer laser, *J. Appl. Phys.* 60 (1986) 1538–1539. <https://doi.org/10.1063/1.337287>.
- [28] J. Bohandy, B.F. Kim, F.J. Adrian, A.N. Jette, B.F. Kim, F.J. Adrian, A.N. Jette, Metal deposition at 532 nm using a laser transfer technique Metal deposition at 532 nm using a laser transfer technique, *J. Appl. Phys.* 63 (1988) 1158.
<https://doi.org/10.1063/1.340023>.
- [29] Chapter 13 - Laser-Induced Forward Transfer Techniques and Applications.pdf, (n.d.).
- [30] P. Serra, M. Duocastella, J.M. Fernández-Pradas, J.L. Morenza, The laser-induced forward transfer technique for microprinting, in: *Adv. Laser Mater. Process. Technol. Res. Appl.*, Woodhead Publishing Limited, Barcelona, Spain, 2010: pp. 367–393.
<https://doi.org/10.1533/9781845699819.5.367>.

- [31] M. Morales, D. Munoz-Martin, A. Marquez, S. Lauzurica, C. Molpeceres, Laser-Induced Forward Transfer Techniques and Applications, in: *Adv. Laser Mater. Process.*, Second Edi, Elsevier Ltd., 2018: pp. 339–379. <https://doi.org/10.1016/b978-0-08-101252-9.00013-3>.
- [32] Z. Kántor, Z. Tóth, T. Szörényi, Metal pattern deposition by laser-induced forward transfer, *Appl. Surf. Sci.* 86 (1995) 196–201. [https://doi.org/10.1016/0169-4332\(94\)00384-X](https://doi.org/10.1016/0169-4332(94)00384-X).
- [33] R.C.Y. Auyeung, H. Kim, N.A. Charipar, A.J. Birnbaum, S.A. Mathews, A. Piqué, Laser forward transfer based on a spatial light modulator, *Appl. Phys. A Mater. Sci. Process.* 102 (2011) 21–26. <https://doi.org/10.1007/s00339-010-6054-9>.
- [34] R.C.Y. Auyeung, H. Kim, S. Mathews, A. Piqué, Laser forward transfer using structured light, *Opt. Express.* 23 (2015) 422. <https://doi.org/10.1364/oe.23.000422>.
- [35] K.S. Kaur, M. Feinaeugle, D.P. Banks, J.Y. Ou, F. Di Pietrantonio, E. Verona, C.L. Sones, R.W. Eason, Laser-induced forward transfer of focussed ion beam pre-machined donors, *Appl. Surf. Sci.* 257 (2011) 6650–6653. <https://doi.org/10.1016/j.apsusc.2011.02.094>.
- [36] M. Colina, P. Serra, J.L. Morenza, Laser-induced forward transfer of biomolecules, *Thin Solid Films.* 454 (2004) 27–30. <https://doi.org/10.1016/j.tsf.2003.11.154>.
- [37] A. Sorkio, L. Koch, L. Koivusalo, A. Deiwick, S. Miettinen, B. Chichkov, H. Skottman, Human stem cell based corneal tissue mimicking structures using laser-assisted 3D bioprinting and functional bioinks, *Biomaterials.* 171 (2018) 57–71. <https://doi.org/10.1016/j.biomaterials.2018.04.034>.
- [38] S. Papazoglou, I. Zergioti, Laser Induced Forward Transfer (LIFT) of nano-micro patterns for sensor applications,

- Microelectron. Eng. 182 (2017) 25–34.
<https://doi.org/10.1016/j.mee.2017.08.003>.
- [39] H. Kim, R.C.Y. Auyeung, A. Piqué, Laser-printed thick-film electrodes for solid-state rechargeable Li-ion microbatteries, *J. Power Sources*. 165 (2007) 413–419.
<https://doi.org/10.1016/j.jpowsour.2006.11.053>.
- [40] T. Dixit, I.A. Palani, V. Singh, Insights into non-noble metal based nanophotonics: Exploration of Cr-coated ZnO nanorods for optoelectronic applications, *RSC Adv.* 8 (2018) 6820–6833.
<https://doi.org/10.1039/c7ra13174g>.
- [41] S. Fernandez-Robledo, J. Nekarda, A. Büchler, A laser induced forward transfer process for selective boron emitters, *Sol. Energy Mater. Sol. Cells*. 161 (2017) 397–406.
<https://doi.org/10.1016/j.solmat.2016.12.026>.
- [42] J. Shaw Stewart, T. Lippert, M. Nagel, F. Nüesch, A. Wokaun, Red-green-blue polymer light-emitting diode pixels printed by optimized laser-induced forward transfer, *Appl. Phys. Lett.* 100 (2012) 203303. <https://doi.org/10.1063/1.4717463>.
- [43] R. Fardel, M. Nagel, F. Nüesch, T. Lippert, A. Wokaun, Fabrication of organic light-emitting diode pixels by laser-assisted forward transfer, *Appl. Phys. Lett.* 91 (2007) 89–92.
<https://doi.org/10.1063/1.2759475>.
- [44] M. Duocastella, J.M. Fernández-Pradas, J.L. Morenza, D. Zafra, P. Serra, Novel laser printing technique for miniaturized biosensors preparation, *Sensors Actuators, B Chem.* 145 (2010) 596–600. <https://doi.org/10.1016/j.snb.2009.11.055>.
- [45] P. Serra, J.M. Fernández-pradas, M. Colina, M. Duocastella, Laser-induced forward Transfer : a Direct-writing Technique for Biosensors Preparation, *J. Laser Micro/Nanoengineering.* 1 (2006) 236–242. <https://doi.org/10.2961/jlmn.2006.03.0017>.

- [46] P. Serra, J.L. Morenza, M. Duocastella, M. Colina, J.M. Ferna, Study of the laser-induced forward transfer of liquids for laser bioprinting, *Appl. Surf. Sci.* 253 (2007) 7855–7859. <https://doi.org/10.1016/j.apsusc.2007.02.097>.
- [47] J.M. Fernández-Pradas, C. Florian, F. Caballero-Lucas, P. Sopeña, J.L. Morenza, P. Serra, Laser-induced forward transfer: Propelling liquids with light, *Appl. Surf. Sci.* 418 (2017) 559–564. <https://doi.org/10.1016/j.apsusc.2016.10.197>.
- [48] A. Kalaitzis, M. Makrygianni, I. Theodorakos, A. Hatziapostolou, S. Melamed, A. Kabla, F. de la Vega, I. Zergioti, Jetting dynamics of Newtonian and non-Newtonian fluids via laser-induced forward transfer: Experimental and simulation studies, *Appl. Surf. Sci.* 465 (2019) 136–142. <https://doi.org/10.1016/j.apsusc.2018.09.084>.
- [49] R. Fardel, M. Nagel, F. Nüesch, T. Lippert, A. Wokaun, Laser forward transfer using a sacrificial layer: Influence of the material properties, *Appl. Surf. Sci.* 254 (2007) 1322–1326. <https://doi.org/10.1016/j.apsusc.2007.08.091>.
- [50] D.P. Banks, K. Kaur, R. Gazia, R. Fardel, M. Nagel, T. Lippert, R.W. Eason, Triazene photopolymer dynamic release layer-assisted femtosecond laser-induced forward transfer with an active carrier substrate, *A Lett. J. Explor. Front. Phys.* 83 (2008) 38003. <https://doi.org/10.1209/0295-5075/83/38003>.
- [51] V. Dinca, R. Fardel, J. Shaw-Stewart, F. Di Pietrantonio, D. Cannatà, M. Benetti, E. Verona, A. Palla-Papavlu, M. Dinescu, T. Lippert, Laser-induced forward transfer: An approach to single-step polymer microsensor fabrication, *Sens. Lett.* 8 (2010) 436–440. <https://doi.org/10.1166/sl.2010.1291>.
- [52] A. Palla-Papavlu, V. Dinca, I. Paraico, A. Moldovan, J. Shaw-Stewart, C.W. Schneider, E. Kovacs, T. Lippert, M. Dinescu, Microfabrication of polystyrene microbead arrays by laser

- induced forward transfer, *J. Appl. Phys.* 108 (2010) 1–7.
<https://doi.org/10.1063/1.3466746>.
- [53] H. Search, C. Journals, A. Contact, M. Iopscience, I.P. Address, Triazene photopolymer dynamic release layer-assisted femtosecond laser-induced forward transfer with an active carrier substrate, *A Lett. J. Explor. Front. Phys.* 38003 (2008).
<https://doi.org/10.1209/0295-5075/83/38003>.
- [54] R. Fardel, M. Nagel, F. Nu, T. Lippert, Laser-Induced Forward Transfer of Organic LED Building Blocks Studied by Time-Resolved Shadowgraphy, *J. Phys. Chem. C.* 114 (2010) 5617–5636.
- [55] P. Delaporte, A.P. Alloncle, Laser-induced forward transfer: A high resolution additive manufacturing technology, *Opt. Laser Technol.* 78 (2016) 33–41.
<https://doi.org/10.1016/j.optlastec.2015.09.022>.
- [56] J. Shaw-stewart, R. Fardel, L. Rapp, The effect of laser pulse length upon laser-induced forward transfer using a triazene polymer as a dynamic release layer, *J. Optoelectron. Adv. Mater.* 12 (2010) 605–609.
- [57] S. Chen, I.Y.S. Lee, W.A. Tolbert, X. Wen, D.D. Dlott, Applications of ultrafast temperature jump spectroscopy to condensed phase molecular dynamics, *J. Phys. Chem.* 96 (1992) 7178–7186. <https://doi.org/10.1021/j100197a012>.
- [58] D. Young, R.C.Y. Auyeung, A. Piqué, D.B. Chrisey, D.D. Dlott, Time-resolved optical microscopy of a laser-based forward transfer process, *Appl. Phys. Lett.* 78 (2001) 3169.
<https://doi.org/10.1063/1.1372200>.
- [59] and P.S. M. Duocastella, J. M. Fernández-Pradas, J. L. Morenza, Time-resolved imaging of the laser forward transfer of liquids, *J. Appl. Phys.* 106 (2009) 084907.

<https://doi.org/10.1063/1.3248304>.

- [60] D. Tsakona, I. Theodorakos, A. Kalaitzis, I. Zergioti, Investigation on high speed laser printing of silver nanoparticle inks on flexible substrates, *Appl. Surf. Sci.* 513 (2020) 145912. <https://doi.org/10.1016/j.apsusc.2020.145912>.
- [61] M. Duocastella, J.M. Fernández-Pradas, P. Serra, J.L. Morenza, Jet formation in the laser forward transfer of liquids, *Appl. Phys. A Mater. Sci. Process.* 93 (2008) 453–456. <https://doi.org/10.1007/s00339-008-4781-y>.
- [62] M. Duocastella, J.M. Fernández-Pradas, J.L. Morenza, P. Serra, Sessile droplet formation in the laser-induced forward transfer of liquids: A time-resolved imaging study, *Thin Solid Films.* 518 (2010) 5321–5325. <https://doi.org/10.1016/j.tsf.2010.03.082>.
- [63] M. Duocastella, A. Patrascioiu, V. Dinca, J.M. Fernández-Pradas, J.L. Morenza, P. Serra, Study of liquid deposition during laser printing of liquids, *Appl. Surf. Sci.* 257 (2011) 5255–5258. <https://doi.org/10.1016/j.apsusc.2010.10.148>.
- [64] M. Duocastella, A. Patrascioiu, J.M. Fernández-Pradas, J.L. Morenza, P. Serra, On the correlation between droplet volume and irradiation conditions in the laser forward transfer of liquids, *Appl. Phys. A Mater. Sci. Process.* 109 (2012) 5–14. <https://doi.org/10.1007/s00339-012-7047-7>.
- [65] J. Mikšys, G. Arutinov, G.R.B.E. Römer, Pico- to nanosecond pulsed laser-induced forward transfer (LIFT) of silver nanoparticle inks: a comparative study, *Appl. Phys. A.* 125 (2019) 814. <https://doi.org/10.1007/s00339-019-3085-8>.
- [66] C. Germain, L. Charron, L. Lilge, Y.Y. Tsui, Electrodes for microfluidic devices produced by laser induced forward transfer, *Appl. Surf. Sci.* 253 (2007) 8328–8333.

<https://doi.org/10.1016/j.apsusc.2007.02.158>.

- [67] O. Fogel, S. Winter, E. Benjamin, S. Krylov, Z. Kotler, Z. Zalevsky, 3D printing of functional metallic microstructures and its implementation in electrothermal actuators, *Addit. Manuf.* 21 (2018) 307–311. <https://doi.org/10.1016/j.addma.2018.03.018>.
- [68] M. Feinaeugle, R. Pohl, T. Bor, T. Vaneker, G. willem Römer, Printing of complex free-standing microstructures via laser-induced forward transfer (LIFT) of pure metal thin films, *Addit. Manuf.* 24 (2018) 391–399. <https://doi.org/10.1016/j.addma.2018.09.028>.
- [69] N. Gorodesky, S. Sedghani-Cohen, M. Altman, O. Fogel, G. Cohen-Taguri, Y. Fleger, Z. Kotler, Z. Zalevsky, Concurrent Formation of Metallic Glass During Laser Forward Transfer 3D Printing, *Adv. Funct. Mater.* 30 (2020) 1–6. <https://doi.org/10.1002/adfm.202001260>.
- [70] M. Zenou, A. Sa'ar, Z. Kotler, Laser jetting of femto-liter metal droplets for high resolution 3D printed structures, *Sci. Rep.* 5 (2015) 17265. <https://doi.org/10.1038/srep17265>.
- [71] A. You, M.A.Y. Be, I. In, Preparation of functional DNA microarrays through laser-induced forward transfer, *Appl. Phys. Lett.* 85 (2004) 1639–1641. <https://doi.org/10.1063/1.1787614>.
- [72] L. Koch, S. Kuhn, H. Sorg, M. Gruene, S. Schlie, R. Gaebel, B. Polchow, K. Reimers, S. Stoelting, N. Ma, P.M. Vogt, G. Steinhoff, B. Chichkov, Laser printing of skin cells and human stem cells, *Tissue Eng. - Part C Methods.* 16 (2010) 847–854. <https://doi.org/10.1089/ten.tec.2009.0397>.
- [73] L. Koch, A. Deiwick, S. Schlie, S. Michael, M. Gruene, V. Coger, D. Zychlinski, A. Schambach, K. Reimers, P.M. Vogt, B. Chichkov, Skin tissue generation by laser cell printing, *Biotechnol. Bioeng.* 109 (2012) 1855–1863.

<https://doi.org/10.1002/bit.24455>.

- [74] B. Hopp, T. Smausz, N. Kresz, N. Barna, Z. Bor, L. Kolozsvári, D.B. Chrisey, A. Szabó, A. Nógrádi, Survival and proliferative ability of various living cell types after laser-induced forward transfer, *Tissue Eng.* 11 (2005) 1817–1823.
<https://doi.org/10.1089/ten.2005.11.1817>.
- [75] H. Selvaraj Bachelor, A NEW APPROACH TO FABRICATE PDMS STRUCTURES USING FEMTOSECOND LASER, 2013. <https://doi.org/10.32920/ryerson.14644545.v1> (accessed January 3, 2022).
- [76] G. Luo, D. Wu, Y. Zhou, Y. Hu, Z. Yao, Elucidating ejection regimes of metal microdroplets in voxel-based laser-induced forward transfer, *Addit. Manuf.* 55 (2022).
<https://doi.org/10.1016/j.addma.2022.102814>.
- [77] P.K. Kumar, D.C. Lagoudas, Introduction to Shape Memory Alloys, in: Dimitris C. Lagoudas (Ed.), *Shape Mem. Alloy.*, Springer US, 2008: pp. 1–51. <https://doi.org/10.1007/978-0-387-47685-8>.
- [78] C. Bechtold, R.L. de Miranda, C. Chluba, E. Quandt, Fabrication of self-expandable NiTi thin film devices with micro-electrode array for bioelectric sensing, stimulation and ablation, *Biomed. Microdevices.* 18 (2016).
<https://doi.org/10.1007/s10544-016-0131-6>.
- [79] T. Habijan, R.L. De Miranda, C. Zamponi, E. Quandt, C. Greulich, T.A. Schildhauer, M. Köller, The biocompatibility and mechanical properties of cylindrical NiTi thin films produced by magnetron sputtering, *Mater. Sci. Eng. C.* 32 (2012) 2523–2528.
<https://doi.org/10.1016/j.msec.2012.07.035>.
- [80] D.P. Banks, K.S. Kaur, R.W. Eason, Etching and forward transfer of fused silica in solid-phase by femtosecond laser-

- induced solid etching (LISE), *Appl. Surf. Sci.* 255 (2009) 8343–8351. <https://doi.org/10.1016/j.apsusc.2009.05.060>.
- [81] M. Kumar, R. Mitra, Effect of substrate temperature and annealing on structure, stress and properties of reactively co-sputtered Ni-TiN nanocomposite thin films, *Thin Solid Films*. 624 (2017) 70–82. <https://doi.org/10.1016/j.tsf.2017.01.024>.
- [82] R.S.C. Paredes, S.C. Amico, A.S.C.M. d'Oliveira, The effect of roughness and pre-heating of the substrate on the morphology of aluminium coatings deposited by thermal spraying, *Surf. Coatings Technol.* 200 (2006) 3049–3055. <https://doi.org/10.1016/j.surfcoat.2005.02.200>.
- [83] Q. Li, D. Grojo, A.P. Alloncle, P. Delaporte, Dynamics of double-pulse laser printing of copper microstructures, *Appl. Surf. Sci.* 471 (2019) 627–632. <https://doi.org/10.1016/j.apsusc.2018.12.052>.
- [84] M. Sole-Gras, R. Xiong, C. Liang, W. Roorda, H. Yamaguchi, Y. Huang, Study of Overlapping Adjacent Jets for Effective Laser-Induced Forward Transfer Printing, *J. Manuf. Sci. Eng. Trans. ASME*. 143 (2021) 1–13. <https://doi.org/10.1115/1.4048440>.
- [85] D. Munoz-martin, Y. Chen, M. Morales, C. Molpeceres, Overlapping limitations for ps-pulsed lift printing of high viscosity metallic pastes, *Metals (Basel)*. 10 (2020). <https://doi.org/10.3390/met10020168>.
- [86] A.K. Bose, X. Zhang, D. Maddipatla, S. Masihi, M. Panahi, B.B. Narakathu, B.J. Bazuin, J.D. Williams, M.F. Mitchell, M.Z. Atashbar, Screen-printed strain gauge for micro-strain detection applications, in: *IEEE Sens. J.*, Institute of Electrical and Electronics Engineers Inc., 2020: pp. 12652–12660. <https://doi.org/10.1109/JSEN.2020.3002388>.

- [87] M. Shakeel, W.A. Khan, K. Rahman, Fabrication of cost effective and high sensitivity resistive strain gauge using DIW technique, *Sensors Actuators, A Phys.* 258 (2017) 123–130. <https://doi.org/10.1016/j.sna.2017.03.003>.
- [88] P.S. Zieliński, P.K.R. Gudeti, T. Rikmanspoel, M.K. Włodarczyk-Biegun, 3D printing of bio-instructive materials: Toward directing the cell, *Bioact. Mater.* 19 (2023) 292–327. <https://doi.org/10.1016/j.bioactmat.2022.04.008>.
- [89] G. Caminoa, S.M. Lomakin, M. Lazzari, Polydimethylsiloxane thermal degradation. Part 1. Kinetic aspects., *Polymer (Guildf)*. 42 (2001) 2395–2402.
- [90] D. Munoz-martin, C.F. Brasz, Y. Chen, M. Morales, C.B. Arnold, C. Molpeceres, *Applied Surface Science* Laser-induced forward transfer of high-viscosity silver pastes, *Appl. Surf. Sci.* 366 (2016) 389–396. <https://doi.org/10.1016/j.apsusc.2016.01.029>.
- [91] A. Patrascioiu, J.M. Fernández-Pradas, A. Palla-Papavlu, J.L. Morenza, P. Serra, Laser-generated liquid microjets: Correlation between bubble dynamics and liquid ejection, *Microfluid. Nanofluidics*. 16 (2014) 55–63. <https://doi.org/10.1007/s10404-013-1218-5>.
- [92] M. Feinaeugle, A.P. Alloncle, P. Delaporte, C.L. Sones, R.W. Eason, Time-resolved shadowgraph imaging of femtosecond laser-induced forward transfer of solid materials, *Appl. Surf. Sci.* 258 (2012) 8475–8483. <https://doi.org/10.1016/j.apsusc.2012.04.101>.
- [93] R. Pohl, C.W. Visser, G. Römer, D. Lohse, C. Sun, B. Huis, Ejection Regimes in Picosecond Laser-Induced Forward Transfer of Metals, *PHYS. REV. Appl.* 3. 3 (2015) 024001. <https://doi.org/10.1103/PhysRevApplied.3.024001>.

- [94] Fabrication of Strain Gauges via Contact Printing_ A Simple Route to Healthcare Sensors Based on Cross-Linked Gold Nanoparticles _ Enhanced Reader, *Appl. Mater. Interfaces*. 10 (2018) 37374–37385.
- [95] X. Ho, C.K. Cheng, J.N. Tey, J. Wei, Tunable strain gauges based on two-dimensional silver nanowire networks, *Nanotechnology*. 26 (2015). <https://doi.org/10.1088/0957-4484/26/19/195504>.
- [96] M. Hempel, D. Nezich, J. Kong, M. Hofmann, A novel class of strain gauges based on layered percolative films of 2D materials, *Nano Lett.* 12 (2012) 5714–5718. <https://doi.org/10.1021/nl302959a>.
- [97] N. Lu, C. Lu, S. Yang, J. Rogers, Highly sensitive skin-mountable strain gauges based entirely on elastomers, *Adv. Funct. Mater.* 22 (2012) 4044–4050. <https://doi.org/10.1002/adfm.201200498>.
- [98] Y. Zhang, N. Anderson, S. Bland, S. Nutt, G. Jursich, S. Joshi, All-printed strain sensors: Building blocks of the aircraft structural health monitoring system, *Sensors Actuators, A Phys.* 253 (2017) 165–172. <https://doi.org/10.1016/j.sna.2016.10.007>.
- [99] A. Sahu, I.A. Palani, V. Singh, Investigation on fabrication of NiTi based strain gauge using laser decal transfer based μ -3D printing, *Manuf. Lett.* 32 (2022) 49–53. <https://doi.org/10.1016/j.mfglet.2022.03.001>.
- [100] C.L. Sones, K.S. Kaur, P. Ganguly, D.P. Banks, Y.J. Ying, R.W. Eason, S. Mailis, Laser-induced-forward-transfer: A rapid prototyping tool for fabrication of photonic devices, *Appl. Phys. A Mater. Sci. Process.* 101 (2010) 333–338. <https://doi.org/10.1007/s00339-010-5827-5>.
- [101] J.R.H. Shaw-Stewart, T.K. Lippert, M. Nagel, F.A. Nüesch, A.

- Wokaun, Sequential printing by laser-induced forward transfer to fabricate a polymer light-emitting diode pixel, *ACS Appl. Mater. Interfaces*. 4 (2012) 3535–3541.
<https://doi.org/10.1021/am300598h>.
- [102] V.S. Jitesh Agrawal, Tejendra Dixit, I.A. Palani, M.S. Ramachandra Rao, Fabrication of high responsivity deep UV photodetector based on Na doped ZnO nanocolumns, *Mater. Res. Express*. (2019) 0–12.
- [103] J. Agrawal, T. Dixit, I.A. Palani, V. Singh, Electron Depleted ZnO Nanowalls-Based Broadband Photodetector, *IEEE Photonics Technol. Lett.* 31 (2019) 1639–1642.
<https://doi.org/10.1109/LPT.2019.2940881>.
- [104] J.S. Kim, W. Il Park, C.H. Lee, G.C. Yi, ZnO nanorod biosensor for highly sensitive detection of specific protein binding, *J. Korean Phys. Soc.* 49 (2006) 1635–1639.
- [105] P.H. Yeh, Z. Li, Z.L. Wang, Schottky-gated probe-free ZnO nanowire biosensor, *Adv. Mater.* 21 (2009) 4975–4978.
<https://doi.org/10.1002/adma.200902172>.
- [106] A.M. Mohammed, I.J. Ibraheem, A.S. Obaid, M. Bououdina, Nanostructured ZnO-based biosensor: DNA immobilization and hybridization, *Sens. Bio-Sensing Res.* 15 (2017) 46–52.
<https://doi.org/10.1016/j.sbsr.2017.07.003>.
- [107] K. Nomura, H. Ohta, K. Ueda, T. Kamiya, M. Hirano, H. Hosono, Thin-film transistor fabricated in single-crystalline transparent oxide semiconductor, *Science* (80-.). 300 (2003) 1269–1272. <https://doi.org/10.1126/science.1083212>.
- [108] K. Ellmer, A. Klein, ZnO and its applications, *Springer Ser. Mater. Sci.* 104 (2008) 1–33. https://doi.org/10.1007/978-3-540-73612-7_1.
- [109] F. Claeysens, A. Klini, A. Mourka, C. Fotakis, Laser patterning

- of Zn for ZnO nanostructure growth : Comparison between laser induced forward transfer in air and in vacuum, *Thin Solid Films*. 515 (2007) 8529–8533.
<https://doi.org/10.1016/j.tsf.2007.03.135>.
- [110] M.H. Jung, H. Lee, Open selective patterning of zno nanorods on silicon substrates using nanoimprint lithography, *Nanoscale Res. Lett.* 6 (2011) 1–11. <https://doi.org/10.1186/1556-276X-6-159>.
- [111] A. Christensen, D. Nicol, I. Ferguson, S. Graham, Thermal design considerations in the packaging of GaN based light emitting diodes, *Fifth Int. Conf. Solid State Light*. 5941 (2005) 594118. <https://doi.org/10.1117/12.625956>.
- [112] C. Stelling, C.R. Singh, M. Karg, T.A.F. König, M. Thelakkat, M. Retsch, Plasmonic nanomeshes: Their ambivalent role as transparent electrodes in organic solar cells, *Sci. Rep.* 7 (2017) 1–13. <https://doi.org/10.1038/srep42530>.
- [113] J. Li, N.A. Shepelin, P.C. Sherrell, A. V. Ellis, Poly(dimethylsiloxane) for Triboelectricity: From Mechanisms to Practical Strategies, *Chem. Mater.* 33 (2021) 4304–4327. <https://doi.org/10.1021/acs.chemmater.1c01275>.
- [114] W.G. Kim, D.W. Kim, I.W. Tcho, J.K. Kim, M.S. Kim, Y.K. Choi, Triboelectric Nanogenerator: Structure, Mechanism, and Applications, *ACS Nano*. 15 (2021) 258–287. <https://doi.org/10.1021/acsnano.0c09803>.
- [115] G. Khandelwal, N.P. Maria Joseph Raj, S.J. Kim, Materials Beyond Conventional Triboelectric Series for Fabrication and Applications of Triboelectric Nanogenerators, *Adv. Energy Mater.* 11 (2021) 1–32. <https://doi.org/10.1002/aenm.202101170>.
- [116] G. Zhu, B. Peng, J. Chen, Q. Jing, Z. Lin Wang, Triboelectric

nanogenerators as a new energy technology: From fundamentals, devices, to applications, *Nano Energy*. 14 (2014) 126–138. <https://doi.org/10.1016/j.nanoen.2014.11.050>.

[117] R. Zhang, M. Hummelgård, J. Örtengren, M. Olsen, H. Andersson, H. Olin, Interaction of the human body with triboelectric nanogenerators, *Nano Energy*. 57 (2019) 279–292. <https://doi.org/10.1016/j.nanoen.2018.12.059>.

[118] V. Gerbreders, M. Krasovska, E. Sledevskis, A. Gerbreders, I. Mihailova, E. Tamanis, A. Ogurcovs, Hydrothermal synthesis of ZnO nanostructures with controllable morphology change, *CrystEngComm*. 22 (2020) 1346–1358. <https://doi.org/10.1039/c9ce01556f>.